

0712 1112 1112
REPORT NO. NADC-87159-60

AD-A213 166



THE MECHANICAL AND MICROSTRUCTURAL RESPONSE OF ELEVATED TEMPERATURE PM ALUMINUM-TITANIUM ALLOYS

William E. Frazier, Ph.D.
Air Vehicle and Crew Systems Technology Department (Code 6063)
NAVAL AIR DEVELOPMENT CENTER
Warminster, PA 18974-5000

OCTOBER 1987

FINAL REPORT
Task No. 1
Project No. RS34A57
Work Unit No. ZP180
Program Element No. 62234N



Approved for Public Release; Distribution is Unlimited

Prepared for
Air Vehicle and Crew Systems Technology Department (Code 60C2)
NAVAL AIR DEVELOPMENT CENTER
Warminster, PA 18974-5000

89 10 3 084

NOTICES

REPORT NUMBERING SYSTEM - The numbering of technical project reports issued by the Naval Air Development Center is arranged for specific identification purposes. Each number consists of the Center acronym, the calendar year in which the number was assigned, the sequence number of the report within the specific calendar year, and the official 2-digit correspondence code of the Command Office or the Functional Department responsible for the report. For example: Report No. NADC-86015-70 indicates the fifteenth Center report for the year 1986 and prepared by the Systems and Software Technology Department. The numerical codes are as follows:

CODE	OFFICE OR DEPARTMENT
00	Commander, Naval Air Development Center
01	Technical Director, Naval Air Development Center
02	Comptroller
05	Computer Department
07	Planning Assessment Resources Department
10	Anti-Submarine Warfare Systems Department
20	Tactical Air Systems Department
30	Battle Force Systems Department
40	Communication & Navigation Technology Department
50	Mission Avionics Technology Department
60	Air Vehicle & Crew Systems Technology Department
70	Systems & Software Technology Department
80	Engineering Support Group

PRODUCT ENDORSEMENT - The discussion or instructions concerning commercial products herein do not constitute an endorsement by the Government nor do they convey or imply the license or right to use such products.

APPROVED BY:

W F Moroney

DATE:

8/30/85

W. F. MORONEY
CAPT, MSC, U.S. NAVY

UNCLASSIFIED

SECURITY CLASSIFICATION OF THIS PAGE

REPORT DOCUMENTATION PAGE				Form Approved OMB No 0704-0188	
1a REPORT SECURITY CLASSIFICATION UNCLASSIFIED			1b RESTRICTIVE MARKINGS		
2a SECURITY CLASSIFICATION AUTHORITY			3 DISTRIBUTION AVAILABILITY OF REPORT Approved for Public Release: Distribution is Unlimited.		
2b DECLASSIFICATION/DOWNGRADING SCHEDULE					
4 PERFORMING ORGANIZATION REPORT NUMBER(S) NADC-87159-60			5 MONITORING ORGANIZATION REPORT NUMBER(S)		
6a NAME OF PERFORMING ORGANIZATION Air Vehicle and Crew Systems Technology Department		6b OFFICE SYMBOL (If applicable) 6063	7a NAME OF MONITORING ORGANIZATION		
6c ADDRESS (City, State, and ZIP Code) NAVAL AIR DEVELOPMENT CENTER Warminster, PA 18974-5000			7b ADDRESS (City, State, and ZIP Code)		
8a NAME OF FUNDING/SPONSORING ORGANIZATION NAVAL AIR SYSTEMS COMMAND		8b OFFICE SYMBOL (If applicable)	9 PROCUREMENT INSTRUMENT IDENTIFICATION NUMBER		
8c ADDRESS (City, State, and ZIP Code) Washington, D.C. 20361-0001 Department of the Navy			10 SOURCE OF FUNDING NUMBERS		
			PROGRAM ELEMENT NO 62234N	PROJECT NO R534A57	TASK NO 1
					WORK UNIT ACCESSION NO ZP180
11 TITLE (Include Security Classification) The Mechanical and Microstructural Response of Elevated Temperature PM Aluminum-Titanium Alloys					
12 PERSONAL AUTHOR(S) William Frazier, Ph.D					
13a TYPE OF REPORT Final		13b TIME COVERED FROM _____ TO _____	14 DATE OF REPORT (Year, Month, Day) 1 Oct., 1987		15 PAGE COUNT 177
16 SUPPLEMENTARY NOTATION <i>fr. back</i>					
17 COSAT CODES			18 SUBJECT TERMS (Continue on reverse if necessary and identify by block number)		
FIELD	GROUP	SUB-GROUP	Aluminum Powder Metallurgy, Aluminum Carbide, High Temperature Aluminum Dispersion Strengthened Aluminum Oxide, <i>(S-20)</i> Al ₃ Ti Creep		
11	06				
11	06.11				
19 ABSTRACT (Continue on reverse if necessary and identify by block number)					
<p>In order to extend the useful temperature range of aluminum alloys to 200-300°C, a novel processing scheme was formulated where prealloyed gas atomized powders were mechanically alloyed in the presence of a carbon bearing process control agent to produce an alloy with a fine dispersion of aluminides, carbides, and oxides. Titanium was selected as the prime alloying element since it forms a thermally stable Al₃Ti dispersoid and has the potential to form a stable carbide, i.e., TiC. Also, the low diffusivity and solid state solubility of titanium in aluminum indicated that Al₃Ti should resist coarsening and curtail property degradation. The objective of the study was to investigate the microstructural and mechanical behavior and develop a model to account for the ambient and elevated temperature deformation behavior.</p> <p>Helium gas atomized (AT), mechanically alloyed (MA), and atomized plus mechanically alloyed (AM) aluminum 4 and 6 wt.%Ti alloy powders were vacuum hot pressed and extruded into 22mm diameter round rod. The alloy microstructure was fully characterized using optical and electron microscopy, x-ray</p>					
20 DISTRIBUTION AVAILABILITY OF ABSTRACT <input checked="" type="checkbox"/> UNCLASSIFIED/UNLIMITED <input type="checkbox"/> SAME AS RPT <input type="checkbox"/> DTIC USERS			21 ABSTRACT SECURITY CLASSIFICATION UNCLASSIFIED		
22a NAME OF RESPONSIBLE INDIVIDUAL William Frazier			22b TELEPHONE (Include Area Code) 215 4411301		22c OFFICE SYMBOL 6063

DD Form 1473, JUN 86

Previous editions are obsolete

S/N 0102-LF-014-6603

SECURITY CLASSIFICATION OF THIS PAGE

UNCLASSIFIED

UNCLASSIFIED

SECURITY CLASSIFICATION OF THIS PAGE

19. Abstract (continued)

and electron diffraction; and image analysis. Ambient and elevated temperature mechanical tests were performed in order to assess alloy strength, ductility, notch toughness, and creep resistance.

The microstructures of the AT and AM materials consist of a homogeneous distribution of plate-like Al_3Ti particles 1 to $15\mu\text{m}$ in diameter. In contrast, the Al_3Ti particulates in the MA alloy were inhomogeneously distributed and 3 to $15\mu\text{m}$ in size. Transmission electron microscopy (TEM) revealed $0.01\mu\text{m}$ diameter Al_4C_3 and Al_2O_3 dispersoids preferentially distributed to the grain boundaries of the AM and MA alloys. In addition, $0.1\mu\text{m}$ size spherical and grain-like Al_3Ti particles were observed via TEM in the AT, AM and MA alloy.

A complex synergistic relationship was found between the presence of dispersoids, texture development, and mechanical behavior. Carbides and oxides enhance strength, but decrease (III) fiber texture. The drop in texture effects an increase in creep rate and a decrease in elastic modulus despite the strong correlation between the presence of Al_4C_3 and increased creep rate.



Accession For	
NTIS GRA&I	<input checked="checked" type="checkbox"/>
DTIC TAB	<input type="checkbox"/>
Unannounced	<input type="checkbox"/>
Justification	
By	
Distribution/	
Availability Codes	
Dist	Avail and/or Special
A-1	

CONTENTS

	Page
FIGURES.....	vi
TABLES.....	xi
I. INTRODUCTION.....	1
1. RAPID SOLIDIFICATION TECHNOLOGY (RST).....	1
2. MECHANICALLY ALLOYING.....	4
3. STRENGTHENING MECHANISMS.....	8
(a) Solid Solution Strengthening.....	8
(b) Crystallographic Texture, Grain Size and Cold Work.....	9
(c) Particle Strengthening.....	11
(1) Shearable Particle Strengthening.....	11
(a) Coherency Hardening.....	11
(b) Surface or Chemical Hardening.....	12
(c) Order Hardening.....	12
(d) Stacking Fault Hardening.....	13
(e) Modulus Hardening.....	13
(2) Orowan Looping-Impenetrable Particle Strengthening.....	14
(d) Elevated Temperature Strength.....	16
(e) Creep.....	18
4. COARSENING BEHAVIOR OF DISPERSOID PARTICLES.....	20
5. ALUMINUM-TITANIUM SYSTEM.....	22
(a) Phase Equilibrium.....	22
(1) Microstructure.....	23
(2) Crystallography.....	23
(b) Non-equilibrium Solidification.....	24
(c) Thermal Stability.....	25
(d) Mechanical Properties of PM Aluminum-Titanium Alloys.....	26
II. EXPERIMENTAL PROCEDURE.....	28
1. MATERIAL PROCESSING.....	28
a. Powder Production.....	28
b. Consolidation.....	29
2. MICROSTRUCTURAL CHARACTERIZATION.....	29
a. Chemical Analysis.....	29
b. Brunauer, Emmet, and Teller (BET) Analysis.....	29
c. Thermal Analysis.....	30
d. X-ray Diffraction.....	30
e. Optical Microscopy.....	30
f. Scanning Electron Microscopy (SEM).....	31
g. Transmission Electron Microscopy (TEM).....	31
h. Image Analysis.....	31

3. MECHANICAL PROPERTIES	32
a. Hardness Measurements	32
b. Ambient Temperature Tensile Tests	32
c. Elevated Temperature Tensile Tests	32
d. Creep	33
III. RESULTS AND OBSERVATIONS	34
1. ALLOY POWDER MICROSTRUCTURAL CHARACTERIZATION	34
a. Composition	34
b. Phase Identification	34
c. Powder Morphology	34
d. Optical Microscopy	35
e. Thermal Analysis	36
2. ISOCHRONAL ANNEALING OF THE ALLOY POWDERS	37
a. Microhardness	37
b. X-ray Diffraction	37
c. Optical Metallography	37
3. MICROSTRUCTURAL ANALYSIS OF THE CONSOLIDATED ALLOY	38
a. Compositional Analysis	38
b. Phase Identification	38
c. Optical Microscopy	39
d. Transmission Electron Microscopy (TEM)	39
e. Alloy Texture	40
4. AMBIENT TEMPERATURE MECHANICAL PROPERTIES	40
a. Tensile Properties	40
b. Tensile Properties of the Annealed Rod	41
5. ELEVATED TEMPERATURE TENSILE PROPERTIES	42
a. Tensile Properties	42
b. Dynamic Mechanical Analysis (DMA)	42
6. CREEP PROPERTIES	43
7. FRACTURE BEHAVIOR	44
a. SEM Fractography of Alloy AT4	44
b. SEM Fractography of Alloy AM4	44
c. SEM Fractography of Alloy MA4	45
d. Optical Metallography of Fractured Tensile Specimens	45
IV. DISCUSSION OF RESULTS	46
1. ALLOY POWDER	46
a. Morphology, Microstructure, and Phase Relationships	46
b. Effect of Thermal Exposure	49
2. MICROSTRUCTURE OF THE EXTRUDED ROD	50
a. Composition	50
b. Optical Metallography	51
c. Phase Identification	51
d. Grain Size and Particle Distribution	52
e. Microstructural Model	53
3. DISCUSSION OF MECHANICAL PROPERTIES	53
a. Tensile Strength	53
b. Ductility	55

c. Notch Tensile Strength	56
d. Elastic Modulus	56
4. TENSILE PROPERTIES OF THE ANNEALED ROD	58
a. Strength	58
b. Ductility	58
5. ELEVATED TEMPERATURE TENSILE PROPERTIES	60
6. CREEP	61
a. Logarithmic Creep	61
b. High Temperature Creep	62
c. Nabarro-Herring-Coble Creep	62
d. Creep Behavior of the PM Aluminum-Titanium Alloys	63
V. SUMMARY	64
1. AMBIENT TEMPERATURE PROPERTIES	64
a. Hall-Petch and Orowan Strengthening	64
b. The Role of Oxides, Carbides, and Aluminides	65
2. ELEVATED TEMPERATURE MECHANICAL RESPONSE	67
3. COMPARISON WITH CURRENT ALLOYS	68
a. Ambient Temperature Properties	68
b. High Temperature Strength	69
c. Creep-Stress Rupture	69
4. FUTURE OF PM ALUMINUM TITANIUM	71
VI. CONCLUSIONS	71
VII. RECOMMENDATIONS FOR FUTURE WORK	74
VIII. TABLES	75
IX. FIGURES	85
X. REFERENCES	156

FIGURES

Figure		Page
1.1	Schematic Diagram of the Mechanical Alloying Process.....	85
1.2	Coherency Strengthening: Shear Strength Versus Particle Radius	86
1.3	Chemical Strengthening: Shear Strength Versus Particle Radius	86
1.4	Modulus Strengthening: Shear Strength Versus Particle Radius	87
1.5	Orowan Particle Strengthening: The Effect of Particle Size	88
1.6	Orowan Particle Strengthening: The Effect of Particle Volume Fraction	89
1.7	Diffusion Controlled Coarsening of Al_3Ti Particulates.	90
1.8	Aluminum-Titanium Phase Diagram and the Al_3Ti Crystal Structure	91
1.9	Aluminum Rich Portion of the Aluminum-Titanium Phase Diagram	92
1.10	Titanium in Solid Solution Versus Cooling Rate	92
2.1	Materials Processing Scheme	93
2.2	Mechanical Property Test Specimens a) Tensile, b) Notch Tensile, and c) Creep	94
3.1	X-ray Diffraction Profiles of the AT4, AM4, and MA4 Alloy Powders	95
3.2	X-ray Diffraction Profiles of the As-received and Annealed Master Alloy Powder	96
3.3	Morphology of the Helium Gas Atomized Powders: AT4 and AT6	97
3.4	Morphology of the Atomized and Mechanically Alloyed Powders: a) AM4 and b) AM6	98

NADC-87159-60

Figure	FIGURES (Continued)	Page
3.5	Morphology of the Mechanically Alloyed Powders: a) MA4 and b) MA6.....	99
3.6	Morphology of a) Alcan Aluminum and b) the Master Alloy used to Produce MA4 and MA6 ..	100
3.7	Optical Micrographs of Helium Gas Atomized Powders: a) AT4 and b) AT6.....	101
3.8	Optical Micrographs of Atomized and Mechanically Alloyed Powders a) AM4 and b) AM6.....	102
3.9	Optical Micrographs of the Aluminum-Titanium Master Alloy: a) As-received and b) Annealed for 24 hrs. at 1000°C in a Vacuum.....	103
3.10	Optical Micrographs of Mechanically Alloyed Powders, a) MA4 and b) MA6.....	104
3.11	Differential Thermal Analysis Profiles of the AT4 Alloy Powder	105
3.12	Differential Thermal Analysis Profile of the AM4 Alloy Powder.....	106
3.13	Differential Thermal Analysis Profile of the MA4 Alloy Powder.....	107
3.14	Differential Thermal Analysis Profile of the Al ₃ Ti Master Alloy	108
3.15	Microhardness of Alloy Powders Annealed for 24 hrs: a) 4 wt.%Ti and b) 6wt.%Ti.....	109
3.16	Relative X-ray Diffraction Peak Intensity of Al ₃ Ti for Isochronally Annealed AT4 Powder	110
3.17	Relative X-ray Diffraction Peak Intensity of Al ₃ Ti for Isochronally Annealed AM4 Powder.....	111
3.18	Relative X-ray Diffraction Peak Intensity of Al ₃ Ti for Isochronally Annealed MA4 Powder.....	112
3.19	Optical Micrographs of the Extruded Alloy Rod: As-received a) AT4 and b) AT6	113
3.20	Optical Micrographs of the Extruded Alloy Rod: As-received a) AM4 and b) AM6.....	114
3.21	Optical Micrographs of the Extruded Alloy Rod: As-received a) MA4 and b) MA6.....	115

Figure	FIGURES (Continued)	Page
3.22	Transmission Electron Micrographs of Extruded a) AT4, b) AM4, and c) MA4.....	116
3.23	Transmission Electron Micrographs of Extruded a) AT6, b) AM6, and c) MA6.....	117
3.24	Transmission Electron Micrographs of Extruded and Annealed (300°C, 100hrs.) a) AT4, b) AM4, and c) MA4	118
3.25	Transmission Electron Micrographs of Extruded and Annealed (300°C, 100hrs.) a) AT6, b) AM6, and c) MA6	119
3.26	Bright Field/Dark Field Transmission Electron Micrograph Pair of Extruded AM4.....	120
3.27	Particle Size Distribution of the Al ₃ Ti Aluminide of the a) As-received and b) Annealed (300°C for 100hrs.) Alloys	121
3.28	Grain Size Variation of the As-received and Annealed (300°C for 100hrs) alloys Yield strength of Isochronally Annealed (100 hrs) Alloys.....	122
3.29	(111) and (200) Pole Figures for As-received Alloys containing 4 wt.% Titanium	123
3.30	(111) and (200) Pole Figures for As-Received Alloys Containing 6 wt.% Titanium	124
3.31	Yield Strength of Isochronally Annealed (100 hrs.) Alloys	125
3.32	Tensile Strength of Isochronally Annealed (100 hrs.) Alloys	126
3.33	Tensile Elongation of Isochronally Annealed (100 hrs.) Alloys	127
3.34	Reduction in Area of Isochronally Annealed (100 hrs.) Alloys	128
3.35	Yield Strength of the Aluminum-Titanium Alloys Tested at Temperature	129
3.36	Tensile Strength of the Aluminum-Titanium Alloys Tested at Temperature	130
3.37	Tensile Elongation of the Aluminum-Titanium Alloys Tested at Temperature	131

NADC-87159-60

Figure	FIGURES (Continued)	Page
3.38	Reduction in Area of the Aluminum-Titanium Alloys Tested at Temperature	132
3.39	Shear Modulus of the Aluminum-Titanium Alloys Measured as a Function of Temperature Using Dynamic Mechanical Analysis	133
3.40	Creep Response of Alloys AM4 and MA6 at 138 MPa	134
3.41	Creep Response of Alloys MA4 and MA6 at 138 MPa	135
3.42	Creep Response of Alloy AM6 at 138 and 172 MPa	136
3.43	Creep Rate Versus Volume Percent Al_4C_3	137
3.44	Scanning Electron Microscopy Tensile Fractographs of AT4: a) As-received and b) tested at 300°C	138
3.45	Scanning Electron Microscopy Tensile Fractographs of AM4: a) As-received and b) tested at 300°C	139
3.46	Scanning Electron Microscopy Tensile Fractographs of MA4: a) As-received and b) tested at 300°C	140
3.47	Optical Micrographs of Tensile Specimens Tested at 25°C. a) AT6, b) AM6, and c) MA6	141
3.48	Optical Micrographs of Tensile Specimens Tested at 300°C. a) AT6, b) AM6, and c) MA6	142
3.49	Optical Micrographs of Creep Specimens Tested at 250°C. and 138 MPa for 150 hrs. a) AM4, b) AM6, and c) MA6	143
4.1	Microstructural Model Illustrating the Relative Size and Spacing of Particles and Grains	144
4.2	Calculated Orowan Strengthening of Dispersoids Versus Alloy Strength	145
4.3	Effect of Aluminum Carbides on Tensile Strength	146
4.4	The Effect of Grain Size on Yield Strength	147

NADC-87159-60

Figure	FIGURES (Continued)	Page
4.5	Effect of Texture on Young's Modulus	148
4.6	Effect of Al_3Ti on Young's Modulus	149
4.7	Effect of Dispersoids on Texture Development	150
4.8	Effect of Texture on Creep Rate	151
5.1	The Effect of Grain Size on the Strength of PM Aluminum-Titanium and Pure Aluminum	152
5.2	Hall-Petch Strengthening of PM Aluminum-Titanium and Pure Aluminum	153
5.3	The Strength of Several Aluminum Alloys Tested at Temperature	154

TABLES

Table	Page
1 The Effect of Oxides on the Mechanical Properties of Aluminum	5
2 The Influence of Carbides and Oxides on Grain Size (32)	7
3 Diffusivities and Solubilities of Several Elements in Aluminum	24
4 The Lattice Parameters of Al_3Ti and Al_3Zr	25
5 Mechanical Properties of Mechanically Alloyed Al-4wt.%Ti (18)	27
6 Effect of Thermal Exposure on the Mechanical Properties of Mechanically Alloyed Al-4 wt.%Ti (18)	27
7 Composition of the Alloy Powders	75
8 Phase Identification of As-Received Powder Alloys	76
9 BET Analysis Results	77
10 Composition of the Powder Alloys	77
11 Phase Identification of the Alloy Rod	78
12 Calculated Volume Percent of Second Phases Based on Compositional Stoichiometry	78
13 Particle Size (μm) as measured by TEM of the Alloy Rod Annealed for 100hrs.	79
14 Grain Size (μm) of the Alloy Rod Annealed for 100hrs.	79
15 Texture of the Extruded Alloy Rod: Random Intensity Times Peak Intensity for the (111) and (200) Planes	80
16 Ambient Temperature Tensile Properties	80
17 Tensile Properties of the Annealed Rod	81
18 Elevated Temperature Tensile Properties	82

TABLES (Continued)

Table		Page
19	Shear Modulus/Normalized Shear Modulus Versus Temperature	83
20	Creep Rate of the PM Aluminum-Titanium Alloys Measured Between 50 and 150 hours	83
21	Orowan Strength: Calculated from the Al_3Ti Particle Size	84
22	Orowan Strength: Calculations Based on the Presence of Al_4C_3	84
23	Ambient Temperature Mechanical Property Comparison	66
24	The Predicted Creep Rate for Fine Grained Pure Aluminum (38, 73)	67
25	Ambient Temperature Properties of Several Elevated Temperature Alloys (12, 18, 97, 98, 99)	68
26	The Creep Behavior of Several Aluminum Alloys at 138 MPa and 220°C (12, 18, 97)	70

I. INTRODUCTION

Advanced powder metal (P/M) aluminum alloys are currently being developed using mechanical alloying and rapid solidification techniques. The objective is to obtain a homogeneous microstructure consisting of finely dispersed thermally stable compounds. The first commercial applications of these materials appear to be in advanced aircraft where substitution of aluminum for titanium could show a 15% weight savings. (1) Utilization of these materials as wing skins of aircraft operating in a Mach 3.0 environment requires retention of structural strength at temperatures between 150-175°C. Application of these advanced alloy systems appears to be impellers for small gas turbines. Millan (2) identifies several military and commercial engine systems for the potential application of P/M alloys, e.g., AGT101 automotive engine.

1. RAPID SOLIDIFICATION TECHNOLOGY (RST).

Unique structures, morphologies, and metastable phases are associated with RST-produced alloys. The distinct microstructures observed are related to the alloy's response to rapid cooling from the melt. Freezing is necessarily associated with the heat of fusion; recalescence retards the rate at which the solid-liquid interface moves across the particle and tends to coarsen the previously solidified structure. (3,4) RST powders exhibit three distinct morphologies: microcrystalline, cellular, and dendritic. (5,6) The microcrystalline region is the most rapidly solidified structure which consists of an ordered arrangement of atoms and a uniform chemical composition. It is homogeneous, resists chemical attack, and is the slowest to coarsen. The cellular and dendritic microstructures correspond to slower cooling rates. Grant (7) has correlated cooling rate with secondary dendritic arm spacing (DAS) and powder size. Atomization results in cooling rates between 10^3 - 10^5 K/s, DAS of 0.8-8.0 μ m, and particle sizes of 20-250 μ m in diameter. Compositional gradients exist across the cellular and dendritic structures. Intermetallic compounds nucleate and grow at boundary interfaces; consequently, DAS is important in determining particle size and distribution.

Mehrabian and Levi (3,8) have studied heat flow during rapid solidification. The solidification of gas atomized powders was found to be adequately described by the use of an enthalpy model. The thermal history of the powder is a path excursion on an enthalpy temperature diagram which reflects the competition between recalescence and external heat loss. The relevant equations are:

Eq. [1]

$$H - H_{sm} = [H_m + K_L (T - T_m)] (1 - g) + K_s (T - T_m) g$$

$$\Gamma = (H - H_{sm})/H_m$$

$$\Phi = k_L (T - T_m)/H_m$$

Γ	=	the ordinate value; dimensionless enthalpy
Φ	=	dimensionless temperature
H	=	enthalpy of the system at T
H_{sm}	=	enthalpy of the solid at the melting temperature
g	=	fraction of solid
k	=	heat capacity
H_m	=	enthalpy of fusion

During atomization, rapid heat loss to the surroundings causes a liquid metal droplet to undercool. A quantity of solid phase nucleates and grows rapidly into the undercooled melt. The average temperature of the droplet continues to decline for a short period until the rate of heat production exceeds the rate of removal. Mehrabian and Levi (3) concluded that for process parameters typically found in gas atomization, external cooling has little effect on extending the range of rapid solidification, i.e. solidification proceeds adiabatically. Newtonian heat transfer conditions exist and there is a minimal temperature gradient within the solidifying powder particle. Therefore, only when the metal has been hypercooled and heat equivalent to the heat of fusion has been removed prior to nucleation, can solidification occur without further heat extraction. (8,9).

RST has been successful in producing alloys with mechanical properties which are substantially more resistant to thermal exposure than current wrought aluminums such as 2219 (Al-6.3Cu-0.3Fe-0.2Si). In large part, the success stems from alloy additions of elements with low diffusion rates and low solid state solubility. The low solid state solubility of the element in the matrix results in a high volume fraction of intermetallic compounds; the low diffusivity of the alloy addition decreases the rate of particle coarsening at service temperatures.

The current generation of elevated temperature RST aluminum alloys is based on transition elements, e.g., Al-Fe-X. Screening studies conducted by Sanders and Hildeman (10), Adams et. al (11) and Griffith et. al (12) have shown this composition to be an excellent compromise between ease of production and superior mechanical properties. The various materials producers have decided to pursue different ternary and quaternary compositions, e.g., Alcoa: Al-Fe-Ce, Alcan: Al-Cr-Zr, Allied: Al-Fe-V-Si, and Pratt and Whitney: Al-Fe-Mo.

There appear to be many compelling reasons why Fe is the alloying element of choice. Iron has a rather high liquid state solubility in aluminum and this enables the use of conventional atomization and melt spinning processes. The microstructure observed in atomized Al-Fe powders consists of the A and B type morphologies described by Jones. (4) and interdispersed throughout the alloy are fine thermally stable incoherent particles of Al_3Fe and Al_6Fe . (5) Also, iron has a low diffusivity and low solid state solubility in aluminum; consequently, particle coarsening is inhibited.

Ternary and quaternary alloying additions may serve several purposes: 1. alteration of the crystal structure of the Al-Fe precipitates, 2. formation of new dispersoids of independent structure and composition, and 3. modification of the solidification behavior of the alloy. For example, Ce additions have been shown to increase the tendency for partitionless solidification and to inhibit the formation of the equilibrium Al_3Fe phase in favor of an ordered ternary Al-Fe-Ce phase (possibly tetragonal $CeFe_4Al_6$) (13) with superior thermal stability. (14, 15) Skinner et. al (16) have shown that the addition of V and Si to the Al-Fe system causes the formation of cubic $Al_{12}(Fe,V)_3Si$ which is extremely resistant to coarsening

This is attributed to the low interfacial energy of the dispersoid formed in alloys with an Fe:V ratio between 10:1 and 5:1.

2. MECHANICALLY ALLOYING.

Mechanically Alloying (MA) has been used to produce aluminum alloys with excellent mechanical properties at service temperatures of 250-300°C. (17, 18) These materials derive their elevated temperature properties from the fine dispersion of aluminides, carbides, and oxides distributed in their microstructures.

Mechanical alloying is an excellent means of producing a reasonably homogeneous powder from mixed elemental powders. Elemental powders are ball milled in a sealed attritor in the presence of a carbon bearing compound such as alcohol or stearic acid, Figure 1.1. The steel balls impelled by rotating paddles repeatedly impact the powders, causing them to cold weld. Cold welding is controlled by the amount and type of the carbon bearing agent used in the process. The oxide layer inherently present on the powder's surface is fractured upon impact. Oxides are dispersed into the material along with the carbon bearing compound. New oxides regenerate on the fresh surface and the process is repeated. (19) The result is a heavily cold worked powder of a homogeneous composition and uniform dispersion of submicron oxides and carbides.

The origin of today's dispersion strengthened powder metallurgy can be traced back to 1948 when sintered aluminum powder (SAP) alloys were introduced by Aluminum Industrie Aktiengesellschaft (AIAG). (20, 21) The development and processing of SAP alloys has been extensively reviewed by Block. (22) Basically, a composite powder consisting of an aluminum matrix and Al_2O_3 particles is produced by ball milling commercially pure aluminum powder. During milling, the tenacious aluminum oxide surface layer is broken up and embedded in the aluminum matrix by a process of repeated fracture and cold welding. The result is a flake-like aluminum powder which is typically consolidated into billets by vacuum hot pressing. The billets are subsequently hot worked to achieve full density and optimal properties.

Early research by Lenel et. al (23) and Lyle (20) demonstrated that SAP alloys could be produced having excellent room temperature tensile strengths (400MPa) and retain significant strength to temperatures as high as 400°C (175MPa). A direct correlation was found to exist between the vol. % oxide and mechanical properties.

TABLE 1. The Effect of Oxides on Mechanical Properties of Aluminum

Vol. % Oxide	UTS (MPa)	YS (MPa)	% Elongation
0	130	100	30
10	270	190	11
20	400	270	2

An increase in oxide content increases the material's strength but sharply decreases its ductility. Further increases in strength and ductility were made by improving the ball milling process and removing adsorbed hydrogen by powder degassing. However, despite these improvements, SAP alloys were never used extensively because of their high production cost and low ductility. (24)

Benjamin (25) successfully produced an oxide dispersion strengthened nickel based alloy (IN-853) in 1970 by using a process called mechanical alloying (MA). The process used to produce mechanical alloyed materials differs from SAP in that a high energy mill is used. High energy mills include vibratory mills, attritors, and large diameter tumbler mills. (26) The effect of the high energy milling operation is to produce a composite metal powder with ultrafine dispersoids and submicron grain sizes. Furthermore, the composition of SAP alloys consists solely of aluminum and Al_2O_3 . Ma, however, is used to combine a variety of elements producing an homogeneous alloy powder or a particula reinforced composite alloy powder.

To achieve optimum results, the MA process must be carefully monitored. The hardness, microstructure, and size distribution of the powder is scrutinized as a function of milling time, etc...(27)

The powder's hardness increases rapidly during the initial stage of mechanical alloying; however, hardness levels plateau, generally indicating the completion of MA. (26) Powder microstructure is commonly used to establish the thoroughness of MA process. The microstructure of MA powders is lamellar and the closer the lamellar spacings the greater the degree of homogeneity. As a rule of thumb, lamellae should not be visible at 50x using an optical microscope. The average powder size is also an important processing parameter. Initially, powder size increases due to particle cold welding. Continued MA results in a decrease in powder size resulting from the fracture of heavily deformed particles.

Benjamin and Bomford (28) investigated the effect of process control agents on the mechanical properties of MA aluminum in comparison to the SAP alloys. Both stearic acid and methanol were effective antiwelding agents. The primary difference was in the relative amounts of oxygen and carbon introduced into the system. It was found that MA aluminum achieved the same strength as SAP alloys at lower dispersoid levels. A yield strength of 250MPa was obtained with 3 vol.% dispersoids in MA and 12 vol. % in SAP alloys.

Lovshenko and Jangg (29) investigated the effect of carbon content on the mechanical properties of extruded MA aluminum. Aluminum powder, 50 μ m in diameter, was alloyed with acetylene carbon black to produce alloys containing 1, 2, and 3 wt.% carbon. The tensile strength increased from 260 MPa to 430 MPa and the percent elongation decreased from 11 to 4%.

Arnhold and Baungarten (30) examined the effect of Al_2O_3 and Al_4C_3 dispersoids on the behavior of reaction milled aluminum alloys termed DISPAL. The tensile strength and yield strength of an alloy was observed to increase with total dispersoid content; however, the type of dispersoid (Al_2O_3 or Al_4C_3) was not found to effect alloy strength.

Research has been directed in order to identify the conditions under which dispersoids form and their crystal structures. (24, 28, 31) Singer et. al (24) employed selected area diffraction (SAD) to ascertain that the amorphous oxides produced during MA are crystallized to ζ - Al_2O_3 during annealing treatments.

SAD revealed the presence of ζ - Al_2O_3 after annealing for 2 hrs. at 400°C , but not after annealing at 300°C . It was also established unambiguously that carbon bearing process control agents decompose during MA to form Al_4C_3 .

The oxides and carbides are important to the strength of MA materials. Their fine size (0.01 - $0.3\mu\text{m}$) inhibits dislocation motion, prevents recrystallization, and curtails grain growth. However, upon coarsening, they lose their effectiveness; consequently, the thermal stability of the carbides and oxides is important to the mechanical behavior of elevated temperature aluminum alloys. Research by Kang et. al. (32) indicates that carbide growth starts at temperatures as low as 315°C , while oxides are stable to 565°C .

TABLE 2. The Influence of Carbides and Oxides on Grain Size (32)

<u>Annealing Treatment</u>	<u>Grain Size (μm)</u>	<u>Dispersoid Size (μm)</u>	
		<u>(Al_4C_3)</u>	<u>(Al_2O_3)</u>
As Extruded	0.35	0.03	0.01
$315^\circ\text{C}/1.5$ hr.	0.35	0.06	0.01
$425^\circ\text{C}/1.5$ hr.	0.43	0.10	0.01
$565^\circ\text{C}/1.5$ hr.	0.50	0.20	0.01

Eric (18) has conducted screening studies to assess the effect of transition elements on the ambient and elevated temperature mechanical properties of MA aluminum alloys. Alloy strength was correlated to the presence of Al_2O_3 and Al_4C_3 dispersoids. The effectiveness of transition element additions was minimal and independent of the element selected. This response was attributed to the incomplete micro-incorporation of alloying elements during processing.

The creep resistance of the MA alloys was excellent. Additions of transition elements, especially titanium, iron, and chromium produced enhanced creep response. The stress to produce 0.2% strain in

100 hrs. was estimated to be 156MPa at 232°C and 96MPa at 343°C. Creep response was found to be independent of grain size and dependent on dispersoid content.

3. STRENGTHENING MECHANISMS.

The properties of many aluminum alloys have been specifically tailored for particular applications e.g., corrosion and strength. (33) This has been made possible by an empirical and theoretical understanding of the synergistic relationship between the alloy's structure property and processing history. (34) Aluminum alloys can be strengthened by several means: 1. solid solution strengthening, 2. cold work, 3. grain size, 4. crystallographic texture, 5. age hardening, and 6. dispersion strengthening. This partial list of strengthening have a common objective: they impede the motion of dislocations and thereby inhibit deformation and increase strength. The most effective means of strengthening aluminum alloys are based on the introduction of a fine second phase particulates; therefore particular emphasis will be focused on particle strengthening.

a. Solid Solution Strengthening. Haasen (35) and Dieter (36) have reviewed the theories regarding solid solution strengthening. There are at least five important ways a solute can interact with the matrix to enhance strength: 1. relative size factor, 2. relative modulus factor, 3. electrical interaction, 4. chemical interaction, and 5. configurational interactions. Of the above, the effect of modulus and relative atomic size on mechanical properties have received the most attention.

When an atom of a different atomic radius than the matrix is introduced to the system, elastic atomic interaction due to their relative size difference ensue. These elastic interactions impede the motion of dislocations and it has been shown that an alloy's strength is directly proportional to the quantity of solute. (37) Starke and Wert (38) suggest that the appropriate equation combines the contribution of atomic size and modulus.

eq. [2]

$$\Delta\tau = 1/a (da/dc) + 1/G (dG/dc)$$

$\Delta\tau$ = increase in shear strength

a = lattice parameter

G = shear modulus

This equation suggests the need for a high concentration of a solute element having a different modulus and atomic radius than the matrix. Unfortunately, atoms of large size differences generally have low mutual solid solubilities.

The electron cloud of a solute atom tends to resist compression. Consequently, electrons tend to be associated with the tension side of defects, creating an electrical dipole which curtails dislocation mobility. Hibbard (39) demonstrated that the yield strength of copper was linearly related to the electron to atom ratio of the alloy.

Short range atomic interaction exists in most solid solution alloys. These interactions may result in short range atomic order. A dislocation which passes through an ordered arrangement of atoms raises the free energy of the system; consequently, dislocation motion is impeded.

b. Crystallographic Texture, Grain Size, and Cold Work.

The role of texture, grain size, and cold work are considered here in unison because of their close interdependent relationship. Crystallographic texture is developed during alloy processing. Since texture is the preferred orientation of crystallographic planes, its development affects both elastic and plastic response of the material. The elastic modulus of single crystal aluminum varies from 76.1 GPa in the $\langle 111 \rangle$ direction to 63.7 GPa in the $\langle 100 \rangle$ direction. (40) The modulus of polycrystalline aluminum is seen to be dependent on the average orientation of the individual grains. Schmid (41) was the first to recognize that a critical resolved shear stress must be exceeded to produce slip in a single crystal along specific planes and directions. i.e., the ease of deformation was dependent on crystallographic

orientation. Taylor (42) and, later, Bishop and Hill (43) developed a relationship between tensile yield stress and critically resolved shear stress for polycrystalline fcc and bcc materials.

eq. [3]

$$\sigma = Mt$$

σ = yield stress

t = critical resolved shear stress

M = Taylor factor

The average "Taylor Factor" was estimated to be 3.1. The development of texture alters the Taylor factor and hence the alloy's strength. Palmer et al. (44) investigated the effect of texture on the tensile properties of extruded powder metallurgy alloy Al-3Li-2Cu-0.2Zr. The [111] pole intensity within 5 degrees of the tensile axis was measured and correlated to the alloy's yield strength. Yield strength was found to vary from 420 to 520MPa as relative intensity of the [111] pole change from 2 to 22.

Hall (45) and Petch (46) developed a mathematical model (the Hall-Petch equation) relating yield stress to the grain size of steel alloys. The Hall-Petch equation has since been found to be valid for most polycrystalline alloys and aluminum alloys. (47, 48)

eq. [4]

$$\sigma_o = \sigma_i + k \sqrt{D}$$

σ_o = yield stress

σ_i = constant (frictional stress on moving dislocations)

k = constant (related to dislocation pile ups)

D = grain diameter

Wert (49), Kim and Griffith (50) have examined the effect of grain size on the yield stress of 7000 series (Al-Mg-Zn) aluminum alloys. The Hall-Petch slope for peak aged 7075 was estimated at 120 MPa $\mu\text{m}^{1/2}$ and for underaged 7091 with grain size range of 2.4 to 46 μm , the Hall-Petch slope was 220 MPa $\mu\text{m}^{1/2}$.

Decker (47) presents yield strength and grain size data for an aluminum copper alloy and for commercially pure aluminum. The Hall-Petch slopes were calculated to be 125 MPa $\mu\text{m}^{1/2}$ and 75 MPa $\mu\text{m}^{1/2}$ respectively.

Cold deformation is commonly used to enhance the tensile strength of 1000 (Al), 3000 (Al-Mn-Mg), 4000 (Al-Si), and 5000 (Al-Mg) series aluminum alloys. The strength of commercially pure 1000 series aluminum can be increased more than 100%. Cold work increases dislocation density to a point that their interactions impede deformation. The mathematical model relating yield strength to dislocation density is similar to the Hall-Petch relationship. (51, 52)

eq. [5]

$$\sigma_o = \sigma_i + \alpha G / \sqrt{\rho}$$

σ_o	=	yield stress
σ_i	=	constant
α	=	constant (0.3 to 0.6)
G	=	shear modulus
ρ	=	dislocation density

C. Particle Strengthening. The hardening of metallic alloys by the utilization of second phase dispersoids has been reviewed thoroughly by several authors (33, 38, 47, and 53). Particle strengthening may be divided into two broad categories: 1. hardening by shearable particles and 2. hardening by impenetrable dispersoids.

(1) Shearable Particle Strengthening. Shearable Particle strengthening results from the resistance of particles to shear by dislocation motion. Five ways have been cited in which particles resist shearing(53):

(a) Coherency hardening, (b) Surface or chemical hardening, (c) Order hardening, (d) Stacking-fault hardening, and (e) Modulus hardening.

(a) Coherency Hardening Matrix particle coherency involving atomic plane disregistry results in elastic strain fields. These strain fields resist dislocation motion and thus contribute to the alloys' strength.

Decker (47) suggests an equation of this form may be applicable.

eq. [6]

$$\tau = 6Gb^{-1} (rf)^{1/2} \epsilon^{3/2}$$

τ	=	increase in shear strength
G	=	shear modulus
r	=	particle radius
f	=	volume fraction of particles
ϵ	=	coherency strain

The strength is mildly dependent on r and f , but strongly on coherency strain. A plot of shear strength versus particle radius is presented in Figure 1.2 which illustrates the effect of coherency strain.

(b) Surface or Chemical Hardening. The shearing of a particle creates a new surface and or interface. Associated with the creation of an interface is a rise in energy which must be supplied to the system during deformation. The applicable equation is (53)

eq. [7]

$$\tau = 2(3\pi)^{1/2} G(\sigma'Gb)^{3/2} (b'r)^{1/2}$$

σ	=	surface energy
----------	---	----------------

A plot of shear strength versus particle radius generated from equation [7] is presented in Figure 1.3 and illustrates the effect of particle surface energy on alloy strength.

(c) Order Hardening. Order hardening is the result of the creation of an antiphase boundary when a dislocation shears an ordered lattice. This type of strengthening is believed to be operative in nickel alloys containing large volume fractions of ordered γ' (Ni_3Al) and in aluminum alloys strengthened by δ' (Al_3Li). Martin(53) presents several equations developed by Brown and Ham, the most fundamental of which is given below.

eq. [8]

$$\tau = (\sigma'2b) [(3\sigma fr)/(\pi T)]^{1/2}$$

σ = surface energy of antiphase boundary

T = dislocation line tension

This equation illustrates how the strength of an alloy can increase with increasing r even though particle volume fraction remains constant.

(d) Stacking Fault Hardening. Stacking fault hardening is similar in nature to order hardening. Stacking fault hardening occurs when both the matrix and particle have the same crystal structure (i.e., fcc or hcp) and there is a difference in the stacking fault energies of the particulate and matrix phases. The distance between the components of an extended dislocation will increase within a particle of lower stacking fault energy.(54) Hence, the dislocation must be dragged out of the particle with an energy equal to the difference in the matrix-particle stacking fault energy. The increase in strength is given by the following expression:

eq. [9]

$$\tau = (8 \pi)^{1/2} G(\delta\sigma'Gb)^{3/2} (rf b)^{1/2} l_m$$

σ = the difference in stacking fault energy between the particle and matrix

l_m = a complex function of r and the stacking fault energy of the matrix.

(e) Modulus Hardening. Alloy hardening can result from the difference in moduli of the matrix and particle. Since the energy of a dislocation is proportional to the shear modulus of the material in which it resides, an energy change will result when a matrix dislocation interacts with a particle having a different modulus. An equation which describes this increase in strength is presented by Martin(53) and attributed to Knowles and Kelly.

eq. [10]

$$\tau = (3\Delta G/4\pi^2)(\Delta G/Gb)^{1/2} [0.8 - 0.1431n(r/b)]^{3/2} (r)^{1/2}$$

ΔG = the difference between the shear modulus of the matrix and the particle.

This equation illustrates how moduli differences can account for the strengthening effect of a softer phase, e.g., copper in iron ferrite.(47) A plot of shear strength versus particle radius is presented in Figure 1.4. Alloy strength is seen to be strongly related to particle radius with particle radii of less than $0.01\mu\text{m}$ necessary for significant strengthening.

The identification of the single strengthening mechanism is difficult. Not only are the theoretical mathematical relationships similar, but in all likelihood there is more than one mechanism operating. A useful empirical equation is(38)

eq [11]

$$\tau = cf^m r^n$$

- τ = shear stress
- c = material constant
- f = volume fraction of the particulate
- r = average radius of the particles
- m = constant (usually 1/2)
- n = constant (usually 1/2)

(2) Orowan Looping-Impenetrable Particle Strengthening. The strength of an alloy containing a dispersion of incoherent impenetrable particles was first considered by Orowan.(55) The shear stress required for a dislocation to loop a particle was found to depend solely on the properties of the matrix and the spacing of the particles.

eq. [12]

$$\tau = Gb \lambda$$

τ	=	shear stress
G	=	shear modulus
λ	=	average particle spacing

Orowan's original relationship has been modified by a number of authors to account for the dislocation dipole effect, dislocation line tension, and the mean planar spacing of particles of finite diameters.(53) Dislocation dipole results when a dislocation bows around a defect. Dislocation of opposite sign come in close proximity; consequently, the stress required for looping is reduced. A further modification to the Orowan model was necessary to account for the fact that the line tension of edge dislocations is greater than that of a screw dislocation. Also, the center to center spacing between large particles does not adequately describe the length of a dislocation bowing between these particles. This factor was accounted for by substituting the equation for mean planar spacing (i.e., the average distance between particle surfaces) for average particle spacing. This more precise version is derived by Martin(53) and presented below.

eq. [13]

$$\tau = \frac{0.81Gb}{2\pi(1-\nu)^{1/2}} \frac{\ln(2r_s/r_o)}{(h_s - 2r_s)}$$

τ	=	increase in critical resolved shear stress
r_s	=	$r(2/3)^{1/2}$, r = particle radius
h_s	=	average center center spacing of particles
r_o	=	dislocation core radius, approximately b
G	=	shear modulus of matrix

Figures 1.5 and 1.6 were generated using equation [13]; Figure 1.5 is a plot of shear strength versus particle radius and Figure 1.6 plots shear strength versus particle volume fraction. These figures illustrate the requirement for fine particles and high volume particle fractions, e.g., radii $\leq 0.05\mu\text{m}$ and volume fractions ≥ 0.1 .

(d) Elevated Temperature Strength. At ambient temperatures, dislocation motion is primarily confined to slip along crystallographic closed packed planes and directions. However, at homologous temperatures above $0.3T_m$, thermally activated processes such as dislocation climb are possible.(56) Three main theories have been proposed to account for the drop in yield strength at elevated temperatures and are due to: 1. Ham and Brown, 2. Humphreys, Hirsch and Gould. 3. Shewfelt and Brown.(53)

Ham and Brown's model assumes that dislocations in particle hardened alloys remain in their slip planes. In order to bypass dispersoids, the dislocations must climb by a thermally activated process. The theory predicts a linear decrease in shear stress, τ , with temperature, T .

eq. [14]

$$\tau = \frac{1}{2}(Gb'(1-\nu)^{1/2}L) + (SUp)(\sqrt{2}Lb^3) + (SKT)(\sqrt{2}Lb^3) \ln((\epsilon'S^2)/(2Pb^4V_d))$$

G = shear modulus of the matrix
 b = Burger's vector
 ν = Poison's ratio
 L = interparticle spacing
 S = side length of a particle (assumed square)
 Up = activation for dislocation pipe diffusion
 ϵ' = strain rate
 V_d = Debye frequency

Humphreys, Hirsch, and Gould compared the rates of jog nucleation and migration at the site of a spherical dispersoid. They concluded that jog nucleation is the controlling factor and arrived at the expression:

eq. [15]

$$[cG(t-t_b)]^{1/2} = (Up/v) + (2W_{jo}/v)$$

$$- (kT/v) \ln[4AV_d(t-t_b)b^5PD^2/d^2\epsilon'kT]$$

- c = is a constant (c = 1 for edge dislocation and (1 + v)/(1 - v) for screw dislocation)
- τ_b = the back stress due to a dislocation increasing its line length when climbing over a particle
- W_{jo} = the activation energy for jog formation
- A = an entropy factor
- D = particle spacing
- d = the effective particle spacing in the slip plane

The third model proposed by Shewfelt and Brown(57) appears to be the most consistent with empirical observations. It is based on velocity calculations for an edge dislocation passing through a random array of point dispersoids bypassed by local climb. It correctly predicts the limiting value of climb controlled yield stress at elevated temperatures to be 0.4 of the Orowan stress and that the velocity of a dislocation is exponentially dependent on the applied shear stress.(53) The basic mathematical expression arrived at by Shewfelt and Brown is

eq. [16]

$$\tau = Gb[0.51 + 0.121 \log(\epsilon'kTR^2/4\pi pb^2a_vGDD_s) + 0.052E_s/kT]/D$$

- D_s = $D_o \exp(-E_s/kT)$
- p = dislocation density
- R = particle radius
- D = the lattice spacing of particles
- a_v = area associated with a vacancy

(e) Creep. Creep is a time dependent deformation process of significant importance in the design and usage of alloys for elevated temperature applications. The typical strain versus time creep curve of an alloy has three distinct regions: 1. primary creep, 2. steady state creep, and 3. tertiary creep. Steady state creep has the most practical significance because of the short term transient nature of primary and tertiary creep.

The creep process may be broadly classified as dislocation creep and diffusional creep. Dislocation creep can occur at high and low temperatures. At elevated temperatures, dislocation creep is via dislocation climb and at lower temperatures, it occurs by vacancy diffusion along dislocation cores.

The diffusional creep process can also be divided into two categories: 1. Coble creep, and 2. Herring-Nabarro. Coble creep dominates at low temperatures and stresses where mass transport along grain boundaries is favorable. Herring-Nabarro creep is dominant at elevated temperatures ($T \geq 0.6T_m$) and by mass transport by lattice diffusion.

Starke and Wert(38) present a constitutive equation which combines the mathematical relationships for the above elevated temperature deformation processes.

eq. [17]

$$\dot{\epsilon} = (AGb/kT) (\sigma/G)^n [D_1 + 50D_c(\sigma/G)^2] + (100\Omega D_1/kTd_2) (\sigma - 0.72\Gamma/d) (1 + 3.38Dg/dD_1)$$

A	=	dimensionless constant
G	=	shear modulus
b	=	Burger's vector
k	=	Boltzmann's constant
σ	=	stress
D_1	=	lattice diffusivity
D_c	=	core diffusivity

D_g	=	grain boundary diffusivity
Ω	=	atomic volume
d	=	grain diameter
Γ	=	grain boundary energy

The first quantitative model to describe the creep behavior in particle hardened alloys was developed by Ansell and Weertman.(58) Stresses are assumed to be well above the Orowan stress so that the rate controlling process is dislocation climb over second phase particles. The creep rate was derived to be:

eq. [18]

$$\epsilon' = (\pi\sigma b^3 D_s)/(2kTd^2)$$

D_s	=	self diffusivity
σ	=	stress
b	=	Burger's vector
d	=	particle diameter
k	=	Boltzman's constant
T	=	temperature

Since creep is a thermally activated process, it can be represented by an Arrhenius type equation. Lund and Nix(59,60) have developed such an expression describing creep rate in particle hardened alloys. Their expression compensates for the decrease in modulus at elevated temperatures and introduces the concept of a threshold stress, σ_o , which must be exceeded before the onset of creep

eq. [19]

$$\epsilon' = A[(\sigma - \sigma_o)/E]^n \exp(-Q/kT)$$

σ_o	=	threshold stress
E	=	Young's modulus
Q	=	activation energy
A	=	constant
n	=	stress exponent

The stress exponent, n , is typically 4-8 for pure metals and as high as 75 for dispersion hardened alloys.(59)

4. COARSENING BEHAVIOR OR DISPERSOID PARTICLES.

Aluminum alloys developed for elevated temperatures are required to be both strong and resistant to thermal degradation. Therefore, the dispersoids which strengthen these alloys must be thermally stable and resist coarsening at operating temperatures. Ostwald Ripening is a process in which small second phase particles dissolve and larger particles grow at their expense. The coarsening kinetics have been analyzed and models such as those developed by Lifshitz and Slyzov successfully predict coarsening rates.(61) For interface controlled particle growth, an applicable application is

eq. [20]

$$r_t^2 - r_o^2 = \frac{64\sigma kCVt}{81RT}$$

r_o = initial particle radius

r_t = particle radius at time t

t = time

T = temperature

σ = interfacial energy

k = reaction constant

V = molar volume of second phase

R = gas constant

C = equilibrium solubility in the matrix of the diffusing species

For diffusion controlled coarsening

eq. [21]

$$r_t^3 - r_o^3 = \frac{8\sigma DCVt}{9RT}$$

For diffusion controlled coarsening, the term DC controls coarsening. The smaller the DC, the more resistant the particles are to coarsening. The data presented in (11) indicates that Zr has the lowest diffusivity flux followed by Fe, Ti, and Mo. Alloys designed with these elements should therefore have low rates of coarsening.

TABLE 3. Diffusivities and Solubilities of Several Elements in Aluminum

	<u>C at%</u>	<u>D₀ m²/s</u>	<u>Q KJ/mol</u>	<u>Diffusivity (AT. %m²/s)</u>
Al-Zr	0.07	7.28	241	6.6×10^{-19}
Al-Fe	0.026	9.1×10^3	260	1.12×10^{-17}
Al-Ti	0.8	5×10^{-9}	108	3.86×10^{-17}
Al-Mo	0.07	1.04×10^{-11}	55	6.03×10^{-17}

The interfacial term, σ , is generally reported at 500mJ/m² for incoherent intermetallic interfaces and up to an order of magnitude smaller for coherent interfaces. Therefore, if the particles could be forced to be coherent, the coarsening rate would decrease.

The diffusion controlled coarsening behavior of Al₃Ti predicted by equation [21] using the data given in Table 3 is presented in Figure 1.7. The pronounced effect of temperature on particle coarsening illustrates the need to process these alloys at the lowest temperatures practicable. However, it should be noted that fine (0.02μm) particles are stable for extended periods of time at 300°C.

The fine grain size of MA aluminums may act to enhance coarsening since diffusion along grain boundaries and dislocations is substantially faster than through the matrix. Martin(53) presents an equation derived by Kirchner that describes particle coarsening along grain boundaries:

eq.[22]

$$r_i^4 - r_o^4 = \frac{9dD\sigma CVt}{32 ABRT}$$

$$A = 2/3 - \sigma_b/2\sigma + (1/3) (\sigma_b/2\sigma)^3$$

$$B = 1/21n(l/f)$$

$$d = \text{grain boundary thickness, 3 atom spacings}$$

$$C = \text{solute content in the grain boundary in equilibrium with an infinitely large particle}$$

$$D = \text{diffusion coefficient of solute along grain boundary}$$

$$\sigma_b = \text{grain boundary energy}$$

$$f = \text{the fraction of the grain boundary covered by precipitates}$$

5. ALUMINUM-TITANIUM SYSTEM.

Alloys based on the aluminum rich end of the Al-Ti system are discussed in this section with particular attention being given to current research efforts in alloy production, phase stability, and mechanical properties. The equilibrium peritectic phase transformation is discussed along with the possibility that two metastable phases form upon solidification and an intermediate metastable phase forms upon solidification and an intermediate metastable phase forms upon aging. Precipitate stability is discussed in light of Ostwald Ripening behavior. Room and elevated temperature mechanical property data are reviewed.

a. Phase Equilibrium. The Al-Ti binary phase diagram is characteristic of alloys of widely differing melting points: Al-660°C., Ti-1660°C. There are several peritectic phase transformations and high melting point intermetallics, e.g., Al₃Ti. The equilibrium phase diagram is presented in Figure 1.8. (62) It is a small region of the aluminum rich portion of the phase diagram that is of value in developing high temperature

aluminum alloys. Titanium is commonly alloyed with aluminum in amounts of 0.1 to 1.15 wt.% and used as a grain refiner. Consequently, the low titanium region of the aluminum-titanium phase diagram has been the subject of much scientific attention. A detailed portion of the diagram is presented in Figure 1.9.(63) A peritectic phase transformation occurs at 665°C. and 1.15 wt.% Ti: $\text{Liq.} + \tau \alpha$. The exact wt.% Ti contained in the first solid to form during the peritectic decomposition is reported to be between 1.15-1.3%.(63,64,65) At the transformation temperature, titanium solubility in the liquid is 0.12 wt.%.

(1) Microstructure. The equilibrium phases present at room temperature are fcc aluminum and bcc Al_3Ti . Numerous authors have investigated the solidification behavior of aluminum titanium alloys under near equilibrium conditions(66,67,68,69,). St. John(66) describes three types of Al_3Ti morphologies and classified them as Type A, B, and C. The type A morphology is dendritic with all arms in one plane and mutually perpendicular. This structure was observed when the alloys were solidified under conditions of low temperature gradients or at low solidification rates and high temperature gradients. Type B particulates are described as "star-like" and/or "petal-like" in appearance. This morphology was found only in dilute alloys or under very high growth rate conditions. The Type C Al_3Ti particles are dendritic: primary, secondary, and tertiary arms growth occurs in a variety of directions but is confined to one crystallographic plane. Type C morphology was observed for alloys containing 3.5 to 5.0 wt.% Ti and at all solidification rates.

Cisse' et. al.(69) studied the effect of solidification rate (1 to 100°C s^{-1}) on the morphology and composition of Al_3Ti . A plate-like structure was observed at slow cooling rates; however, as the solidification rate was increased, the Al_3Ti particles became progressively more petal-like in appearance. Using microprobe analysis, the titanium concentration gradient existed; however, the gradient was more pronounced at slower solidification rates.

(2) Crystallography. The structure of aluminum is face centered cubic with a lattice parameter of 0.405 nm. Mondolfo (64) reports Al_3Ti has tetragonal structure, space group $I4/mmm$, 8 atoms unit cell with $a = 0.3851$ nm and $c = .86$ nm.; density of 3.370 kg m^{-3} . This representation of the Al_3Ti crystal structure

is presented in figure 1.8.(70) Tsunekawa and Fine(71); and Hansen(65) report that Al_3Ti has a tetragonal lattice (DO_{22} type) with $a = 0.5435\text{nm}$, $c = 0.859\text{nm}$. This corresponds to a larger unit cell with $a = a\sqrt{2}$, but does not fit the unit lattice of the atom's numbers.(64) In the precipitation of Al_3Ti from a supersaturated solid solution, an intermediate metastable coherent phase has been reported $\text{Al}_3\text{Ti}'$. This phase is believed to be similar to the cubic $\text{Al}_3\text{Zr}'$ phase; space group $\text{Pm}\bar{3}\text{m}$; 4 atoms/unit cell.(64) The $\text{Al}_3\text{Zr}'$ forms as round particles changing to rods with a fan shaped pattern. The matrix-particle orientation is $(001)_p // (001)_{\text{Al}}$ $[100]_p // [100]_{\text{Al}}$.

Hashimoto et. al(72). Kobayashi & Miura are referenced in "REFERENCE 72" with Hashimoto have studied the crystallography governing the nucleation of aluminum on Al_3Ti . The orientation relationships discovered can be classified into two categories: those involving semicoherent interfaces and those of the "so called" pseudo(near)-coincidence interface for which Coincidence-Site Lattice (CLS) analysis applies. The most consistent with the pseudo (near)-coincidence model is $(111)_{\text{Al}} // (112)_{\text{Al}_3\text{Ti}}$, $[011]_{\text{Al}} // [110]_{\text{Al}_3\text{Ti}}$. However, under relatively fast cooling conditions an orientation more consistent with the semicoherent interface model is frequently observed, i.e., $(001)_{\text{Al}} // (001)_{\text{Al}_3\text{Ti}}$, $[100]_{\text{Al}} // [100]_{\text{Al}_3\text{Ti}}$. Note, this is the same relationship previously described for the $\text{Al-Al}_3\text{Zr}$ interface.

b. Non-equilibrium Solidification. Peritectic reactions are generally sluggish, and it has been reported that upon rapid cooling, these alloys form metastable phases. Two metastable phases reported are $\text{Al}_{17}\text{Ti}_4$ and $\text{Al}_{15}\text{Ti}_4$ (69,74); however, the crystal structures were not identified. Mondolfo(64) questions their existence because of "...doubtful evidence..." supporting the assertion. The nucleation of " α " aluminum is believed to involve these metastable phases since dendrites were observed to grow outwards from them.(74)

Cooled rapidly, metastable single phase aluminum can be attained. The cooling rate required to restrain phase separation is a function of composition. For an alloy of 0.15 wt.% Ti, the required cooling rate is about 1°C_s^{-1} and for a 0.7 wt.% Ti alloy, it is 150°C_s^{-1} . Figure 1.10 is a graphical representation of the results obtained by Kerr, Cisse, and Bolling(74) illustrating the effect of cooling rate on the titanium concentration trapped in solid solution. Extrapolating to cooling rates obtained during gas atomization, it is

found that 1.4 wt.% Ti(3.5 vol.% Al_3Ti) could be trapped in solid solution. However, other workers have reported that rapid quenching from the liquid, up to 5 wt.% Ti can be held in solution.(64)

An interesting point is that with hyperperitectic alloys, increasing the cooling rate increases the nucleation temperature(74,75). An approximation of the nucleation temperature and composition of the first solid to form can be obtained by extending the liquid-" α " line upward into the Liquid- Al_3Ti phase region, in direct contrast to eutectic transformations. Sufficient cooling rates may eliminate the equilibrium peritectic phases or metastable phases and hence rule out peritectic reactions and transformations.

c. Thermal Stability. The thermal stability of the aluminum titanium system containing 2 wt.% Ti was examined by microprobe and an etching techniques.(63) The etch, HCl (50ml), HNO_3 (25ml) CuCl_2 (1g), and H_2O (150ml), was sensitive to Ti content and causes relief of the titanium rich portion of the matrix leaving Al_3Ti intermetallic unaffected.

The Al_3Ti particles were found to be thermally stable up to 500°C . for 24 hours. Above 500°C , there is a tendency towards spheroidization. The intercellular microsegregation occurring during the peritectic transformation persisted even after annealing for 24 hours at 635°C . Based on their microstructural study, an approximate diffusion coefficient for Ti in Al was obtained at 635°C . : $2 \times 10^{-11} \text{cm}^2/\text{s}$.(63)

The interfacial energy is generally reported to be $500 \text{mJ}/\text{m}^2$ for incoherent intermetallic interfaces and up to an order of magnitude smaller for coherent interfaces. Therefore, if the particles could be found that were coherent, the coarsening rate would decrease. Therefore, efforts were undertaken to modify the lattice parameter of Al_3Ti with Zr to more closely match that of the aluminum matrix.(71) Both Al_3Ti and Al_3Zr have tetragonal structures.

TABLE 4.(71) The Lattice Parameters of Al_3Ti and Al_3Zr

Al	$a = 0.405 \text{nm}$	
Al_3Ti	$a = 0.5436 \text{nm}$	$c = 0.860 \text{nm}$
Al_3Zr	$a = 0.401 \text{nm}$	$c = 1.732 \text{nm}$

There is a 5% difference between the diagonal length of the (001) plane in a unit cell of Al_3Ti and twice the length of the lattice parameter of aluminum. The addition of Zr was found to improve the diagonal fit; however, the mismatch between a values is slightly greater. However, it remains an open question if the interfacial energy between the matrix and the intermetallic was reduced.

The effect of rare earth additions of Gd and Er on the thermal stability of aluminum titanium melt spun ribbon and the morphology of Al_3Ti was investigated.(76,77,78) Additions of Gd to arc melted buttons caused the formation of a ternary phase($\text{Al}_{23}\text{Ti}_2\text{Gd}$) which nucleated on and then incased the Al_3Ti phase.(77) For melt spun alloys, the authors found that Gd caused a uniform precipitation of the globular ternary phase in preference to the needle-like Al_3Ti .(76) Microhardness measurements made on annealed ribbon demonstrated a general hardness increase with alloying additions and an enhanced aging response.

Erbium additions to an Al-Fe-Ti melt spun alloy were found to cause the formation of a globular ternary Al-Ti-Er phase in preference to the needle-like Al_3Ti phase.(78) In order to assess the effect of Er additions on thermal stability, isochronal annealing experiments were conducted. The microhardness of the Er modified alloys was superior to the entire temperature range examined.

d. Mechanical Properties of PM Aluminum-Titanium Alloys. There exists only a limited of mechanical property data for aluminum-titanium alloys produced by powder metallurgy techniques because of production difficulties, e.g., high liquids temperatures. The alloy solidifies via a peritectic transformation which is inherently sluggish. In addition, the large temperature difference between the liquids and solids ($\approx 600^\circ\text{C}$) mandates extremely fast solidification rates in order to avoid coarse intermetallics.

Commonly used powder manufacturing techniques include: 1) mechanical alloying, 2) atomization, and 3) melt spinning. Pratt and Wittney attempted to atomize Al-Ti powders using their rotating disc process; however, their attempts to produce usable quantities of powder for consolidation were not successful.(11)

Al-Ti alloys have been successfully mechanically alloyed, consolidated, and tested by Novamet.(18) The al-4wt.% Ti they produced exhibited excellent mechanical properties. The elevated temperature tensile data is given below.

TABLE 5. Mechanical Properties of Mechanically Alloyed Al-4 wt.% Ti (18)

	<u>UTS(MPa)</u>	<u>YS(MPa)</u>	<u>% Elong.</u>	<u>% RA</u>
25°C.	382	326	10.5	29.5
232°C.	252	201	3.0	2-10
287°C.	210	182	5.5	11.5
343°C.	186	159	1-3	6-12

The steady-state creep rate at 232°C. and 193 MPa is 4.26×10^{-5} /hr. at 343°C. and 121 MPa it is 1.8×10^{-4} /hr.

The effect of thermal exposure on room temperature properties is minimal as detailed in Table 6.

TABLE 6. Effect of Thermal Exposure on the Mechanical Properties of Mechanically Alloyed Al-4 wt.% Ti (18)

	<u>UTS(MPa)</u>	<u>YS(MPa)</u>	<u>% Elong.</u>	<u>% RA</u>
No exposure	383	326	10.5	29.5
100 hr. at 232°C.	379	333	9.5	27.0
100 hr. at 343°C.	373	320	11.0	27.5

Inherent in the mechanical alloying process is the pick-up of oxygen and carbon by the aluminum powders. The typical amount of carbon and oxygen is 0.47 wt.% and 2.11 wt.%, respectively. The carbon and oxygen forms compounds such as Al_4C_3 and Al_2O_3 in significant quantities, i.e., ≥ 5 vol.%. No correlation was made as to the amount of Al_3Ti formed; however, if equilibrium conditions prevail, one would expect about 10 vol.%.

II. EXPERIMENTAL PROCEDURE

The description of the experimental work is provided in three sections: 1. Materials Processing, 2. Microstructural Characterization, and 3. Mechanical Property Evaluation. The materials processing section describes how the alloy powders were produced, consolidated, and extruded. The microstructural characterization section discusses the structure, morphology, and chemistry of the powder alloys. The final section, Mechanical Property Evaluation, describes the tests and procedures used to evaluate the alloys' hardness, tensile properties, and creep response.

1. MATERIALS PROCESSING.

Aluminum 4 and 6 wt.% titanium alloy powders were produced by inert gas atomization, mechanical alloying, and mechanical alloying the atomized powder alloys. The alloys were designated according to the powder production technique used and the amount of titanium: AT for atomized, MA for mechanically alloyed, and AM for atomized and mechanically alloyed. An organic antiwelding agent (stearic acid) was added to the mechanically alloyed powders to introduce carbon to the system. Note: great care should be exercised in mechanical alloying and powder handling because of the danger of powder explosion. The powders were then degassed, vacuum hot pressed, and extruded into round rod. A flow chart of the processing sequence is presented in Figure 2.1.

a. Powder Production. The inert gas atomized powders were atomized in helium and screened to - 325 mesh (- 44 μ m) in a nitrogen/trace oxygen atmosphere by Valimet, Stockton, CA. The powders were then stored in a sealed carton.

The mechanically alloyed powder was produced by Novamet, Wyckoff, NJ. Alcan 99.9% pure aluminum was mechanically alloyed with pure titanium to create a master alloy with a chemistry of Al_3Ti . The master alloy was then annealed for 24 hrs. at 1000°C in a vacuum in order to promote aluminide formation and homogenize the microstructure.

The annealed master alloy was then mechanically alloyed with pure aluminum. Two alloy powders were produced containing 4 and 6 wt. % Ti plus residual amounts of carbon, hydrogen, and oxygen from the 1-1 % wt. % stearic acid antiseizing agent added to prevent cold welding.

Half of the inert gas atomized alloy powders were mechanically alloyed using similar processing conditions as the mechanically alloyed powders. This procedure serves to homogenize the microstructure and introduce carbon and oxygen to the system. During processing, one wt. % stearic acid was added to AM4 powder and 1½ wt. % to AM6 powder.

b. Consolidation. The powder alloys were cold pressed into 10 Kg billets 0.15m in diameter and vacuum degassed at 427°C. The vacuum degassed billets were then enclosed in 1100 series aluminum powder and vacuum hot pressed at 493°C and 34 MPa. Excess aluminum canning material was removed prior to extrusion.

The powder alloy billets were heated to a nominal temperature of 410°C, transferred to a container at 316°C and extruded into 22mm diameter rod through a cylindrical die with a cone angle of 30°. The head and tail sections of the extrusions were removed prior to machining test specimens.

2. MICROSTRUCTURAL CHARACTERIZATION.

a. Chemical Analysis. The chemistry of the powders and the powder alloys were analyzed using standard wet analysis and atomic absorption techniques in order to assess aluminum, titanium, oxygen, and carbon levels.

b. Brunauer, Emmet, and Teller (BET) Analysis. A 3-point BET analysis was performed on the alloy powders in order to determine the specific surface area and the density of the actual powder particles. This technique involves passing a mixture of helium and nitrogen gas through a sample of powder sample cooled to liquid nitrogen temperatures. The amount of nitrogen which is absorbed during this process is released upon heating and its volume measured. From the volume of nitrogen adsorbed and the fact that one atom of nitrogen occupies $16.2 \times 10^{-20} \text{m}^3$, the surface area of the powder is calculated by

measuring the number of nitrogen atoms adsorbed by this value.

c. Thermal Analysis. Thermal analysis experiments were conducted using a DuPont 1090 thermal analyzer in conjunction with the appropriate module: differential scanning calorimeter (DSC), differential thermal analyzer (DTA), or dynamic mechanical analyzer (DMA). DSC/DTA heating curves were obtained at a heating rate of 10°C/min using a pure aluminum sample as a reference material. A metered flow of dry nitrogen gas kept the cell under a positive pressure.

DMA was used to assess the drop in shear modulus of the wrought alloys with temperature. For this test, rectangular specimens $7.62 \times 0.64 \times 0.32$ cm were machined. The ends of the specimens were securely fixed to the stationary and driving arms of the DMA. An oscillating bending moment was applied at the specimen's natural resonant frequency as the alloys were heated at a rate of 10°C/min. From the changes in the specimen's compliance and resonant frequency, the alloy's shear modulus was calculated and plotted against test temperature.

d. X-ray Diffraction. X-ray diffraction was utilized to identify the phases present in the powders and wrought alloys. It was also used to monitor the change in volume fraction of Al_3Ti resulting from thermal exposure. X-ray analysis was performed on a Rigaku DMAX B x-ray unit equipped with a $\theta/2\theta$ goniometer and a graphite monochromator. X-rays were generated using a copper tube operating at 50KV and 20ma. The scan rate was 1°/min and data was collected every 0.04 degrees.

The preferred crystallographic orientation of the alloy rod was assessed using the Schulz reflection technique. The Bragg angles for the reflection of x-rays from the (111) and (200) planes of fcc aluminum were calculated. The specimen was adjusted to make equal angles between the incident and diffracted x-rays. The specimen was rotated in its own plane about an axis normal to its surface and about a horizontal axis lying in the plane formed by the incident and diffracted x-rays. The intensity of the peaks were recorded, analyzed, and plotted in the form of (111) and (200) pole figures.

e. Optical Microscopy. The alloy powders were mixed with fine ground dially phthalate powder and

consolidated in a Buehler mounting press. The wrought alloys were mounted in a similar fashion. The mounted specimens were hand polished on successively finer grades of abrasive paper, i.e. 220, 320, 500, and 1000 grit. The samples were lapped using a 0.3 μ m and 0.05 μ m alumina slurry. The specimens were observed in the etched (e.g., Keller's) and unetched condition on a Bausch and Lomb Research II metallograph.

f. Scanning Electron Microscopy (SEM). An Amray scanning electron microscope equipped with an energy dispersive and wavelength length dispersive x-ray spectrometer was operated at 20kv in the secondary electron emission mode. The SEM was used to characterize the morphology of the alloy powders, the size distribution of aluminide dispersoids, and the fracture surfaces of the static mechanical test specimens.

g. Transmission Electron Microscopy (TEM). Thin foils of the materials were examined using a JEOL 100CX II transmission electron microscope operating at an accelerating voltage of 120kv. Samples were prepared for electropolishing by using a jeweler's saw in order to cut the rod into 0.6mm thick sections. Following hand grinding to 0.1mm, 3mm diameter disks were punched for electropolishing. Foils were prepared on a Struers twin jet electropolisher in a solution of 30% nitric acid and 70% methanol. The thinning conditions were 12v, 1.5ma, and a bath temperature of -30°C.

In addition, a Phillips 400 scanning electron microscope (STEM) operating at 120kv was used in conjunction with a Leveex energy dispersive spectrometer to help identify second phase particles.

h. Image Analysis. The size and distribution of dispersoids were characterized quantitatively by manual and computer assisted techniques. The fine dispersion of aluminides, carbides, and oxides observed by TEM were measured manually. Particle diameters were calculated by averaging their length and breadth.

A Cambridge Quantimet 970 was used in tandem with a high resolution video camera in order to analyze the microstructures of mounted and polished specimens observed by SEM. Particle diameters were calculated from the observed surface areas by assuming that the particles were spherical.

3. MECHANICAL PROPERTIES.

Mechanical tests were performed on the powder and consolidated alloys in order to evaluate their ambient and elevated temperature capabilities. The microhardness of the alloy powders' before and after isochronal annealing were measured; likewise, hardness and tensile tests were performed on the wrought rod after isochronal annealing. Elevated temperature tensile tests were performed in order to evaluate the at-temperature static properties of the alloys. Creep experiments were used to assess the long term load carrying capability of the alloys at elevated temperatures.

a. Hardness Measurements. Samples of the alloy powders were prepared for microhardness testing by mounting and polishing them in bakelite. An identical preparation technique to that described in the Optical Microscopy section (II-B-5) was employed. Measurements were made on a Tukon microhardness tester using a Knoop indenter and a 20g load. A minimum of 20 measurements were made per alloy and the results averages.

The hardness of the wrought alloys were measured on a Wilson Hardness machine using the Rockwell B scale. The alloys were prepared by grinding a flat on the surface using 400 grit paper.

b. Ambient Temperature Tensile Tests. Tensile tests were conducted in accordance with ASTM E8-81 on an Instron test machine. (79) All tests were conducted at a strain rate of $1.1 \times 10^{-4} \text{ s}^{-1}$. The tensile specimens were 100mm long and 13mm in diameter, Figure 2.2a. The reduced section was 37mm long and 6mm in diameter. Using a 25mm MTS extensometer, strain measurements were made and used to calculate Young's Modulus. In order to insure accuracy, 4 measurements per specimen were made at 90° intervals around each sample.

Notch tensile tests were performed using a modified tensile specimen having a sharp notch with a root radius of less than 0.017mm (ASTM E602-81) machined in the mid section of the sample, Figure 2.2b.

c. Elevated Temperature Tensile Tests. The elevated temperature tests were conducted in accordance

with ASTM E21-79(79) under similar conditions (e.g., test equipment, strain rate, and specimen geometry) as the ambient tensile tests. Tensile tests were conducted in a convection oven with temperature controlled to $\pm 2^{\circ}\text{C}$. The oven required 10-20 minutes to come to temperature equilibrium after the introduction of the sample. The specimens were held for 15 minutes prior to test initiation.

d. Creep. Creep experiments were conducted in accordance with ASTM E139-79 on specimens shown in Figure 2.2c.(79) An Applied Test Systems Inc. creep machine with an automatic self leveling arm and an automatic loading system was used. Temperature was maintained at $\pm 2^{\circ}\text{C}$ of the set point by using a convection oven with the control thermocouple attached at the mid section of the creep specimen. Strain was monitored using a dual extensometer LVT type electronics calibrated so that 2.54mm = 10,000 volts. Tests were terminated after 100 to 200 hours.

III. RESULTS AND OBSERVATIONS

Results of the microstructural and mechanical experiments conducted on (i) the aluminum titanium powder and (ii) the wrought aluminum titanium alloys AT, AM, and MA are reported in this section.

1. ALLOY POWDER MICROSTRUCTURAL CHARACTERIZATION.

a. Composition. The compositional analysis of the alloy powders and the master alloy are presented in TABLE 7. The masteralloy contains titanium in excess of that required to form stoichiometric Al_3Ti . The titanium content of the alloy powders ranges from 4.2 to 6.7 wt.%. The mechanically alloyed powders, AM6, MA6 and MA4, contain 0.6 to 1.4 wt.% carbon; however, AM4 has lower carbon content than the other mechanically alloyed powders; and AT4 and AT6 are essentially carbon free.

b. Phase Identification. The constitutive phases of the alloy powder were identified by x-ray diffraction and are presented in TABLE 8. Al_3Ti was detected in the AT and AM powders but not in the MA or unannealed masteralloy. Figure 3.1 illustrates the type of diffraction traces observed for the AT4, AM4, and MA4 powder alloys. Note, that no Al_3Ti peak is seen in MA4 trace.

The x-ray diffraction plots obtained for the annealed masteralloy and the as-received masteralloy are presented in Figure 3.2. The as-received masteralloy is observed to be a binary mixture of elemental aluminum and titanium with no observable intermetallics. After the master alloy is annealed, it transforms into a complex mixture of Al_3Ti , Al, Ti, and $Al_{24}Ti_{18}$.

c. Powder Morphology. The shape and topology of the alloy powders and their precursors, the Alcan aluminum and annealed masteralloy powders, are presented in Figures 3.3 to 3.6. As is typical of inert gas atomized powder, AT4 and AT6 are spherical, Figure 3.3. The ubiquitous plate-like morphology of mechanically alloyed powders is clearly evident in the AM and MA powders, Figures 3.4 and 3.5. However, the outline of highly deformed atomized powder is still observed in the AM powder flake, Figure 3.4. The Alcan aluminum powder, shown in Figure 3.6a, has a smooth surface and is either spherical or

tear-drop in shape. In sharp contrast, the annealed master alloy has a rough surface and a irregular shape, Figure 3.6b.

Results of the BET analysis for specific surface area and actual particle density are presented in Table 9. The AM6 powder has the lowest specific surface area, $0.16 \text{ m}^2/\text{g}$; and alloy AT6 has the greatest specific surface area, i.e., $0.45 \text{ m}^2/\text{g}$. No correlation was observed between the values of specific area; and powder type or composition. Powder density ranged from 2.67 to 2.79 g/cc. The densities of the alloys powders increases with titanium content, e.g., AT4 has a density of 2.74 g/cc and AT6 a density of 2.79 g/cc. Furthermore, the density of the alloy powders appears to be related to processing. The helium gas atomized powders have the highest density; the mechanically alloyed powders have the lowest density.

d. Optical Microscopy. Optical micrographs of the AT, AM, master alloy, and MA alloy powders are presented in Figures 3.7-3.10 respectively. The helium gas atomized powders, AT4 and AT6, have similar microstructures, Figure 3.7. The shape of the powder is that of a sphere and/or ellipse. Plate-like second phase structures of Al_3Ti are clearly visible and range in size from less than a micron to larger than $20\mu\text{m}$. However, comparing the microstructures of the AT6 and AT4, the AT6 powder appears to contain a higher population of Al_3Ti particles larger than $5\mu\text{m}$.

The microstructures of the atomized powders after mechanical alloying. AM4 and AM6, are shown in Figure 3.8. The microstructure is heavily cold worked with cracking observed at the periphery of the powder particles. Evidence, also, of particle-particle cold welding can be observed. However, the large plate-like particles of Al_3Ti seen in the AT alloy powders are not present. Instead, Al_3Ti particles less than $2\mu\text{m}$ in diameter are homogeneously distributed throughout the microstructure.

The microstructures of the as-received and annealed master alloy powders is presented in Figure 3.9. The as-received powder consists of a two phase lamella structure; the regularly spaced lamellae have a periodicity of $4\text{-}6\mu\text{m}$ and a thickness of $1\text{-}3\mu\text{m}$. The annealed master alloy has a similar lamella structure; however, the thickness of the second phase is much less than $1\mu\text{m}$.

The microstructures of the mechanically alloyed powders, MA4 and MA6, are presented in Figure 3.10. The microstructure consists of both coarse, e.g., $20\mu\text{m}$ and fine, $< 2\mu\text{m}$ second phase ellipsoidal particles inhomogeneously distributed throughout the powder particle. The shape of the powder particles are irregular with cracks running radially from their surface into the particles' interior. Furthermore, large amounts of metal flow and porosity is observed. The porosity being preferentially located at matrix/particle interfaces.

e. Thermal Analysis. The differential thermal analysis (DTA) thermograms of alloys, AT4, AM4, MA4, and the annealed Al_3Ti master alloy are shown in Figures 3.11 to 3.14 respectively. The thermal traces are conveniently divided into heating and cooling curves. Deviation of the plot from the horizontal in the upward direction indicates an exothermic reaction, (i.e., precipitation, solidification, recrystallization, and coarsening). Likewise, a downward deviation is indicative of an endothermic reaction, (i.e., melting and precipitate desolution).

Upon heating alloy AT4, two broad exothermic peaks are observed at 620 and 850°C separated by a sharp endothermic peak occurring at 660°C , Figure 3.11. The endothermic reaction is associated with the alloy powder melting. The exothermic peaks are believed to be the result of Al_3Ti coarsening and precipitation in the solid and liquid aluminum matrix. The energy released during coarsening of Al_3Ti from 0.1 to $3.0\mu\text{m}$ was calculated to be 1J/g . The energy associated with the precipitation of 2.5 vol. % Al_3Ti at 600°C was calculated to be 181J/g . This compares well with the energy of the first exothermic peak, 176J/g , measured via DTA. The cooling and reheating curves are apparently free from reaction except those associated with melting and solidification.

The broad low temperature, 620°C ., exothermic peak present in the DTA thermogram of alloy AT4 is not observed in AM4 and MA4, Figures 3.12 and 3.13. Furthermore, immediately following the aluminum melt endotherm, the thermograms of AM4 and MA4 exhibit well defined exothermic peaks. Upon cooling AM4 and MA4, only the exothermic solidification peak is observed.

The DTA thermogram of the annealed masteralloy is distinct from those of the alloy powders, Figure 3.14. Five exothermic peaks (370, 640, 700, 820, and 970°C.) and two endothermic peaks (660 and 1130°C.) are observed upon heating; however, no reactions are recorded during cooling.

2. ISOCHRONAL ANNEALING OF THE ALLOY POWDERS.

In order to assess the effect of thermal exposure on the mechanical and microstructural behavior of the alloy powders, isochronal (24hrs.) annealing experiments were conducted. Microhardness, x-ray diffraction, and optical microscopy were used to monitor structure/property variations with powder processing.

a. Microhardness. Results of the microhardness measurements for the AT, AM, and MA alloys are shown in Figures 3.15. In general, the alloys containing 6 wt.% Ti, Figure 3.15b, are harder than the 4 wt.% titanium, Figure 3.15a. The mechanically alloyed powders, MA and AM, are substantially harder than the AT powder over a wide range of annealing temperatures. The hardness of the AM and MA powders increases with annealing temperatures up to 400°C. Above 400°C, their hardness decreases. The hardness of the AT powders increases slightly upon annealing; however, unlike the mechanically alloyed powders, its hardness is not degraded with annealing at temperatures up to 600°C.

b. X-ray Diffraction. The relative intensities of the (200) Al_3Ti diffraction peaks normalized by the (200) and (111) aluminum peaks for the isochronally annealed AT4, AM4, and MA4 alloy powders are shown in Figures 3.16 to 3.18 respectively. In order to investigate the precipitation and coarsening behavior of the alloy powders, the (200) Al_3Ti diffraction peak was chosen because it is the second most intense reflection and is well separated from strong aluminum peaks. It can be observed that the relative intensity of the Al_3Ti peak increases with increased annealing temperature. After annealing at 600°C, the relative intensity of the Al_3Ti diffraction peaks of all the alloys are comparable.

c. Optical Metallagraphy. The optically resolvable microstructural features of the AT, AM, and MA alloy powders do not change appreciably upon annealing at temperatures up to 400°C. Annealing at 600°C did

cause a small amount of Al_3Ti particle spheroidization. The fact that no overt microstructural coarsening occurs upon annealing is in agreement with the diffusion coarsening theory as applied to $\text{Al}-\text{Al}_3\text{Ti}$ system and discussed in Section I.4. Coarsening Behavior of Dispersoid Particles.

3. MICROSTRUCTURAL ANALYSIS OF THE CONSOLIDATED ALLOY.

a. Compositional Analysis. Chemical analysis results of the extruded rod are presented in Table 10. The alloys prepared from inert gas atomized powder, AT4 and AT6, contained no carbon. Alloys AM6, MA6, and MA4 have carbon present in significant amounts i.e., 1.0 to 1.7 wt % carbon. Of the mechanically alloyed materials, alloy AM4 has the least amount of carbon, i.e., 0.6 wt. %.

The oxygen content of the alloys range from 0.1 to 0.6wt. %. On the average, the oxygen content of the MA and AM extrusions is 2 to 4 times that of the alloy AT4 and AT6, e.g., AT4 has 0.12wt. % O and AM4 has 0.58wt. % O.

The amount of titanium in the alloys varied from 4.7 to 6.8 wt. % and constitutes a deviation from the program's target values of 4.0 to 6.0 wt. % titanium.

b. Phase Identification. Phase identification of the alloys was accomplished by x-ray diffraction and selected area diffraction (SAD). There were four phases identified: fcc aluminum, bct Al_3Ti , hexagonal Al_4C_3 , and cubic $\gamma - \text{Al}_2\text{O}_3$; their distribution among the alloys is presented in Table 11. X-ray diffraction was unable to establish the presence of Al_4C_3 and Al_2O_3 ; therefore, SAD was used to verify their presence and determine their relative intensity. Al_4C_3 was found only in those alloys prepared from mechanically alloyed powder. Very weak indication of the $\gamma - \text{Al}_2\text{O}_3$ phase were found in all the alloys.

The volume fraction of each phase present was calculated based on compositional stoichiometry and is presented in Table 12. Alloys AM6, MA4, and MA6 have 4.8 to 8.1 vol. % Al_4C_3 ; whereas, AM4 contains only 2.9 vol. % Al_4C_3 .

The greatest amount of $\gamma - \text{Al}_2\text{O}_3$ is present in the mechanically alloyed materials, e.g., 0.3 to 0.9 vol. % Al_2O_3 . Alloys AT4 and AT6 contain approximately 0.2 vol. % Al_2O_3 .

The volume percent of Al_3Ti varies from 10.5 to 15.4 as titanium content increases from 4 to 6wt. %. However, unlike Al_4C_3 and Al_2O_3 , the volume fraction of Al_3Ti is not a function of the powder production route employed, i.e., atomization or mechanical alloying.

c. Optical Microscopy. The microstructures of the extruded AT, AM, and MA alloys are presented in Figures 3.19 to 3.21. The microstructures of alloys AT4 and AT6 are similar consisting of homogeneously distributed Al_3Ti particles ranging in size from less than a micron to $15\mu\text{m}$ or more in diameter. The microstructural features of the AM alloys resolvable by optical techniques are identical to those of the AT materials, Figures 3.19 and 3.20. In contrast, the microstructure of the MA alloys, Figure 3.21, are distinct from those of either the AT or AM materials. In the MA alloys ellipsoidal Al_3Ti particles 3 to $15\mu\text{m}$ in size are dispersed throughout the aluminum matrix; however, the finer $1\mu\text{m}$ size dispersoids present in the AT and AM alloys are absent.

The grain structure could not be examined using optical microscopy; however, prior powder particle boundaries were observed upon heavily etching with Keller's reagent. These should not, however, be misconstrued with actual grain boundaries. The grain size, $0.5\mu\text{m}$, of the alloys is too small to be resolved via optical microscopy.

d. Transmission Electron Microscopy (TEM). TEM examination of the extruded powder alloys was conducted before and after exposing the alloys for 100 hrs. at temperatures up to 400°C . Figures 3.22 and 3.23 show the microstructures of the as-received AT, AM, and MA alloys. The microstructures of the alloys annealed at 300°C for 100 hours are presented in Figures 3.24 and 3.25. Two morphologies of Al_3Ti particles are readily visible, i.e., spherical and grain-like.

A TEM bright field dark field pair of annealed alloy AM4 imaging Al_3Ti is presented in Figure 3.26 and is typical of Al_3Ti 's spherical morphology. The TEM micrograph of alloy AT4 presented in Figure 3.22.a also shows numerous examples of spherical Al_3Ti particles lining the grain boundaries.

The grain-like morphology of Al_3Ti can be observed in alloy AM6, Figure 3.23.b. A butterfly shaped, 0.2-0.4 μm sized Al_3Ti particle is located in the upper left corner of Figure 3.25b. Unlike spherical Al_3Ti , the contrast of the grain-like morphology is strongly dependent upon its orientation to the microscope's electron beam.

The size distribution of Al_3Ti particles in the alloys AT, AM, and MA before and after isochronal annealing are presented in Figure 3.27 and Table 13. The particles counted ranged in size from 0.01 to 0.05 μm . Prior to thermal exposure, the average particle diameter is 0.08 μm ; after annealing for 100 hrs. at 300°C, the average particle diameter increases to 0.11 μm . The distribution of particle in the 0.01 to 0.15 μm size range appears relatively unaffected by annealing. However, the number of particles counted in the 0.20 to 0.50 μm size range increases noticeably.

The finer dispersoids observed principally in alloys AM and MA and located primarily at grain boundaries have been identified as Al_4C_3 and $+\gamma - \text{Al}_2\text{O}_3$. Figures 3.22b&c and 3.23.b&c. The average size of these particles is estimated to be 0.01 μm .

The average grain size of the alloys measured before and after isochronal annealing are presented in Figure 3.28 and Table 14. The average grain size lies between 0.3 and 0.5 μm and appears to be unaffected by the 100 hour long thermal exposure of 300°C.

e. Alloy Texture. The (111) and (200) pole figures for the as-received extruded aluminum 4 wt.% and 6 wt.% Ti rod are presented in Figures 3.29 and 3.30 respectively. The maximum intensity of the (111) and (200) poles for each alloy is given in Table XV. The alloy rods all exhibit the (111) fiber texture typical of extruded aluminum alloys. However, alloys AT4 and AT6 have substantially higher pole intensities than do the AM or MA materials, e.g., the (111) pole intensity for AT4 is 16 and for MA4 is 5.

4. AMBIENT TEMPERATURE MECHANICAL PROPERTIES

a. Tensile Properties. The tensile properties of the as-received extruded aluminum-titanium alloys are

shown in Table 16. Mechanical property results are the average of 2-3 tests and demonstrated little property variability, i.e., the standard deviation corresponding to yield strength, tensile strength, and modulus variation ranged from 0 to 4%. The yield strength of the as-received AM and MA alloys range from 288 to 325 MPa and is about 140 MPa greater than the YS of the AT materials, e.g., AT6 180 MPa. The ultimate tensile strength of the mechanically alloyed materials, MA4, MA6, AM4, and AM6, range from 321 to 351 MPa; whereas, the UTS of alloys AT4 and AT6 are 230 and 220 MPa.

A measure of the work hardening is the difference between an alloy's UTS and YS. Using this criteria, the alloys may be listed in descending order of their ability to work harden: AT4, AT6, AM4, AM6, MA6, and MA4. The difference between the UTS and YS of alloy AT4 is 50 MPa, but reduces to 20MPa for MA4.

The ductility of the PM aluminium-titanium alloys is inversely related to their YS. The materials with the lowest YS, AT4 and AT6, have tensile elongations of 21 to 22%. The elongation of the strongest three alloys, MA4, MA6, and AM6, is 8 to 9% and the elongation of alloy AM4 is 15%.

The average Young's Modulus of the alloys (84.4GPa) is 15% greater than that of conventional high strength aluminum (70 GPa). The moduli of the AT and AM alloys range from 86 to 91 GPa and is significantly greater than that of the MA alloys, e.g., MA4, 74 GPa and MA6, 80 GPa.

Results of the notch tensile tests indicate that the alloys are not notch sensitive and may have superior toughness. The NT/UTS values range from 1.25 to 1.5. Alloys AT4, AT6, and AM4 have the highest NT/UTS values, i.e., 1.5 and alloy AM6 the lowest at 1.25.

b. Tensile Properties of the Annealed Rod. The tensile properties of the extruded alloy rod annealed for 100 hrs. at 200, 300, 400, and 500°C are presented in Table 17 and illustrated in Figures 3.31 to 3.34. The yield strengths (YS), Figure 3.31, and ultimate tensile strengths (UTS), Figure 3.32, of all the alloys do not degrade with 100 hour exposures up to 500°C.

In fact, YS and UTS increase when annealed and reach a maximum at about 300°C. For example, the yield strengths of AT6, AM6, and MA6 in the as-extruded condition are 180, 320, and 325 MPa respectively; however, after annealing at 300°C, the respective yield strengths increase to 190, 347 and 352 MPa.

Likewise, the ductility of the alloys are not seriously degraded with thermal exposure. The percent elongation and percent reduction in area remain relatively stable, Figures 3.33 and 3.34. The percent elongation of AT4 is 22% in the as-received condition, 23% after annealing at 300°C, and 24% after annealing at 500°C. The elongation of AM4 is 15% in the as-received condition, 15% after annealing at 300°C, and 7% after annealing at 500°C. In the as-received condition, MA4 has a 9.3% percent tensile elongation. After annealing at 300 and 500°C, the percent elongation of MA4 declines to 7.5% and 4% respectively.

5. ELEVATED TEMPERATURE TENSILE PROPERTIES

a. Tensile Properties. Tensile tests of the AT, AM, and MA alloys were conducted at 200, 300, and 400°C. The values for yield strength, tensile strength, percent elongation, and percent reduction in area are reported in Table 18 and illustrated in Figures 3.35 and 3.38. The AM and MA materials exhibit superior strength to the AT material over the entire range; however, the UTS and YS of the alloys converge at higher temperatures ($\approx 400^\circ\text{C}$), Figures 3.35 and 3.36. As one would anticipate, the AT alloys have superior ductility over the entire temperature range, Figures 3.37 and 3.38. It is worth noting, that AM4's properties are mid way between those for the mechanically alloyed material and those of the gas atomized powder alloys.

b. Dynamic Mechanical Analysis (DMA). In order to assess the effect of temperature on elastic modulus, DMA tests were performed at temperatures ranging from 25 to 400°C. Results of the DMA experiments are presented in Table 19. Shear Modulus, G, and the normalized shear modulus are presented in order to permit direct comparisons between alloys. Normalization is required because of the inherent sensitivity

of DMA to specimen geometry and test conditions. Results indicate that shear modulus is not affected by alloy type.

The normalized and averaged values of shear modulus for all the PM aluminum-titanium alloys are graphically presented in Figure 3.39. The average shear modulus at 400°C is 70% of its ambient temperature value. However, more than 90% of the ambient temperature shear modulus is retained at temperatures up to 200°C.

6. CREEP PROPERTIES

The test parameters for the creep experiments were established in light of elevated temperature tensile data. The AT alloys were excluded from the test because of their low elevated temperature strengths, e.g., AT4 has a yield strength of 75 MPa at 300°C. The alloys were tested at moderately high stress levels and homologous temperatures greater than $0.5T_{MP}$, e.g., 138MPa and 250°C. The effect of temperature on creep behavior was investigated by testing at temperatures ranging from 200 to 300°C, while maintaining a stress of 138MPa.

The creep strain versus log time response of the materials tested at 138 MPa are presented in Figures 3.40 and 3.41. At temperatures below 280°C, the plots of strain versus log time for the alloys AM6, MA4, and MA6 are linear. Therefore, their creep response is classified as logarithmic and is transient in nature. Alloy AM4 also exhibits logarithmic creep at temperatures below 250°C.

The creep resistance of the alloys ranked in descending order is AM6, MA4, MA6, and AM4. At any given time-temperature combination, alloy AM6 exhibited the smallest creep strain. For example, at a stress of 138 MPa and a temperature of 250°C, the 100 hour creep strains of AM6, MA4, MA6, and AM4 are 0.0034, 0.004, 0.005, and 0.0098 m/m respectively.

In order to assess the effect of stress on creep response, alloy AM6 was tested at two stress levels, i.e., 138 and 172 MPa. The creep strain versus log time response of AM6 is presented in Figure 3.42.

Increased stress levels and higher temperatures resulted in larger creep strains. Furthermore, a deviation from logarithmic creep is observed at 172 MPa and temperature above 280°C.

Creep rates of the alloys were calculated for the time interval between 50 and 150 hrs. and are presented in Table 20. At a constant stress of 138 MPa and at all test temperatures, alloy AM6 has the lowest creep rate. Increasing the test temperature from 220 to 280°C, doubles the creep rate of AM6, i.e., from $4.2 \times 10^{-9} \text{s}^{-1}$ to $8.7 \times 10^{-9} \text{s}^{-1}$. However, at 172 MPa, increasing the temperature from 220 to 280°C increases creep rate six fold, i.e., from $9.2 \times 10^{-9} \text{s}^{-1}$ to $63.4 \times 10^{-9} \text{s}^{-1}$.

The effect of Al_4C_3 on creep rate is presented in Figure 3.43. Al_4C_3 has little effect on creep at 220°C; however, at 280°C increasing the amount of Al_4C_3 by 3% doubles strain rate.

7. FRACTURE BEHAVIOR

Optical and scanning electron microscopy (SEM) were used to examine the microstructures and fracture surfaces of tensile and creep specimens. SEM fractographs of the AT, AM, and MA tensile samples tested at 25 and 300°C are shown in Figures 3.44 to 3.46. Macroscopically, all the tensile fracture surfaces examined had the typical cup and cone appearance of ductile tensile failures.

a. SEM Fractography of Alloy AT4. AT4 tested at room temperature has a dimpled fracture surface. The dimples range in size from less than $0.05 \mu\text{m}$ to greater than $3.0 \mu\text{m}$, Figure 3.44a. The fracture surface of AT4 tested at 300°C is distinct from that observed at ambient temperatures, Figure 3.44b. The appearance may still be described as dimpled; however, the dimples range in size from 2 to $15 \mu\text{m}$ and extensive local alloy deformation can be inferred from the dimple morphology.

b. SEM Fractography of Alloy AM4. Similar to alloy AT4, AM4 has a fine dimpled fracture surface. However, the dimples are smaller and more homogeneously distributed. At room temperature, the dimples range in size from 0.5 to $1.0 \mu\text{m}$, Figure 3.45a. The fracture surface of AM4 tested at 300°C has similarly sized dimples; however, the dimples are more highly deformed at room temperature, Figure 3.45b.

c. SEM Fractography of Alloy MA4. Tested at room temperature, alloy MA4 has large (0.5 by 4.0 μ m) rectangularly shaped holes dispersed throughout a fine (0.2 to 1.0 μ m) and homogeneously dimpled fracture surface, Figure 3.46a. The large holes are most likely the result of plates of Al₃Ti pulling away from the matrix during fracture. The rectangular holes evident in the fracture surface of MA4 tested at ambient temperatures are not seen after testing at 300°C, Figure 3.46b. Instead, the microstructure closely resembles that of AM4 tested at the same temperature: dimples are fine (0.5 to 1.0 μ m) and homogeneously distributed. However, deformation of the material comprising the dimples is less than that observed in alloy AM4 suggesting that MA4 has less local ductility.

d. Optical Metallography of Fractured Tensile Specimens. Optical micrographs, at the proximity of the fracture surface, of alloys AT6, AM6, and MA6 tensile tested at 25 and at 300°C are presented in Figures 3.47 and 3.48. Examination of these micrographs reveals no microstructural differences between the alloys tested at room temperature and at 300°C. This is not disconcerting since dispersoids resolvable by optical microscopy are unlikely to be affected by thermal exposure.

The microstructures of AT6 and AM6 are similar and consist of fine ($\leq 1.0 \mu$ m) homogeneously distributed dispersoids. The microstructure of alloy MA6 consists of inhomogeneously distributed fine ($\leq 1.0 \mu$ m) and coarse (5.0 μ m) dispersoids. Some of the larger particles are fractured; although, whether fracture occurred during tensile testing or during alloy processing is unclear.

Optical micrographs of creep specimens AM4, AM6, and MA6 tested at 250°C. and 138MPa for over 150 hrs. are presented in Figure 3.49. Comparing their microstructures to those of the tensile specimens, no differences can be readily observed.

In summary, SEM fractographic analysis indicates ductile failure modes are operative at both ambient and elevated temperatures. Macroscopically, the fractured tensile specimens have a cup-and-cone appearance. Cracks initiate within the specimen and failure occurs by microvoid coalescence. In addition, creep and tensile specimens examined via optical microscopy indicate that no overt microstructural changes occurred during deformation.

IV. DISCUSSION OF RESULTS

1. ALLOY POWDER

a. Morphology, Microstructure, and Phase Relationships. The powder production process employed controls powder shape, microstructure, and composition. Three types of powder production methods were used in this study: (i) inert gas atomization, (ii) mechanical alloying of elemental aluminum plus Al_3Ti , and (iii) mechanical alloying the inert gas atomized powders. Mechanical alloying is distinct from atomization and other solidification processes in that alloys are produced by solid state reactions, i.e., neither the alloy nor its elemental constituents are ever in the liquid state. In order to more fully appreciate the microstructural features of the powders, equilibrium solidification of aluminum-titanium alloys will be discussed briefly.

The equilibrium phase diagram for the aluminum-titanium alloy system is presented in Figures 1.8 and 1.9. Equilibrium solidification of a Al-6wt.% Ti alloy begins at a liquidus temperature of 1110°C when peritectic solid Al_3Ti nucleates. By the peritectic transformation temperature of 665°C , 16 wt.% of the liquid has transformed to coarse platelets of Al_3Ti . Cooled below 665°C , the liquid aluminum and part of the solid Al_3Ti transform by a sluggish peritectic reaction into solid aluminum containing 1.6 wt.% Ti. The microstructure now consists of 11 vol.% peritectic Al_3Ti and 89 vol.% Al. Cooled to temperature below 400°C , the equilibrium solid state solubility of titanium is nil; consequently, an additional 4 vol.% Al_3Ti precipitates.

The alloy powders, AT4 and AT6, were helium gas atomized and thus experienced cooling rates typical of conventional gas atomization, i.e., 10^4 $^\circ\text{C/s}$.(7) Clearly atomization is a nonequilibrium solidification process and based upon the experimental work of Kerr, Cisse, and Bolling, 1.6 wt.% Ti can be trapped in solid solution.(74) Furthermore, because of the limited solid state solubility of titanium in aluminum at room temperature, Al_3Ti would be expected to precipitate upon aging. However, given that 1.6 wt.% Ti is in solid solution aluminum, between 2.4 and 4.4 wt.% Ti has transformed to Al_3Ti , i.e., 6 to

11 vol.% Al_3Ti .

The morphology of the AT powders is spherical and is typical of inert gas atomized aluminum powders. Figure 3.3. The higher melt viscosity associated with titanium additions necessitated the pressurization of the tundish and the use of a large orifice. This may have resulted in the increased number of non spherical AT6 powder particles.

Powder particle agglomeration and agglutination is observed in Figure 3.3 and most likely result from the impact of partially solidified particles during atomization. The large number of such particles is not surprising because of the large temperature range and time during the solidification process, i.e. 450°C and 0.045s.

The microstructure of the AT4 and AT6 powder alloys are very similar and consist of a dispersion of Al_3Ti particles ranging in size from those optically unresolvable to greater than 20 μm , Figure 3.7. The presence of the larger plate-like Al_3Ti particles suggests that the cooling rates of gas atomization are insufficient and/or the melt temperature was below the liquidus temperature of the alloy. Cisse (69) reports that as cooling rates of aluminum-titanium alloys are increased from 1 to 100°C/s, the morphology of the Al_3Ti particles changed from plate-like to star-like. Therefore, the presence of the large plate-like Al_3Ti particles leads to the conclusion that the melt temperature was too low.

The morphology of the AM4 and AM6 alloy powders are presented in Figure 3.4 and their microstructures in Figure 3.8. The AM powders were prepared by mechanically alloying the inert gas atomized powders in the presence of an organic antiseizing agent. The plate-like appearance of the powder particles is indicative of the heavy amount of mechanical deformation received during the mechanical alloying process. However, despite heavy deformation prior particle boundaries of the AT powders can still be distinguished.

As one would expect, the microstructure of the AM powders appears similar to that of the AT powders. However, the large plate-like Al_3Ti particles present in the AT alloy powder are not readily

apparent in the AM alloy powder. Ostensibly, these large particulates are fragmented during mechanical alloying.

The mechanically alloyed powders, MA4 and MA6, were prepared by mechanically alloying Alcan aluminum powder with vacuum annealed Al_3Ti master alloy powder, Figure 3.6. The Al_3Ti master alloy powder was mechanically alloyed using a stoichiometric mixture of elemental aluminum and titanium powders. Prior to using the master alloy to mechanically alloy the MA powders, it was annealed at 1000°C in a vacuum.

The microstructures of the master alloy before and after annealing are presented in Figure 3.9. The two phase lamella structure of the master alloy powder was identified as titanium and aluminum by x-ray diffraction. After the master alloy was annealed, four phases were identified: fcc aluminum, hcp titanium, bct Al_3Ti , and bct Al_2Ti_8 . The microstructure of the annealed master consists of two macroscopically discernible structures, i.e., Al_3Ti separated by lamella of unreacted titanium.

The mechanically alloyed powders, MA4 and MA6, are plate-like in appearance, Figure 3.5. However, unlike the AM alloy powders, there is no evidence of prior particle boundaries. This is not surprising in light of the fact that ductile pure aluminum powder was used to prepare these alloys instead of prealloyed spherical powder.

The microstructure of the MA alloy powders is presented in Figure 3.10. The microstructure consists of fine and coarse particles inhomogeneously distributed in an aluminum matrix. X-ray diffraction indicates the presence of two phases: fcc aluminum and hcp Ti. The absence of Al_3Ti reflections can be rationalized as follows. (i) The substantial amount of unreacted titanium present in the master alloy powder significantly decreases the vol.% of Al_3Ti in the MA alloy powders, i.e., one atom of Ti reacts with three atoms of Al. (ii) Because the MA powders are heavily deformed, substantial x-ray line broadening is expected. Given the fact that the strong reflection of Al_3Ti are in close proximity to the stronger and broader peaks of aluminum and titanium, those of Al_3Ti may be entirely obscured.

b. Effect of Thermal Exposure. The alloy powders were annealed for 24 hours at temperatures up to 600°C in order to assess the effect of thermal exposure upon their microstructures and mechanical properties. The relative intensity of the (200) Al_3Ti x-ray diffraction peaks compared to the (111) and (200) peaks of aluminum for the alloy powders are presented in Figures 3.16 to 3.18. The relative intensity of the Al_3Ti diffraction peaks increase with annealing temperature indicating an increase in the volume fraction of Al_3Ti . No peak is observed for the MA powders until annealed at 400°C; however, when annealed at 600°C its intensity is equivalent to the AT and AM powders.

These results suggest that titanium trapped in solid solution during atomization precipitates during the thermal treatments of the AT and AM powders. The MA powders rich in titanium behave differently. The elemental titanium must combine with aluminum to form Al_3Ti via a solid state reaction involving interdiffusion. In any case, the increased amount of Al_3Ti should enhance mechanical properties.

The results of the microhardness measurements are shown in Figure 3.15. The microhardness of the AM and MA powders are substantially greater than those of the AT alloy powders over most of the temperatures tested. Upon annealing, the microhardness of all the alloy powders increases; however, exposures to very high temperatures decreases particle hardness. It is interesting to observe that the hardness of the AM and MA powders increases rapidly with temperature to 400°C and drops precipitously at 600°C. However, the hardness of the AT powders initially increases and decreases only slightly with temperature.

The microhardness results confirm that the volume fraction of Al_3Ti is increasing upon annealing. However, the fact that the hardness of the AM and MA powders increases more than the AT powders may be the result of other factors, e.g., the formation of Al_4C_3 and Al_2O_3 .

The carbon and oxygen content of the AM and MA alloy powders is substantially greater than that of the AT powders. The carbon and oxygen are byproducts of the decomposition of the stearic acid process control agent employed during mechanical alloying. The carbon and oxygen are believed to react with the

aluminum alloy to form Al_4C_3 and Al_2O_3 (24, 32, and 80).

The reactions associated with the decomposition of the organic process control agent and the subsequent formation of Al_4C_3 and $\gamma\text{-Al}_2\text{O}_3$ are complex, numerous, and believed to occur over a wide range of temperatures.(80,81) For example, Ovecoglu (81) has shown that the decomposition of Nopcowax (a common process control agent) occurs between 100 and 550°C. The amorphous carbides, oxides, and hydrides crystallize during powder degassing and consolidations to produce a dispersion of fine Al_4C_3 and Al_2O_3 particles.

The fine dispersion of oxides and carbides is therefore considered to be responsible for the increase in the microhardness of the AM and MA alloy powders. Also, the precipitation of Al_3Ti would be expected to result in a small increase in hardness comparable to that observed in the AT alloys. Elevated temperature exposures could result in the recovery, recrystallization, and grain growth of the alloy powders. Together, these factors tend to reduce the hardness of the powders exposed to high temperatures. However, their impact is expected to be small because recrystallization and grain growth are severely limited by the multitude of fine dispersoids and the free surfaces of the powder particles. It is more likely that the exposure of carbide and oxides to elevated temperature results in coarsening (32) and accounts for the decrease in microhardness at temperatures above 400°C. The energy stored during mechanical alloying is the origin of the alloys' fine grain size; however, the carbides prevent grain growth.

2. MICROSTRUCTURE OF THE EXTRUDED ROD

a. Composition. The chemical makeup of the extruded rod reflects the composition of the powders from which it was produced, Tables 7 and 10. Differences are most likely the result of statistical variations in powder sampling; and the accuracy and precision of the chemical analysis techniques employed, i.e., standard wet analysis, atomic absorption, and spectrographic analysis.

The carbon content of the rod appears to be directly proportional to the amount of stearic acid

process control agent used during mechanical alloying. There are several compounds commonly referred to as stearic acid, e.g., $\text{CH}_3(\text{CH}_2)_{16}\text{CO}_2\text{H}$ contains 76 wt.% carbon. The AT alloys were not mechanically alloyed and are carbon free. One weight percent stearic acid was added to the AM4 alloy powder. The extruded AM4 alloy has a carbon content of 0.62 wt.%, i.e., 2.9 vol.% Al_4C_3 . The average carbon content of alloys AM6, MA4, and MA6 increased to 1.33 wt.%, 6.2 vol.% Al_4C_3 , with the addition of 1% wt.% stearic acid. This compares favorably with the results of other authors. Benjamin and Bomford (28) added 1.85 wt.% stearic acid during the mechanical alloying of aluminum and achieved carbon levels of 1.53 wt.% in the final product.

b. Optical Metallography. The optical micrographs of the AT and AM alloys are similar in appearance. Figures 3.19 and 3.20. Particles range in size from 1 to 15 μm and are homogeneously distributed throughout the aluminum matrix. Unfortunately, the grain structure cannot be readily observed optically. In contrast, the microstructure of the MA alloys are coarse and inhomogeneous, Figure 3.21. The particles range in size from 3 to 15 μm and are inhomogeneously distributed throughout the alloy's microstructure.

However, despite the obvious microstructural differences between the AM and MA alloys their mechanical behavior are similar and distinct from the AT materials. This observation leads to the conclusion that the microstructural features controlling mechanical behavior are optically unresolvable.

c. Phase Identification. X-ray diffraction and TEM were used to ascertain the type and distribution of phases present in the microstructures of the extruded alloy rod. X-ray diffraction of the as-received alloys confirmed the presence of bct Al_3Ti but was unable to detect $\text{Al}_{24}\text{Ti}_8$, Al_4C_3 , and Al_2O_3 .

Selected area diffraction (SAD) established the presence of Al_4C_3 and $\gamma\text{-Al}_2\text{O}_3$ in the microstructures of the mechanically alloyed materials. Ring, not spot patterns were seen for Al_4C_3 phase even when the smallest diffraction aperture was used. This indicates that there is a high volume fraction of fine (0.01 μm) Al_4C_3 dispersoids having no preferential habit plane relative to aluminum. This is because the superlattice reflection of coherent particles produces a spot pattern oriented to the aluminum

matrix; coarse particles would produce a spot pattern; and a small volume fraction would not produce a visible and continuous ring pattern.

No other phases were identified. This may appear surprising considering that the major alloying element is titanium and titanium is known to react strongly with carbon and oxygen. In fact, Koczak et. al. (82) have demonstrated that TiC can be produced by melting these alloys in the presence of carbon. Recently, however, Banerji and Reif (83) evaluated the thermodynamic stability of TiC in the presence of Al_4C_3 . They concluded that Al_4C_3 was the stable phase at temperatures below 1000°C. Furthermore, TiO_2 does not form even though its free energy of formation is low (-178kcal at 600°C) because Al_2O_3 is even more stable, i.e., -222kcal at 600°C. (84) This thermodynamic stability holds over the entire temperature range of their existence.

d. Grain Size and Particle Distribution. The grain size and Al_3Ti particle size distributions for the AT, AM, and MA alloys are presented in Figures 3.27 and 3.28 and in Tables 13 and 14. The average grain size of the as-received material was measured to be $0.40\mu\text{m}$. Although the angular relationship between grains was never actually measured, it is believed that they are high angle boundaries based primarily on TEM observation of their microstructures and SAD patterns. When the TEM specimen is tilted, the contrast of a grain changes rapidly and distinctly from those of neighboring grains. Furthermore, the SAD pattern for aluminum is a set of continuous rings indicative of a fine grained material.

The average Al_3Ti particle size measured for the aluminum-titanium alloys was $0.08\mu\text{m}$ using TEM and $0.7\mu\text{m}$ using SEM. This difference may be explained in terms of the magnifications employed. TEM micrographs were taken at magnifications 50,000 to 140,000 whereas SEM micrographs were taken at magnifications of 1,000 to 5,000. The fine particles resolved via TEM could not be seen using SEM; likewise, the larger particles observed in the SEM either fall out of the specimen during electrolytic thinning or occupy the photographic field in the TEM at high magnifications.

The larger plate-like particles are the result of primary solidification of Al_3Ti and may be the result of atomization below the alloy's liquidus temperature. This particle morphology has been reported in the

solidified microstructure of aluminum-titanium alloys by numerous investigators.(66-69) The fine spherical particles are the result of solid state nucleation and growth during processing.

e. Microstructural Model. In order to more fully appreciate how the various microstructural features interact, an idealized model was developed. The model is based upon the average grain size and particle size data collected from optical, SEM and TEM techniques. The model accurately represents both the average size and spacing of microstructural features but does not account for feature shape, size variation and volume fraction.

Figure 4.1 is a graphical representation of the microstructural model. The left hand side represents the microstructure of the AM and MA alloys containing Al_4C_3 . The right hand side represents the microstructure of the AT materials. A cursory examination of the figure reveals that there are Al_3Ti particles as large as if not larger than the grain size, i.e., $0.4\mu m$. These large Al_3Ti particulates are spaced about $1\mu m$ apart. The spherical Al_3Ti particles $0.1\mu m$ in diameter are preferentially located along the grain boundaries and have a spacing of 0.2 to $0.7\mu m$.

The fine Al_4C_3 and Al_2O_3 particles present in the AM and MA alloys are also preferentially located at grain boundaries. These particles are $0.01\mu m$ in diameter and spaced about $0.04\mu m$ apart. In the next section, the mechanical properties of the alloys will be discussed in light of this microstructural model.

3. DISCUSSION OF MECHANICAL PROPERTIES

a. Tensile Strength. In this section, an attempt is made to establish what relationship exists between microstructure, composition, and tensile strength; and to correlate tensile test results to the various accepted strengthening models. However, difficulties arise when attempting to describe alloy strength based on the complex microstructures found in these PM aluminum titanium alloys. As described in the previous section, the microstructure consists of four phases present in a variety of morphologies, sizes, and volume fractions. This implies that the alloys' response could be a combination of what is typically found in dispersion strengthened, particle strengthened, or two phase aggregates composite materials.

Both shearable and nonshearable particle strengthening models were investigated, Section I.3.C. Particle Strengthening. Models based on shearable particles were eliminated early in the analysis because of several factors: 1. no evidence of particle matrix coherency was found, 2. no evidence of sheared particles was found, and 3. significant strengthening is predicted only for extremely fine particle and large volume fractions e.g., particle diameters much less than $0.01\mu\text{m}$ and volume fractions greater than 0.10.

Orowan strengthening, eq.[13], by dislocation looping of dispersoid was calculated using particle size data collected during image analysis. The results for the dispersion of Al_3Ti and Al_4C_3 are presented in Tables 21 and 22 and illustrated graphically in Figure 4.2. As can be seen from Figure 4.2, Al_3Ti contributes little to the alloys' strength and cannot be used to explain the differences in properties amongst the various materials.

In contrast to the results for the strengthening affect of Al_3Ti , a strong correlation was found to exist between the presence of Al_4C_3 and alloy strength, Figures 4.2 and 4.3. However, the predicted strength is two to three times as great as was actually measured. This may be the result of the inhomogeneous particle distribution at the grain boundaries. Or, this may indicate that the Orowan Strengthening model is not strictly applicable to these alloys.

Despite the small effect of grain size on conventional aluminum alloys' strength, it was investigated as a possible strengthening mechanism. Alloy strength plotted against the inverse square root of grain size was found to form a straight line as predicated by the Hall-Petch model, Figure 4.4. The Hall-Petch slope was calculated to be $165\text{GPa}/\sqrt{\mu\text{m}}$. This is in excellent agreement with the value reported in the literature for conventional aluminum alloys e.g., for Al-Mg-Zn alloys: $120\text{-}220\text{GPa}/\sqrt{\mu\text{m}}$ (85) and for Al-Cu alloys $75\text{-}125\text{GPa}/\sqrt{\mu\text{m}}$ (47).

The alloys' strength is then seen to be strongly related to grain size and Al_4C_3 dispersoids but weakly to the presence of Al_3Ti . By examining the microstructural model presented earlier in Figure 4.1, the spacing of the large and small aluminides are seen to be of the same dimension as the grain size:

consequently it is unlikely that mechanism involving dislocation bowing around the aluminides contribute to the alloys' strength significantly. Furthermore, since the carbides and oxides are concentrated at the grain boundaries, it is likely that Orowan type calculations which assume a homogeneous distribution of particles would overestimate their strengthening effect.

Therefore, it is concluded that the primary effect of the dispersoids is to inhibit grain growth and thus increase strength via the Hall-Petch mechanism. The inhibition of grain growth by second phase particles can be estimated using the Zener relationship.

eq. [23]

$$\text{grain size} = 1.33 \alpha r f$$

α	=	constant
r	=	particle radius
f	=	volume fraction particulate

The fine size of the carbides and aluminides make them effective in controlling grain growth in the MA and AM materials. In the absence of carbides in the AT alloys the aluminides, which are an order of magnitude greater in size, must control grain size.

The strength of the mechanically alloyed materials, AM and MA, is 100 to 120 MPa greater than that of the rod produced from the prealloyed powders, Table 16 and 17. This can be related directly to the presence of fine carbides and oxides present in their microstructure. However, no relationship was found to exist between strength and the volume fraction of Al_3Ti particulates.

b. Ductility. The helium gas atomized alloys (AT) exhibited the best ductility: 21-22 % elongations and 33-41 % reduction in area, Table 17. The AM and MA materials had elongations of 8-12 % and reduction in areas of 20-29%. The reduced ductility of the AM and MA alloys is directly associated with the presence of the fine aluminum carbide and aluminum oxide particles which decorate their grain boundaries. This assertion is supported by the fact that the AT materials which exhibit good ductility are

essentially carbide free. Also, alloy AM4 has half the carbon content and nearly twice the ductility of the other Am and MA alloys, Table 10.

Annealing for 100 hrs at temperatures as high as 500°C does not affect ductility significantly. There is a slight (1-2%) decrease in elongation of the Am and MA alloys after annealing at 300°C and a commensurate 10 to 20 MPa increase in yield strength. This result corresponds to the microstructural observation that grain size and particle size remain basically stable during thermal exposure; and that Al_3Ti , Al_2O_3 , and Al_4C_3 particle precipitate during annealing.

c. Notch Tensile Strength. The PM aluminum-titanium alloys all exhibit excellent notch tensile strengths as indicated by their NT/UTS ratios given in Table 16. The NT/UTS ratios range from 1.2 to 1.5. Values less than one are associated with alloys that are notch sensitive and values greater than one indicate superior toughness in high strength aluminum alloys.

The presence of a sharp notch in the gage section of the test sample acts as a stress riser creating a complex triaxial stress state below the root of the notch. Evoking either the Tresca or Von Mises criteria for the onset of yielding it can be shown that the onset of plasticity is suppressed to higher axial stress levels. Corresponding to the increase in strength is an increase in the hydrostatic component of stress. Alloys exhibiting poor matrix particle bonding would tend to fail at the interface under such hydrostatic stresses. Likewise, microvoid coalescence at the interface of any variety of microstructural features eventually leads to failure.

The high levels of NTS TS can then be attributed to good matrix particle bonding, a clean aluminum grain structure, and a fine (0.5 μm) grain size. The homogeneous grain structure helps to distribute the stresses evenly and the ductile aluminum grain interior is able to accommodate local strain incompatibilities at the particle matrix interfaces.

d. Elastic Modulus. The modulus of aluminum alloys is generally considered to be insensitive to microstructure, composition and processing history. However, it is known that the development of

preferred crystallographic orientation (texture), the presence of second phases, and the addition of certain alloying elements can affect elastic modulus.

The results of the microstructural and crystallographic investigation of the aluminum titanium alloys studied suggest that a complex synergistic relationship exists between modulus, texture, particles and composition. Young's modulus is observed to increase from 80 to 90 GPa as the intensity of the (111) pole increased from 2 to 22, Figure 4.5. Modulus also increases from 75 to 90 GPa as the volume percent of Al_3Ti is increased from 10.5 to 15, Figure 4.6 although, no correlation was observed between modulus and the volume percent of Al_4C_3 and Al_2O_3 . The development of texture, however, is curtailed by the presence of second phase particle. Figure 4.7 illustrates how the presence of Al_4C_3 reduces the amount of preferred orientation: similar correlations can be made for both Al_2O_3 and Al_3Ti .

Three models have been employed to describe the elastic behavior of dispersion and particle reinforced matrices. (86) The first and most widely cited is the so called "rule of mixtures" whose derivation assumes that both the matrix and reinforcing particulate phases are equally strained (isostrain model). (87) The second model was formulated by assuming that the matrix and particles are subject to the same stress levels (isostress model); (88) and the third model is the average of the isostrain and isostress models' results. (89)

The isostrain and isostress models are conveniently described by the following equation:

eq[24]

$$E^m = \sum f_i (E_i)^m$$

- E_i = elastic modulus of component "i"
 f_i = volume fraction of component "i"
 m = constant; $m = 1$ for the isostrain model
 and $m = -1$ for the isostress model.

The value for Young's modulus obtained from the isostrain model constitutes an upper limit and the

isostress model provides a lower limit. The actual values lies somewhere in between.

In order to estimate the modulus of the Al_3Ti particulate phase, the rule of mixture model was used. The use of this model is justified only if there is good bonding between the particulates and the matrix; and the matrix is sufficiently ductile to withstand the high local stresses which develop at the particle/matrix interface. Fine (90) found that the rule of mixtures model provided a satisfactory description of the elastic modulus for the $Al-Al_6Mn$ system in which the particle and matrix are well bonded. However, Fine's analysis of Lyle's (91) data indicates that the isostress model is applicable to the $Al-Al_2O_3$ system in which there is poor bonding between particles and matrix. Consequently, the addition Al_2O_3 has little effect on the alloy's modulus. The results of the notched tensile tests and microstructural evaluation indicate that the criteria necessary for the use of the rule of mixtures model are satisfied.

The modulus of the Al_3Ti phase was calculated using the mean value for particle volume fraction and alloy modulus; the modulus of aluminum matrix was assumed to be 70GPa. The modulus of the aluminide was computed to be 177.6 GPa and reflects a 2.5 GPa increase in the alloy's modulus for each wt. % Ti. This value agrees well with Mondolfo who reports a 2.6 GPa increase per wt. % Ti. (64) Although the modulus values for Al_3Ti are not available in the literature, Holowach and Redder (92) measured the moduli of Ti_3Al and $AlTi$ to be 144.8 and 175.9 GPa respectively. Based upon the above discussion, 177.6GPa appears to be a reasonable value for the modulus of Al_3Ti .

4. TENSILE PROPERTIES OF THE ANNEALED ROD

a. Strength. The strength of the aluminum-titanium alloys increases moderately (≈ 20 MPa) with annealing to temperatures of about 300°C. Figures 3.31, 3.32. Both the inert gas atomized and mechanically alloyed materials experience identical strength increases.

Microstructural features such as grain size and particle diameter do not change significantly with exposure to 300°C. Table 13 and 14. Therefore, their impact on strength changes is dubious.

The increase in strength may be the result of either Al_3Ti precipitation or the continued reaction of residual carbon and oxygen with the aluminum matrix to form Al_4C_3 and Al_2O_3 . The latter explanation does not appear valid since the strength of both the mechanically alloyed and inert gas atomized materials increases. That is, only the mechanically alloyed materials have carbon and oxygen in sufficient quantities to affect mechanical properties.

The precipitation of Al_3Ti has been shown to occur in the alloy rod at temperatures up to 600°C . Figures 3.16 to 3.18. The increase in strength is, therefore, attributed to Al_3Ti precipitation.

At annealing temperatures above 400°C , the strength of the alloys decreases. This is attributable to the increase in grain size and particle coarsening. The average grain size increases from $0.4\mu\text{m}$ to $0.7\mu\text{m}$ and although the coarsening rate of Al_3Ti is expected to be slow, Al_4C_3 is known to coarsen rapidly at these temperatures. (32)

b. Ductility. The percent elongation and percent reduction in areas of the annealed alloy rods are presented in Figures 3.33 and 3.34. The ductility of all the alloys declines with increased annealing temperatures. The ductility of the inert gas atomized alloys are higher than those of the mechanically alloyed rod over the entire temperature range.

The carbon content and ductility of alloy AM4 lies between the atomized alloys, i.e., AT4 and AT6; and the mechanically alloyed materials prepared using 1-1/2 wt. % stearic acid, i.e., alloys AM6, MA4, and MA6. The volume fraction Al_4C_3 for all the alloys is given in Table 12. Correlating the amount of Al_4C_3 to tensile elongation for each alloy it is seen that elongation is inversely related to Al_4C_3 content.

The decline in ductility with increased annealing temperature can be correlated to microstructural changes. The Al_4C_3 , Al_2O_3 , and Al_3Ti particles coarsen and as a result grain growth occurs. The toughness and ductility of high strength aluminum alloys is known to decrease with grain size. (53) Therefore, it is concluded that an increase in grain size, as a result of particle coarsening, effects a modest decline in alloy ductility.

5. ELEVATED TEMPERATURE TENSILE PROPERTIES

The yield strengths (YS) and tensile strengths (UTS) of the aluminum-titanium alloys tested at temperature are presented in Figure 3.35 and 3.36. The strength of the alloys all decline with temperature and their strengths relative to each other remain fixed up to 300°C. Above 300°C, tensile properties tend to converge.

The room temperature properties of these alloys have been shown to be dependent on grain and particle size. There is a synergistic relationship between these microstructural features which inhibit dislocation motion. At temperatures greater than $0.5T_m$ (193°C), however, dislocations are able to climb over obstacles as well as bow around them. Furthermore, grain boundary deformation mechanisms become more pronounced and the fine grain size of these materials would be expected to weaken the alloy.

The accepted models relating grain size (dislocation density) and particle distribution to yield strength are all proportional to the shear modulus of the matrix, e.g., eq. [5] and eq. [13]. Consequently, a decline in the shear modulus of aluminum would effect a reduction in alloy strength. Shear modulus data presented by Mondolfo (64) for aluminum indicates that G at 200°C is 80% of that at 25°C. The uniform drop in strength with temperature up to 200-300°C, thus, may be attributed to the decline in the shear modulus of aluminum with temperature.

Above 200°C, nonconservative dislocation motion is possible. Dislocations are no longer restricted to the (111)<110> slip systems but can climb over obstacles by thermally activated process, e.g., vacancy diffusion. In addition, because Poisson's ratio increases with temperature other slip systems become active, e.g., (100)<110>. (93) Grain boundary deformation becomes important. Fine grained alloys experience grain boundary sliding and rotation. Combined, these factors greatly reduce alloy strength.

The ductility of the alloys generally increases with temperature. The lower ductility associated with the AM and MA alloys is attributed to the presence of grain boundary oxides and carbides. The presence

of grain boundary dispersoids is believed to inhibit diffusional flow and grain boundary sliding. (94)

6. CREEP

This section addresses the results of the creep experiments. Prior to commencing this discussion it is useful to cite the various deformation mechanisms associated with creep.

Creep is by definition a slow deformation process. Typically, creep is studied at high temperatures, low stresses, and under constant load conditions. Plots of creep strain versus time are generated and usually can be divided into three regions: primary creep, secondary creep, and tertiary creep. The primary and tertiary creep portions of the curve are transient in nature and are usually ignored. Secondary creep (steady state creep) is the most highly studied type of creep. This region is associated with a dynamic balance between work hardening, recovery, and recrystallization.

Four types of deformation strains are associated with creep: elastic (ϵ_e), anelastic (ϵ_a), instantaneous plastic (ϵ_p), and time dependent plastic (ϵ_{ip}) strain. The elastic and anelastic strains are recoverable and are generally ignored in the study of high temperature creep. Elastic and anelastic behavior only dominate at low temperatures ($T < T_{mp}$) and stress below the Orowan's critical shear stress.

a. Logarithmic Creep. Logarithmic creep is a low temperature ($T = 0.5T_{mp} = 193^\circ\text{C}$) and moderate stress form of time dependent plastic deformation. Under stress, the alloy work hardens and dislocations multiply. Dislocation interactions inhibit slip and because the temperature is low, nonconservative dislocation motion is curtailed. The equation governing this type of behavior is

eq. [25]

$$\epsilon = \epsilon_e + \epsilon_p + \epsilon_o \log(1 + \alpha t)$$

$$\epsilon_o = \text{constant}$$

$$\epsilon_p = \text{instantaneous plastic strain}$$

$$\epsilon_e = \text{elastic strain}$$

t = time
 α = time constant

This form of creep is classified as transient because creep rate continuously decreases with time.

b. High Temperature Creep. The strains associated with high temperature creep encompass elastic, plastic, anelastic, and time dependent deformation. Because of the transient nature of the former, the time dependent deformation processes are of more significance. The basic equation governing high temperature creep is (95).

eq. [26]

$$K = C (\sinh B\sigma)^n \exp(-Q/kT)$$

or more simply

K = $\dot{\epsilon} \exp(-Q/kT)$
 K = creep rate
 σ = stress
 Q = activation energy for creep
 k = Boltzmann's constant
 T = temperature

C, B, and n are constants

For pure aluminum, the stress exponent, n, has a value of 4 or 5; however, for dispersion strengthened aluminum alloys this exponent can be as high as 75. (59) The activation energy for creep, Q, is that of self diffusion, e.g.; 120KJ/mol. (38) At lower temperatures, however, the activation energy for creep is related to that of grain boundary diffusion, i.e., 60KJ/mol. (38)

c. Nabarro-Herring-Coble Creep. A special kind of steady state creep can occur in fine grained alloys. i.e., less than 100 μ m. During elevated temperature creep, grains tend to elongate and diffusion is necessary to accommodate the deformation process. Nabarro and Herring developed a model for high

temperature creep dominated by matrix diffusion., Steady state creep rate is proportional to lattice diffusivity and inversely proportional to the grain size squared. Coble developed a model for low temperature creep dominated by grain boundary diffusion. Coble creep is proportional to grain boundary diffusivity and inversely related to the cube power of grain size. At intermediate temperatures both Nabarro-Herring and Coble creep may be appreciable.

d. Creep Behavior of PM Aluminum-Titanium Alloys. The strain versus log time creep curves for the aluminum-titanium alloys tested at 138 MPa are presented in Figures 3.40 and 3.41. Figure 3.42 illustrates the effect of increasing stress from 138 to 172 MPa on the creep response of alloy AM6. Also, the creep rates as measured between 50 and 150 hours are given in Table 20.

The linear nature of the majority of creep strain versus log time curves indicates that the creep behavior is logarithmic. As discussed previously, logarithmic creep is transient in nature. Its cause is associated with localized thermal fluctuations within the specimen which result in stress gradients. However, work hardening and dislocation multiplication result in a continuously decreasing creep rate.

Normally, the presence of dispersoids would be expected to decrease the rate of logarithmic creep because of increased dislocation particle interaction. However, Figure 3.43 clearly illustrates that creep rate is increased by the presence of Al_4C_3 particles. Consequently, another microstructural feature must be of greater significance. The grain sizes, particle sizes, and particle volume fractions of the alloys are similar. Therefore, it is not disconcerting to find that a strong correlation between creep rate and those microstructural features does not exist.

The synergistic relationship between the quantity of Al_4C_3 dispersoids and texture was discussed in Section IV. 3. d. with regards to elastic moduli. Essentially, as the amount of Al_4C_3 increases, the degree of preferred crystallographic orientation (texture) decreases, Figure 4.7. The effect of texture on creep rate is shown in Figure 4.8. As the amount of (111) fiber texture increases, creep rate decreases; therefore, it is suggested that the presence of dispersoids causes a decrease in texture and the decreased texture promotes logarithmic creep rate.

V. SUMMARY

This section is designed to both summarize and clarify a number of issues arising from this research. In particular, the relative contribution of Hall-Petch and Orowan strengthening on ambient temperature mechanical properties are discussed. The influence of particle type, size, and volume fraction on alloy properties are reviewed. At elevated temperatures, it is shown that Coble and Nabarro-Herring creep are suppressed by the presence of grain boundary dispersoids. Lastly, the properties of PM aluminum-titanium alloys are compared with state-of-the-art materials.

1. AMBIENT TEMPERATURE PROPERTIES

a. Hall Petch and Orowan Strengthening. The strength of the PM aluminum-titanium alloys is primarily derived from their fine ($0.5\mu\text{m}$) grain size. The fine grain size is the result of the 0.01 to $1.0\mu\text{m}$ diameter dispersion of aluminides, carbides, and oxides preferentially located at the grain boundaries. Dispersoids within the grain also enhance strength by impeding dislocation motion and improve ductility by providing a continuous source of dislocations.

Figure 5.1 is a plot of log yield strength versus log grain size for the aluminum-titanium alloys and commercially pure aluminum. The commercially pure aluminum was cold rolled 70% and recovery annealed to achieve the strengths and grain sizes indicated(96). The linear nature of the plot indicates that grain boundary strengthening is operative.

Yield strength versus inverse square root grain size is plotted in Figure 5.2. The differences between the extrapolated values of aluminum-titanium alloys can result from numerous secondary strengthening effects, e.g., (a) the relative number of high to low angle grain boundaries, (b) Orowan strengthening, and (c) the increased mean matrix stress due to the presence of particles. In summary, the ambient temperature properties are the result of (i) Hall-Petch strengthening and (ii) Orowan strengthening.

b. The Role of Oxides, Carbides, and Aluminates The variety of particle sizes, types, and volume fractions make it extremely difficult to isolate the individual contribution of a dispersoid to an alloy's over-all strength and creep properties. However, unambiguously the primary effect of the particles is to prevent grain growth beyond that predicted by Zener's relationship, i.e., equation [23]. Zener's relationship predicts that the maximum grain size is proportional to particle radius and inversely proportional to particle volume fraction. Consequently, fine dispersoids present in high volume fractions have the most significant impact on grain size.

Al_4C_3 plays a major role in the strengthening of the aluminum-titanium alloys because of its fine size, e.g., $0.01\mu\text{m}$ and high volume fractions, i.e., 0.03 to 0.08. Al_2O_3 particles have the same size as Al_4C_3 but have very low volume fractions and therefore alter alloy properties less dramatically. Al_3Ti is present in volume fractions ranging between 0.1 to 0.15; however, its mean particle diameter is 100 times greater than that of Al_4C_3 and Al_2O_3 . Consequently, the strengthening effect of Al_3Ti is only apparent in the carbon free alloy, e.g., AT6 and AT4. From Figure 5.2, the strength increase is estimated at 20-60 MPa.

Dispall is the trade name of a family of mechanically alloyed aluminum-carbon-oxygen alloys which exhibit excellent ambient and elevated temperature mechanical properties.(30) Dispall's properties are achieved solely by the addition of oxygen and carbon to aluminum; and therefore, make an interesting and useful comparison with the Al-Ti-C-O alloy.

Table 23 presents some of the properties of PM Al-Ti, Dispall, and mechanically alloyed Al-4Ti (83089) reported in another study.(30,18) Dispall's strength increases and elongation decreases with increasing carbon content. The UTS of the carbon free AT6 is 60 MPa greater than Dispall 0 (0 wt.% C). Likewise, the UTS of AM6 (1 wt.% C) is 116 MPa greater than Dispall 1 (1 wt.% C). Therefore, Al_3Ti appears to contribute in a secondary manner to the alloy's strength. However, because the grain size of Dispall ($0.6\text{-}1.5\mu\text{m}$) is greater than that of PM aluminum-titanium the precise contribution of Al_3Ti is unclear. In addition, because the elongations of the Dispall and PM Al-Ti alloys are similar, it may be concluded that Al_3Ti does not seriously degrade ductility.

TABLE 23. Ambient Temperature Mechanical Property Comparison

<u>ALLOY</u>	<u>YS, MPa</u>	<u>UTS, MPa</u>	<u>% ELONG.</u>	<u>E, GPa</u>
DISPAL* 0	--	160	25	70
DISPAL* 1	--	235	20	70
DISPAL* 2	248	311	10	70
DISPAL* 3	--	380	6	70
83089**	326	383	10	--
MA6 +	325	347	8	80
AM6 + +	321	351	9	87
AT6 + + +	180	220	21	88

* Numeral designates carbon content in wt.%; alloys contain between 0.4 and 2.5 wt.% oxygen

** AL-4Ti-(2.11)0-0.47C; Inco alloy produced via mechanical alloying

+ Al-5.6Ti-1.7C-(0.6)0

+ + Al-6.2Ti-1.0C-(0.2)0

+ + + Al-5.9Ti-(0.2)0

The elastic moduli of the Dispall alloys is that of commercially pure aluminum, i.e., 70 GPa. Dispall contains about 15 vol.% Al_4C_3 and Al_2O_3 dispersoid which do not significantly enhance the alloys' moduli. However, the moduli of the PM Al-Ti alloys are significantly greater than that of pure aluminum, e.g., the modulus of AM6 is 24% greater. The inference is that Al_3Ti and extrusion texture are responsible for the increased elastic modulus.

The Inco alloy, 83089, has properties similar to alloys AM6 and MA6, i.e., yield strength of 326MPa and tensile elongation of 10%. However, alloy 83089 contains more oxygen and less carbon than AM6 and MA6. This suggests that the roles of Al_4C_3 and Al_2O_3 dispersoids are similar and that identical mechanical properties can be achieved using various combinations of oxygen and carbon.

2. ELEVATED TEMPERATURE MECHANICAL RESPONSE

The high temperature mechanical properties of the PM aluminum-titanium alloys, like their ambient properties, are dominated by the alloy's fine, stable, grain size. The fine grain size does not deteriorate elevated temperature properties because the grain boundary dispersoids appear to effectively inhibit dislocation glide and climb. The creep rates predicted by several deformation models are reported in Table 24 for pure aluminum under conditions of: (1) an applied stress of 138 MPa, (2) a temperature of 250°C, (3) a grain size of 0.5 μ m, and (4) a particle size of 1 μ m. The analysis was done using the following material parameters: (1) lattice diffusivity of $3.62 \times 10^{-18} m^2/s$, (2) a grain boundary diffusivity of $1.02 \times 10^{-11} m^2/s$, and (3) a grain boundary width of $5 \times 10^{-10} m$.

TABLE 24. The Predicted Creep Rate for Fine Grained
Pure Aluminum (38, 73)

<u>Deformation Mode</u>	<u>Creep Rate, s^{-1}</u>
Coble-grain boundary	0.458
Nabarro-Herring (lattice diffusion)	3.4×10^{-5}
Particle strengthened ($\sigma_{Orowan} < \sigma_{applied}$)	1.9×10^{-6}
Particle Strengthened ($\sigma_{Orowan} > \sigma_{applied}$)	9.4×10^{-2}

In a dispersion free aluminum alloy having a grain size of 0.5 μ m, Coble grain boundary deformation dominates. The presence of 1.0 μ m dispersoids curtails the rate of deformation by 2 to 5 orders of magnitude depending on whether the applied stress is less than or greater than the Orowan stress.

The creep rate of the PM Al-Ti alloys measured at the above stated conditions was approximately 10^{-9}s^{-1} . Clearly, grain boundary Coble creep has been suppressed by the presence of dispersoids. Arzt et. al. (94) have described this type of behavior as interface controlled diffusional creep. Dislocation motion within the grain boundary is impeded by particles in a manner analogous to Orowan strengthening within the grain interior. Dislocations must bow and/or climb past grain boundary dispersoids, however, this requires the local rearrangement of atoms within the grain boundary by an interface controlled diffusion mechanism. In summary, dispersoids inhibit both grain boundary and lattice deformation at elevated temperatures.

3. COMPARISON WITH CURRENT ALLOYS

a. Ambient Temperature Properties. The room temperature properties of several elevated temperature aluminum alloys are compared with PM aluminum-titanium in Table 25.

TABLE 25. Ambient Temperature Properties of Several Elevated
Temperature Alloys (12, 18, 97, 98, 99)

ALLOY	YS. MPa	%ELONG.	NTS TS	E. GPa	DEN.gcm ⁻³
AM6	321	9	1.25	87	2.8
83089*	326	10	--	--	2.8
Dispall 2**	248	10	--	70	2.7
Al-8Fe-2Mo	322	11	1.12	--	--
(FVS0812) -	390	10	$K_{1c} \approx 31\text{MPa}\sqrt{\text{m}}$	88.4	3.02
(FVS1212) - -	605	8.7	--	95.5	3.07
CU78 - - -	445	12	--	81.4	2.93
2219-T8	345	12	--	72.4	2.82

•	Al-4Ti-(2.11)0-0.47C
••	Al-2C-(0.4-2.5)0
+	Al-8.5Fe-1.3V-1.7Si
++	Al-12.4Fe 1.2V-2.3Si
+++	Al-8.3Fe-4Ce

Examination of the ambient temperature mechanical properties indicates that AM6 has the advantage of low density, high modulus, and good notched toughness. The strength of AM6 is superior to that of Dispall 2, comparable to Al-8Fe-2Mo, and 80 to 280MPa less than the higher strengths of Al-Fe-Ce and Al-Fe-V-Si alloys.

b. High Temperature Strength. The yield strength of several elevated temperature materials tested at temperature is presented in Figure 5.3. The strength of the aluminum-titanium alloys tested at 250°C are superior to those of conventional aluminum alloys, e.g., 7075-T6, and comparable to elevated temperature materials, e.g., Al-Fe-Ce and Al-Fe-Mo. However, the Al-Fe-V-Si alloys have the best reported strength over the entire temperature range reported.

c. Creep-Stress Rupture. The creep and stress rupture of several aluminum alloys are presented in Table 26. At an applied stress of 138 MPa and temperature between 200-300°C, AM6 is substantially more resistant to creep deformation than conventional aluminum alloys, e.g., 2024, 6061, and 7075. The nonrecoverable strain of AM6 after 100hrs. at 138MPa and 220°C is comparable to that of CU78. However, it is worth mentioning that because the creep of AM6 is logarithmic, its deformation rate is continuously decreasing.

TABLE 26. The Creep Behavior of Several Aluminum
Alloys at 138 MPa and 220°C (12, 18, 97)

<u>Alloy</u>	<u>Rupture/%Strain</u>	<u>Time, hrs.</u>
7075-T6	R	1.8
6061-T6	R	24
2024-T6	R	110
Al-8.3Fe-4Ce	R	>200
AM6, MA6, MA4	R	>200
Al-5.9Fe-6.0Ni	1.00	5
Al-7.4Fe-3.4Ce(232°C)	0.36	100
Al-8.3Fe-4Ce	0.05	100
AM6	0.12	100
AM6 (250°C)	0.17	100
MA6	0.16	100
MA6 (250°C)	0.34	100
AM4 (200°C)	0.35	100
AM4 (250°C)	0.87	100

The creep rate of Inco's mechanically alloyed Al-4Ti, 83089, at 171MPa and 232°C is $5.2 \times 10^{-8} \text{s}^{-1}$. (18) At an equivalent stress, alloy AM6 has a creep rate of $1.9 \times 10^{-8} \text{s}^{-1}$ at 250°C and $0.9 \times 10^{-8} \text{s}^{-1}$ at 220°C. This represents roughly a four fold improvement in creep rate. Furthermore, alloy 83089 has a rupture life of 38 hours at 232°C and 166MPa. Whereas the rupture life of AM6 is greater than 200 hours at 280°C and 172 MPa and provides a significant increase in specimen life at a higher stress and temperature.

4. FUTURE OF PM ALUMINUM TITANIUM

The atomized plus mechanically alloyed aluminum titanium alloys (AM) exhibit an excellent combination of strength, ductility, modulus, and creep resistance. However, it is clear that there are a number of competing elevated temperature commercial alloy systems which have very attractive properties. The commercial success of PM aluminum-titanium alloys lies in our ability to optimize its properties, reduce processing costs, and convince commercial producers/users of its potential. The research results indicate that PM aluminum-titanium alloys have the potential for large improvements in strength and creep resistance. In order to obtain these improvements, the aluminide size must be reduced and the distribution of carbide and oxide dispersoids improved. These can be achieved by quenching from higher temperatures to avoid primary Al_3Ti formation, melt spinning, and planar flow casting.

VI. CONCLUSIONS

1. ALLOY POWDER

- a Helium gas atomization of aluminum 4 and 6 wt.% titanium alloys results in a spherical powder particle having a two phase microstructure, i.e., Al_3Ti and Al. Al_3Ti forms both during peritectic solidification and precipitation from solid solution.
- b. A two phase lamella flake-like powder particle is produced by mechanically alloying elemental aluminum and titanium. Annealing at 1000°C in a vacuum produces Al_3Ti and Ti; and trace amounts of Al and $\text{Al}_{24}\text{Ti}_8$.
- c Mechanical alloying of the inert gas atomized powder increases the homogeneity of the Al_3Ti particle distribution. Carbon and oxygen are introduced into the powders during mechanical alloying and result in the formation of Al_4C_3 and Al_2O_3 .

- d. The carbon content of the powder alloys is proportional to the amount of stearic acid process control agent employed.
- e. Annealing the powders increases hardness by the precipitation of Al_3Ti . The pronounced increase in hardness of the mechanically alloyed powders is the result of Al_4C_3 and Al_2O_3 formation.

2. ALLOY MICROSTRUCTURE

- a. The microstructure of the as-received extruded helium gas atomized powder alloys contains three phases, i.e., Al, Al_3Ti , and Al_2O_3 .
- b. Four phases were identified in the extruded AM and MA microstructures, i.e., Al, Al_3Ti , Al_2O_3 , and Al_4C_3 .
- c. The aluminum distribution of the AT and AM alloys is finer and more homogeneous than that of the MA materials.
- d. Alloy grain size and texture is controlled by the fine particles in their microstructures.

3. AMBIENT TEMPERATURE MECHANICAL PROPERTIES

- a. The Orowan Strengthening model is not strictly applicable to these alloy systems because: 1) fine dispersoids are inhomogeneously distributed and 2) the mean planar spacing of Al_3Ti particles is comparable to the grain size.
- b. Alloy strength can be explained in terms of the Hall-Petch relationship.
- c. Elastic modulus increases with the amount of (111) fiber texture and volume fraction of Al_3Ti .
- d. Using the rule-of-mixtures, the modulus of Al_3Ti is estimated to be 178GPa.

- e. Mechanical alloying significantly improves alloy strength particularly at elevated temperatures.
- f. Annealing the aluminum-titanium alloys at 300°C for 100 hrs. increases strength. The increase in strength is attributable to the precipitation of Al_3Ti and the formation of Al_4C_3 and Al_2O_3 .
- g. Annealing at temperatures above 300°C reduces alloy strength and is attributable to Al_4C_3 and Al_2O_3 coarsening and grain growth.

4. ELEVATED TEMPERATURE TENSILE PROPERTIES

- a. The strength of the aluminum-titanium alloys decreases with temperature at a rate proportional to the decline in alloy shear modulus up to 200-250°C.
- b. The mechanically alloyed materials exhibit significantly better tensile strength with good levels of ductility at all test temperatures.

5. CREEP

- a. Logarithmic creep is observed in alloys AM6, MA4, and MA6 when tested at 138 MPa at temperatures between 220 and 280°C.
- b. Creep rate decreases as the volume fraction of Al_4C_3 and the amount of (111) fiber texture increases
- c. Creep rate decreases as alloy yield strength increases.

6. FRACTOGRAPHY

- a. Ambient and elevated temperature tensile tests result in ductile failures. Macroscopically, all fractures were cup and cone. Fractures initiate at the specimens' center and failure progression is by microvoid coalescence.

VII. RECOMMENDATIONS FOR FUTURE WORK

In order to advance our understanding of the structure-property-processing relationships of PM aluminum-titanium alloys, the following suggestions are made:

1. To improve alloy strength, faster solidification rate processing, e.g., melt spinning, is required to obtain Al_3Ti dispersoids small enough to participate fully in Orowan strengthening. Solidification rates may also be increased by reducing the temperature difference between the alloy's liquidus and solidus. This could be accomplished by the addition of small amounts of a eutectic forming element, e.g., Ce.
2. Extended coarsening studies are needed to assess long term alloy stability over a wide range of operational temperatures. This type of quantitative kinetic research should be performed on a binary alloy containing fine, homogeneously distributed, Al_3Ti particulates. Reductions to the coarsening kinetics may be affected by alloying additions focused on altering the particle-matrix interface.
3. Alloying modifications may be considered to alter the Al_3Ti body center tetragonal structure to a cubic structure with additions of Zr or Sc. The effect of a more coherent structure (e.g., λ/λ') combined with melt spinning and mechanical alloying can (may) provide for an improved alloy design and improved mechanical properties.
4. There exists a complex relationship between texture, dispersoids, and mechanical properties. This relationship is significantly large to warrant an immediate investigation into the role of dispersoid type, size and distribution on texture development. Particular attention should be focused on the mechanisms of texture development in a particle hardened alloy system.
5. Clarification of high temperature deformation response as a function of dispersoid size, texture and volume fraction of second phase.

NADC-87159-60

VIII. TABLES

TABLE 7. Composition of the Alloy Powders

<u>Material</u>	<u>Ti</u>	<u>Si</u>	<u>Fe</u>	<u>C</u>	<u>O</u>	<u>H (ppm)</u>
AT4	4.200	0.303	0.019	0.015	0.05	21.9
AT6	6.695	0.039	0.030	0.015	0.11	37.9
MA4	3.700	0.099	0.031	1.160	0.11	734.0
MA6	6.040	0.052	0.037	1.380	0.27	131.0
AM4	4.480	0.059	0.024	0.900	0.15	115.0
AM6	6.320	0.069	0.030	0.630	0.18	138.0
Master alloy	43.100	0.095	0.550			
Alcan Al		0.049	0.101			

TABLE 8. Phase Identification of As-Received Powder Alloys

<u>ALLOY</u>	<u>AL</u>	<u>TI</u>	<u>AL₃TI</u>	<u>AL₂₄TI₈</u>
AT4	VS	--	M	--
AT6	VS	--	M	--
AM4	VS	--	M	--
AM6	VS	--	M	--
MA4	VS	VW	--	--
MA6	VS	VW	--	--
MASTER ALLOY	S	S	--	--
ANNEALED MASTER ALLOY	VW	W	VS	W

-- NOT FOUND
 VW VERY WEAK
 W WEAK
 M MODERATE
 S STRONG
 VS VERY STRONG

TABLE 9. BET Analysis Results

<u>Material</u>	<u>SPECIFIC SURFACE AREA (m²/g)</u>	<u>POWDER DENSITY (g/cc)</u>
AT4	0.20	2.74
AT6	0.45	2.79
MA4	0.29	2.67
MA6	0.31	2.69
AM4	0.26	2.72
AM6	0.16	2.76

TABLE 10. Composition of the Powder Alloys

<u>Material</u>	<u>Ti</u>	<u>C</u>	<u>O</u>
AT4	4.04	0.01	0.12
AT6	5.89	0.01	0.16
MA4	4.70	1.25	0.37
MA6	5.60	1.72	0.60
AM4	5.60	0.62	0.58
AM6	6.32	1.01	0.19

NADC-87159-60

TABLE 11. Phase Identification of the Alloy Rod

<u>ALLOY</u>	<u>AL</u>	<u>AL₃Ti</u>	<u>AL₄C₃</u>	<u>AL₂O₃</u>
AT4	VS	S	--	VW
AT6	VS	S	--	VW
AM4	VS	S	M	VW
AM6	VS	S	S	VW
MA4	VS	S	S	VW
MA6	VS	S	S	VW

-- NOT FOUND
 VW VERY WEAK
 W WEAK
 M MODERATE
 S STRONG
 VS VERY STRONG

TABLE 12. Calculated Volume Percent of Second Phases Based on Compositional Stoichiometry

<u>ALLOY</u>	<u>Al₃Ti</u>	<u>Al₄C₃</u>	<u>Al₂O₃</u>	<u>TOTAL</u>
AT6	15.01	0.06	0.24	15.31
AT4	14.30	0.05	0.18	14.53
AM6	15.39	4.76	0.28	20.43
AM4	12.66	2.92	0.86	16.44
MA6	12.58	8.05	0.89	21.51
MA4	10.52	5.83	0.54	16.90

NADC-87159-60

TABLE 13. Particle Size(μm) as Measured by TEM of the Alloy Rod Annealed for 100hrs.

<u>ALLOY</u>	<u>25°C</u>	<u>300°C</u>	<u>400°C</u>
AT6	0.13	0.11	0.08
AT4	0.07	0.08	0.08
AM6	0.04	0.05	0.08
AM4	0.08	0.08	0.13
MA6	0.05	0.09	----
MA4	0.05	0.16	0.10

TABLE 14. Grain Size(μm) of the Alloy Rod Annealed for 100hrs.

<u>ALLOY</u>	<u>25°C</u>	<u>300°C</u>	<u>400°C</u>
AT6	0.74	0.35	1.01
AT4	0.47	0.48	0.97
AM6	0.29	0.35	0.37
AM4	0.31	0.50	0.50
MA6	0.32	0.36	----
MA4	0.28	----	0.38

NADC-87159-60

TABLE 15. Texture of the Extruded Alloy Rod: Random Intensity Times Peak Intensity for the (111) and (200) Planes.

<u>ALLOY</u>	<u>(111)</u>	<u>(200)</u>
AT6	22.2	3.7
AT4	15.8	2.8
AM6	4.2	1.9
AM4	10.3	2.3
MA6	2.8	1.6
MA4	5.2	1.7

TABLE 16. Ambient Temperature Tensile Properties

<u>ALLOY</u>	<u>TENSILE STRENGTH (MPa)</u>	<u>YIELD STRENGTH (MPa)</u>	<u>PERCENT ELONGATION</u>	<u>PERCENT REDUCTION IN AREA</u>	<u>YOUNG'S MODULUS (GPa)</u>	<u>NT UTS</u>
AM6	351.3	320.9	9.0	12.5	86.7	1.2
STD:	9.0	6.0	1.4	0.2	0.1	
AM4	320.9	287.7	15.0	29.8	85.7	1.5
STD:	9.6	9.6	0.0	1.7	0.1	
MA6	347.1	325.1	8.0	20.6	80.3	1.4
STD:	4.1	3.7	1.0	1.6	1.0	
MA4	338.1	318.3	9.3	27.1	73.9	1.4
STD:	5.2	5.7	0.5	0.8	2.1	
AT6	220.4	180.4	21.0	33.4	88.2	1.5
STD:	0.7	6.7	1.0	1.2	0.2	
AT4	229.6	177.8	22.0	41.1	91.1	1.5
STD:	4.4	7.2	0.8	0.7	0.2	

TABLE 17. Tensile Properties of the Annealed Rod

ANNEAL TEMP. (°C)	ALLOY	TENSILE STRENGTH (MPa)	YIELD STRENGTH (MPa)	PERCENT ELONGATION	PERCENT REDUCTION IN AREA
25	AM6	351.29	320.86	9.00	12.47
	AM4	320.92	287.66	15.00	29.77
	MA6	347.14	325.15	8.00	20.55
	MA4	338.07	318.30	9.33	27.07
	AT6	220.41	180.41	21.00	33.35
	AT4	229.56	177.82	22.00	41.10
200	AM6	352.45	329.52	9.00	16.87
	AM4	318.03	293.03	13.50	26.50
	MA6	361.83	345.03	6.50	15.75
	MA4	340.28	324.76	8.00	25.90
	AT6	228.69	178.93	16.00	21.35
	AT4	225.79	211.69	2.00	5.75
300	AM6	371.38	347.03	8.50	14.35
	AM4	340.28	315.76	15.00	26.70
	MA6	370.14	352.52	7.00	19.40
	MA4	361.24	349.48	7.50	17.45
	AT6	250.55	190.93	11.50	16.45
	AT4	212.00	183.00	23.00	40.70
400	AM6	349.07	327.55	8.50	15.05
	AM4	330.14	303.17	13.00	23.50
	MA6	361.24	342.31	5.00	12.50
	MA4	338.24	324.69	8.00	19.75
	AT6	219.79	170.79	14.50	21.15
	AT4	215.38	158.21	21.00	38.80
500	AM6	349.03	312.21	7.00	10.25
	AM4	317.97	312.21	7.00	10.25
	MA6	307.83	289.28	2.00	2.30
	MA4	301.86	281.45	4.00	5.30
	AT6	201.10	151.34	16.00	30.95
	AT4	198.07	134.28	24.00	46.50

TABLE 18. Elevated Temperature Tensile Properties

TENSILE TEMP. (°C)	ALLOY	TENSILE STRENGTH (MPa)	YIELD STRENGTH (MPa)	PERCENT ELONGATION	PERCENT REDUCTION IN AREA
25	AM4	287.66	320.92	12.67	29.77
	AM6	320.86	345.72	9.50	12.55
	MA4	318.30	338.07	9.33	27.07
	MA6	325.15	347.14	8.00	20.55
	AT4	177.82	229.56	22.00	41.10
	AT6	180.41	220.41	21.00	33.35
200	AM4	197.28	203.31	10.50	22.10
	AM6	245.76	254.55	5.00	11.05
	MA4	245.76	255.24	2.50	5.00
	MA6	262.66	273.59	4.50	8.45
	AT4	126.76	134.21	26.50	51.65
	AT6	127.62	136.38	14.00	24.40
300	AM4	149.21	154.62	9.50	28.90
	AM6	195.79	200.55	4.00	5.80
	MA4	197.17	201.21	2.50	12.50
	MA6	198.62	202.69	4.50	9.95
	AT4	76.90	82.34	21.50	57.55
	AT6	95.59	99.97	15.00	28.25
400	AM4	91.52	91.52	6.00	27.30
	AM6	97.68	98.14	2.67	5.63
	MA4	77.00	78.34	1.50	1.20
	MA6	83.03	83.72	2.00	4.65
	AT4	20.28	21.59	24.50	80.00
	AT6	24.86	26.24	10.50	22.10

TABLE 19. Shear Modulus/Normalized Shear Modulus Versus Temperature

ALLOY	TEMPERATURE, °C					
	25	100	200	300	350	400
AT4	50.0	49.0	45.3	39.8	37.0	33.5
	100	98	91	80	74	67
AT6	50.0	48.8	45.0	40.2	38.2	35.5
	100	98	90	80	76	71
AM4	45.0	44.0	40.2	34.8	32.5	30.0
	100	98	89	77	72	67
AM6	49.9	49	45.8	41.0	39.5	34.0
	100	98	92	82	79	68
MA4	52.0	51.5	48.8	44.3	40.5	37.0
	100	99	94	85	78	71
MA6	54.3	53.5	50.2	45.0	41.5	40.5
	100	98	92	83	76	75

TABLE 20. Creep Rate of PM Aluminum-Titanium Alloys Measured Between 50 and 150 Hours

Alloy	Temp. °C	T/T _m	⁴ Stress (MPa)	Creep Rate (s ⁻¹ × 10 ⁹)	Constant (× 10 ³)
AM4	220	0.53	104	0.7	2.76
	250	0.56	" "	9.9	2.86
	300	0.61	" "	18.0	4.35
AM4	200	0.51	138	9.7	4.70
	250	0.56	" "	53.2	8.03
AM6	220	0.53	" "	4.2	2.60
	250	0.56	" "	4.6	3.13
	280	0.59	" "	8.7	3.36
MA4	250	0.56	" "	6.5	3.73
	280	0.59	" "	9.9	4.59
MA6	220	0.53	" "	4.6	2.95
	250	0.56	" "	10.3	4.69
	280	0.59	" "	17.3	5.64
AM6	220	0.53	172	9.2	3.69
	250	0.56	" "	18.7	5.33
	280	0.59	" "	63.4	6.43

TABLE 21. Orowan Strength: Calculated from the Al_3Ti Particle Size

<u>Alloy</u>	<u>Vol.% Al_3Ti</u>	<u>Diameter (μm)</u>	<u>L^*</u>	<u>L^{**}</u>	<u>CRSS¹</u>	<u>CRSS²</u>
AT6	11.5	0.63	1.68	1.17	39.4	39.7
	3.5	0.13	0.62	0.51	46.6	86.1
AM6	11.9	0.66	1.73	1.19	39.6	39.4
	3.5	0.04	0.17	0.14	123.0	95.0
MA6	9.1	0.90	2.70	1.96	22.1	31.7
	3.5	0.05	0.23	0.19	98.1	107.8

L^* = Center to center distance(μm) between particles.

L^{**} = Edge to edge distance(μm) between particles.

CRSS¹ = Critical resolved shear stress(MPa) calculated using L^{**} and the mean particle diameter.

CRSS² = Critical resolved shear stress(MPa) calculated using L^{**} and the distribution of particle sizes.

TABLE 22. Orowan Strength: Calculations Based on the Presence of Al_4C_3

<u>Alloy</u>	<u>Vol.% Al_4C_3</u>	<u>Mean Diameter(μm)</u>	<u>$L^*(\mu\text{m})$</u>	<u>CRSS(MPa)</u>
AT6	0.06	0.01	0.37	23.9
AT4	0.05	0.01	0.40	21.8
AM6	4.76	0.01	0.04	259.3
AM4	2.92	0.01	0.05	192.6
MA6	8.05	0.01	0.03	364.0
MA4	5.83	0.01	0.04	294.6

L^* = Center to center distance between particles

CRSS = Critical resolved shear stress

NADC-87159-60

IX. FIGURES

METAL POWDER REPORT 38, NO. 10, 1983

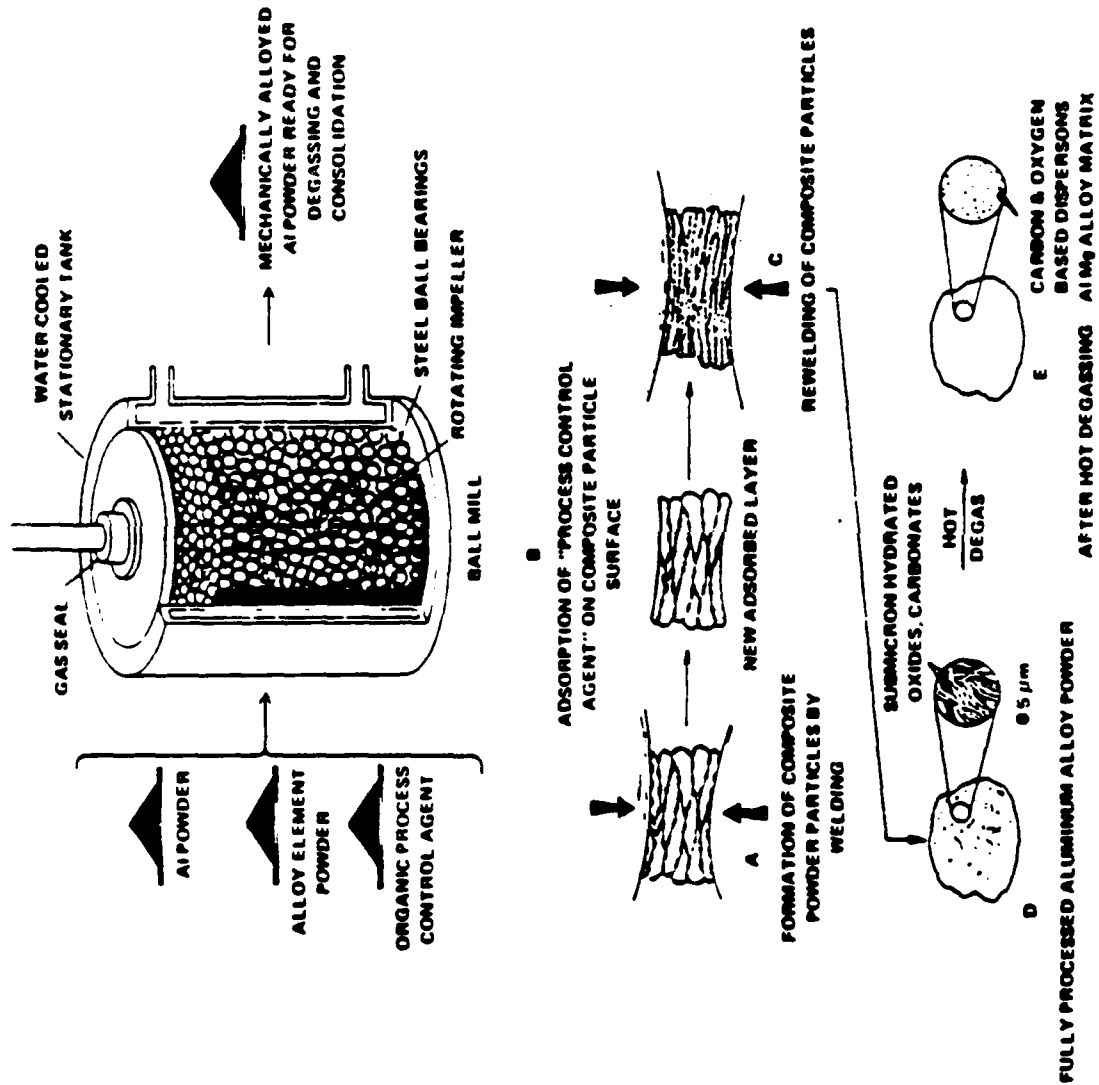


FIGURE 1.1 SCHEMATIC DIAGRAM OF THE MECHANICAL ALLOYING PROCESS

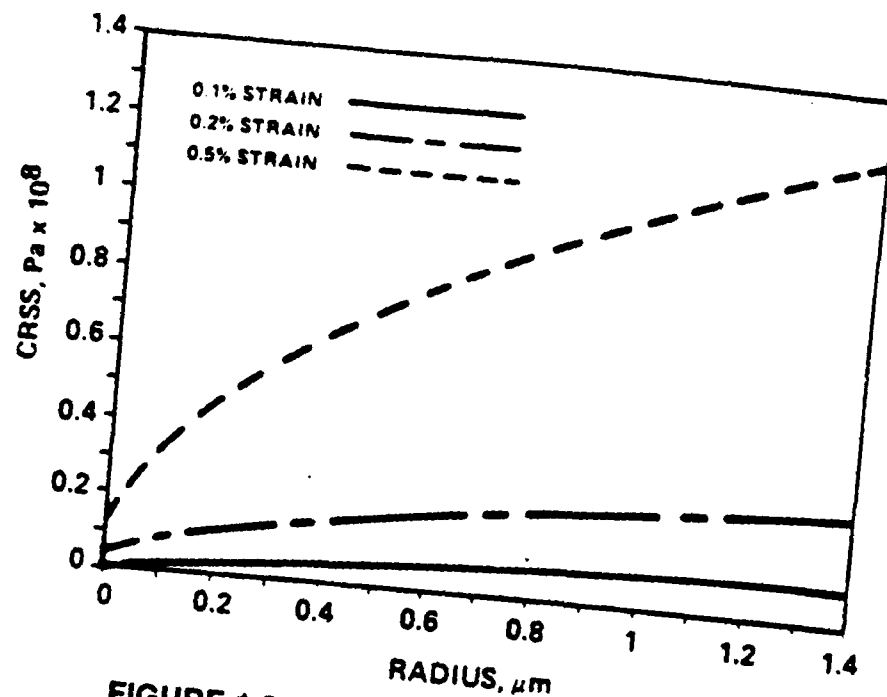


FIGURE 1.2 COHERENCY STRENGTHENING:
SHEAR STRENGTH VERSUS PARTICLE RADIUS

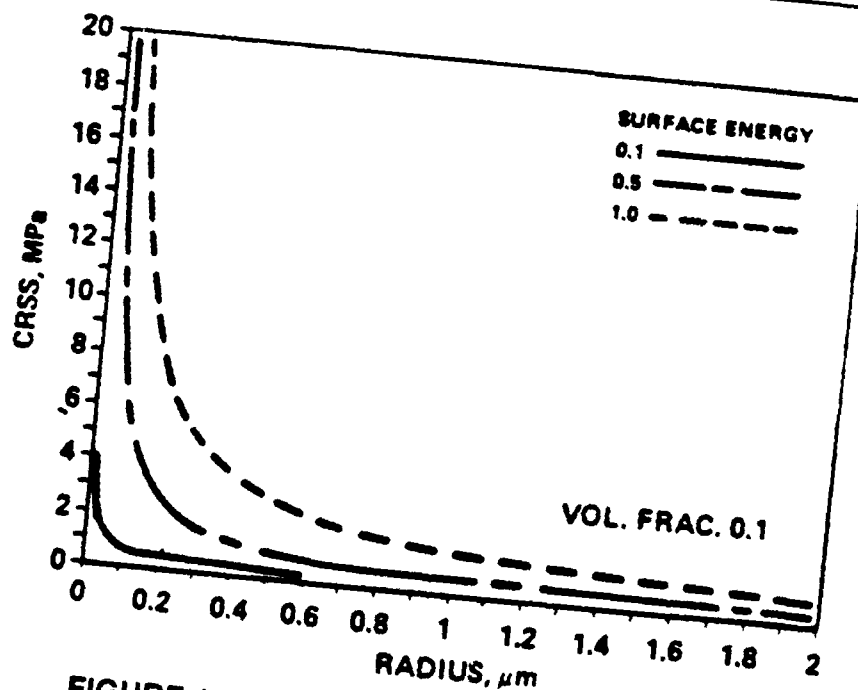
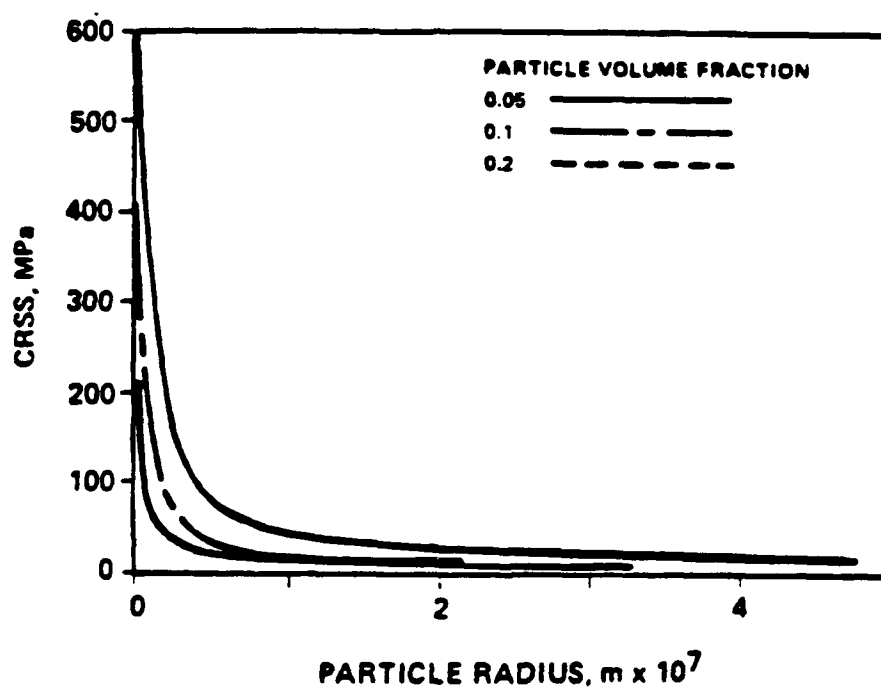
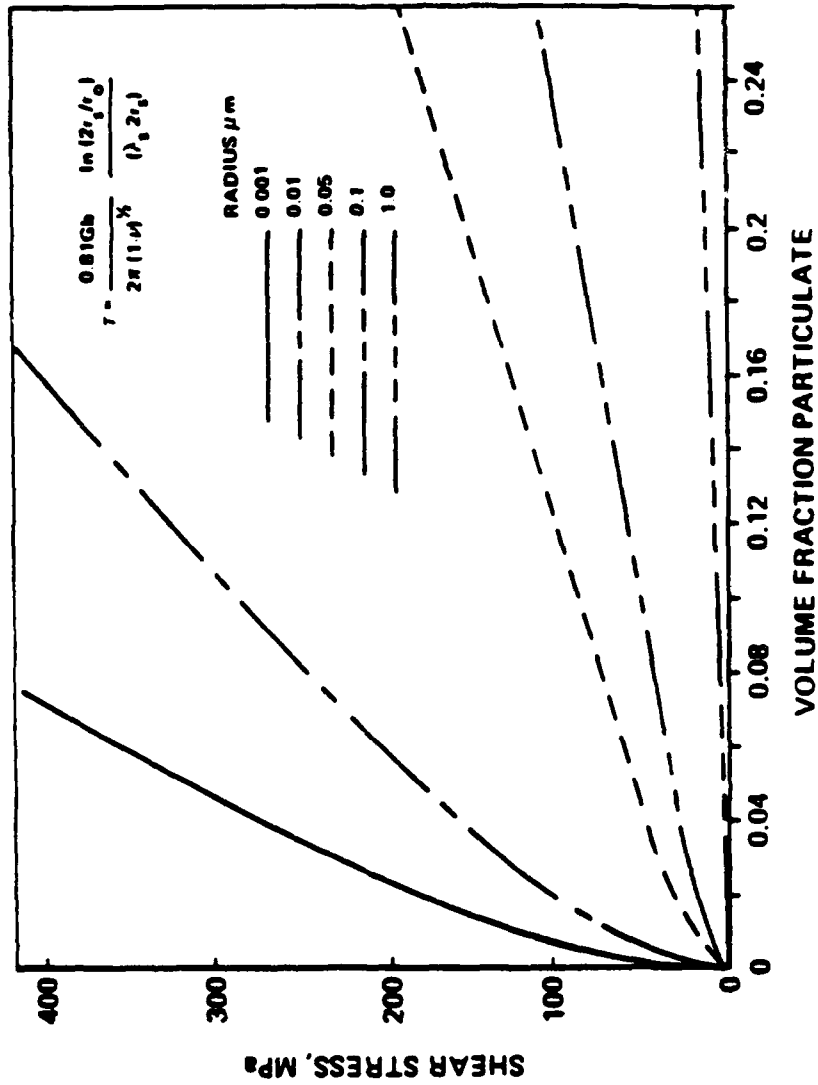


FIGURE 1.3 CHEMICAL STRENGTHENING:
SHEAR STRENGTH VERSUS PARTICLE RADIUS



**FIGURE 1.4 MODULUS STRENGTHENING:
SHEAR STRENGTH VERSUS PARTICLE RADIUS**



**FIGURE 1.5 OROWAN PARTICLE STRENGTHENING:
THE EFFECT OF PARTICLE SIZE**

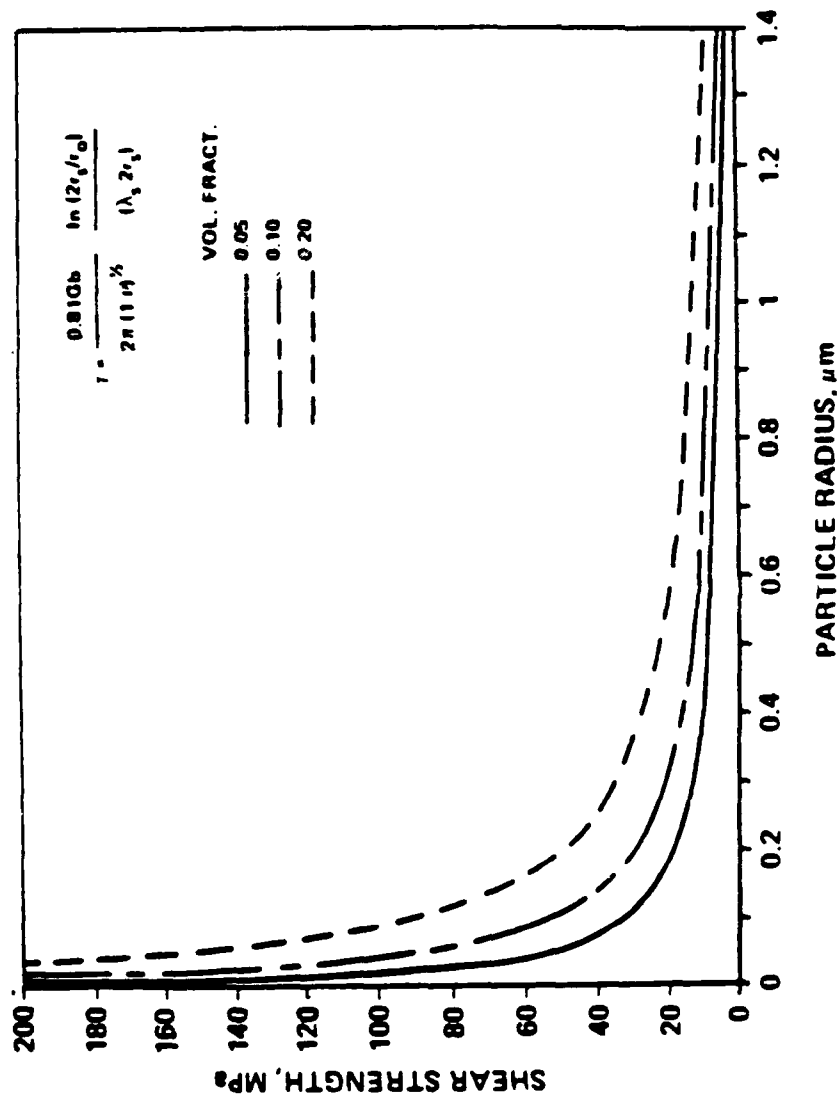
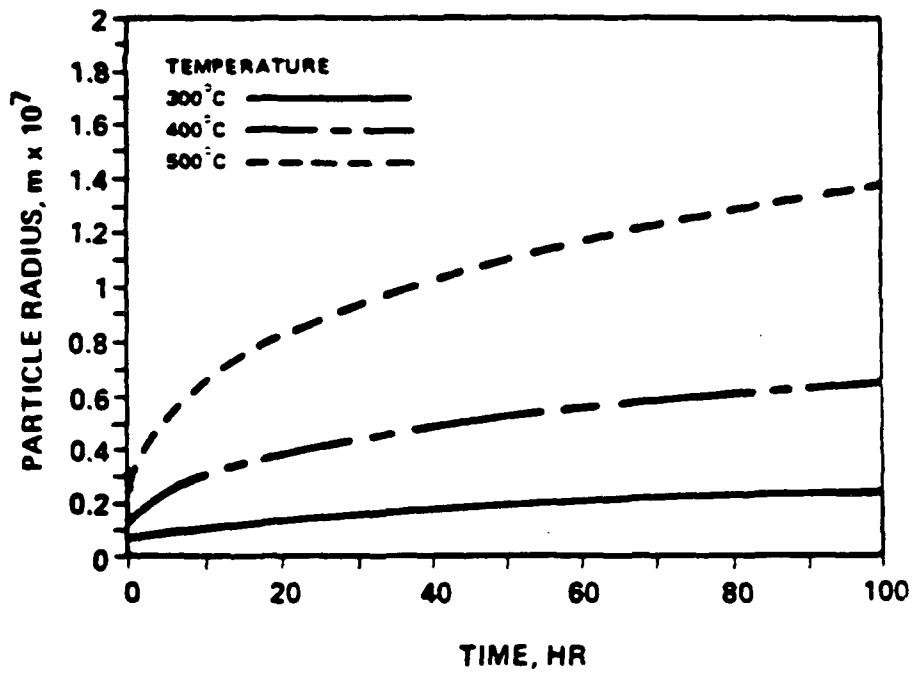


FIGURE 1.6 OROWAN PARTICLE STRENGTHENING:
THE EFFECT OF PARTICLE VOLUME FRACTION



**FIGURE 1.7 DIFFUSION CONTROLLED COARSENING
OF Al_3Ti PARTICULATES**

532-GA-87-00382

FRAZIER-TRIAD-3/20/87

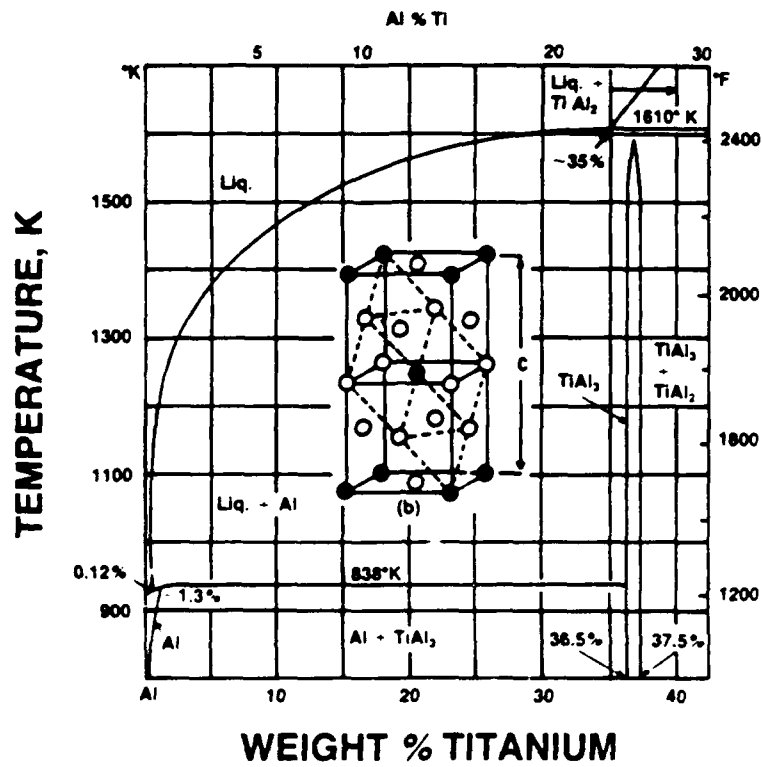


**FIGURE 1.8 ALUMINUM-TITANIUM PHASE
DIAGRAM AND THE Al_3Ti CRYSTAL STRUCTURE**

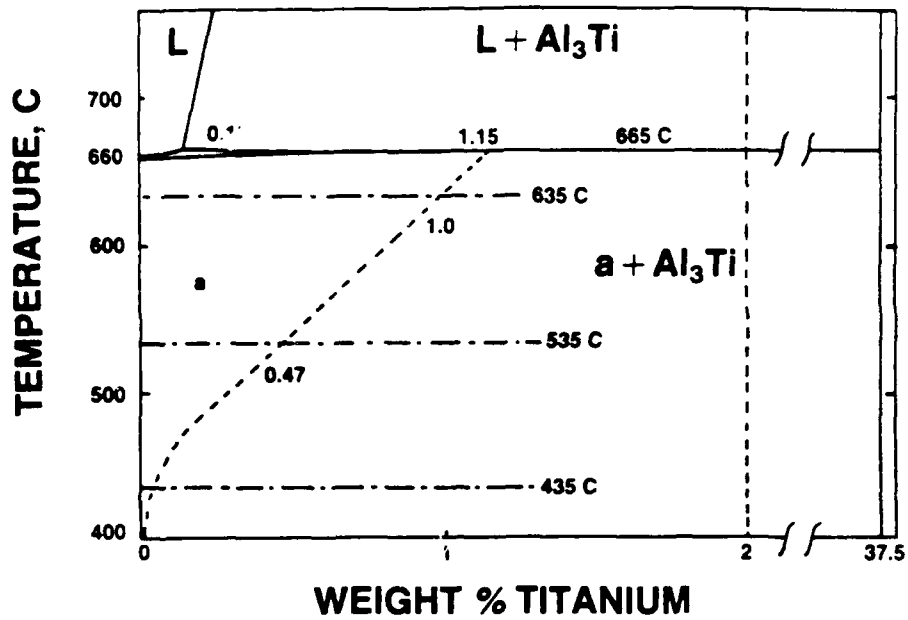


FIGURE 1.9 ALUMINUM RICH PORTION OF THE ALUMINUM-TITANIUM PHASE DIAGRAM

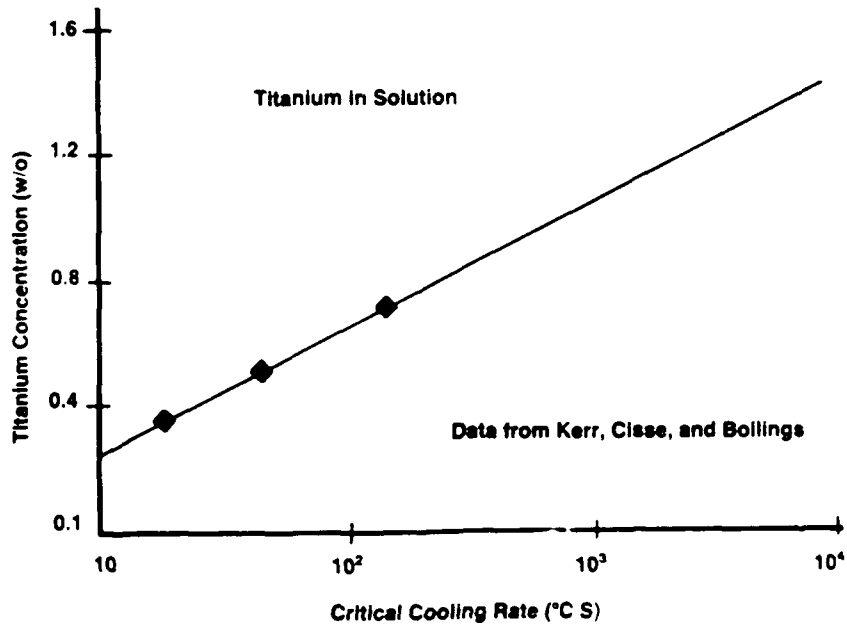


FIGURE 1.10 TITANIUM IN SOLID SOLUTION VERSUS COOLING RATE

PM ALUMINUM TITANIUM ALLOY PRODUCTION

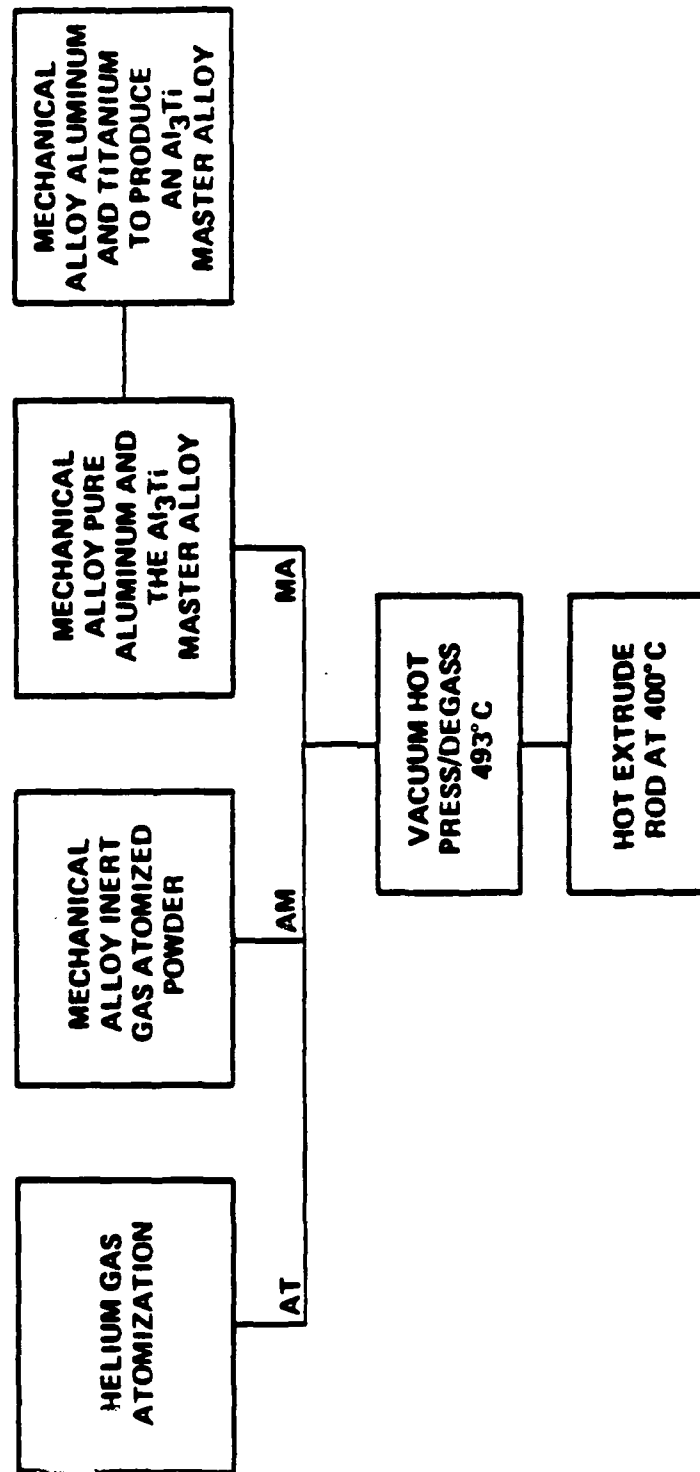
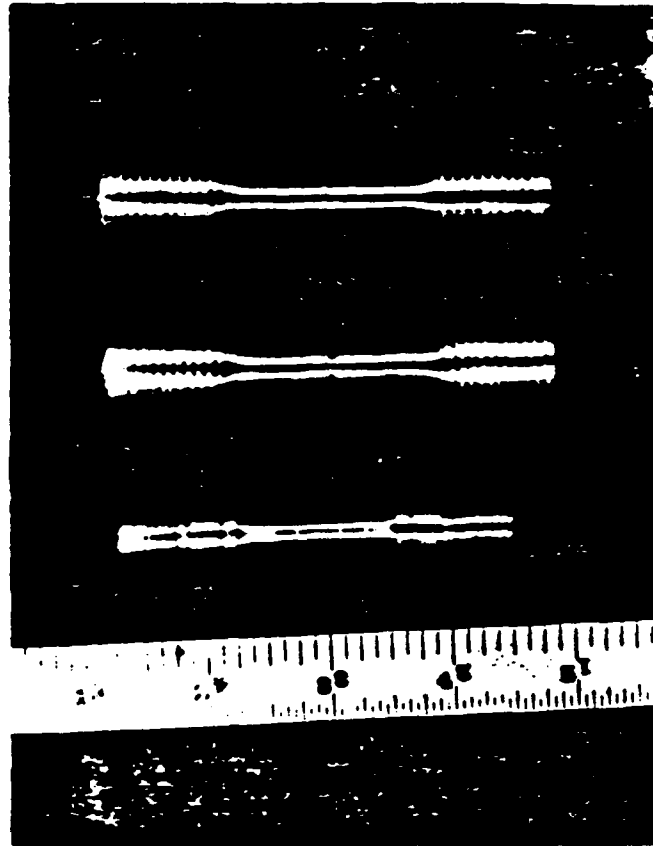


FIGURE 2.1 MATERIALS PROCESSING SCHEME



**FIGURE 2.2 MECHANICAL PROPERTY TEST SPECIMENS:
TENSILE, NOTCH TENSILE, AND CREEP**

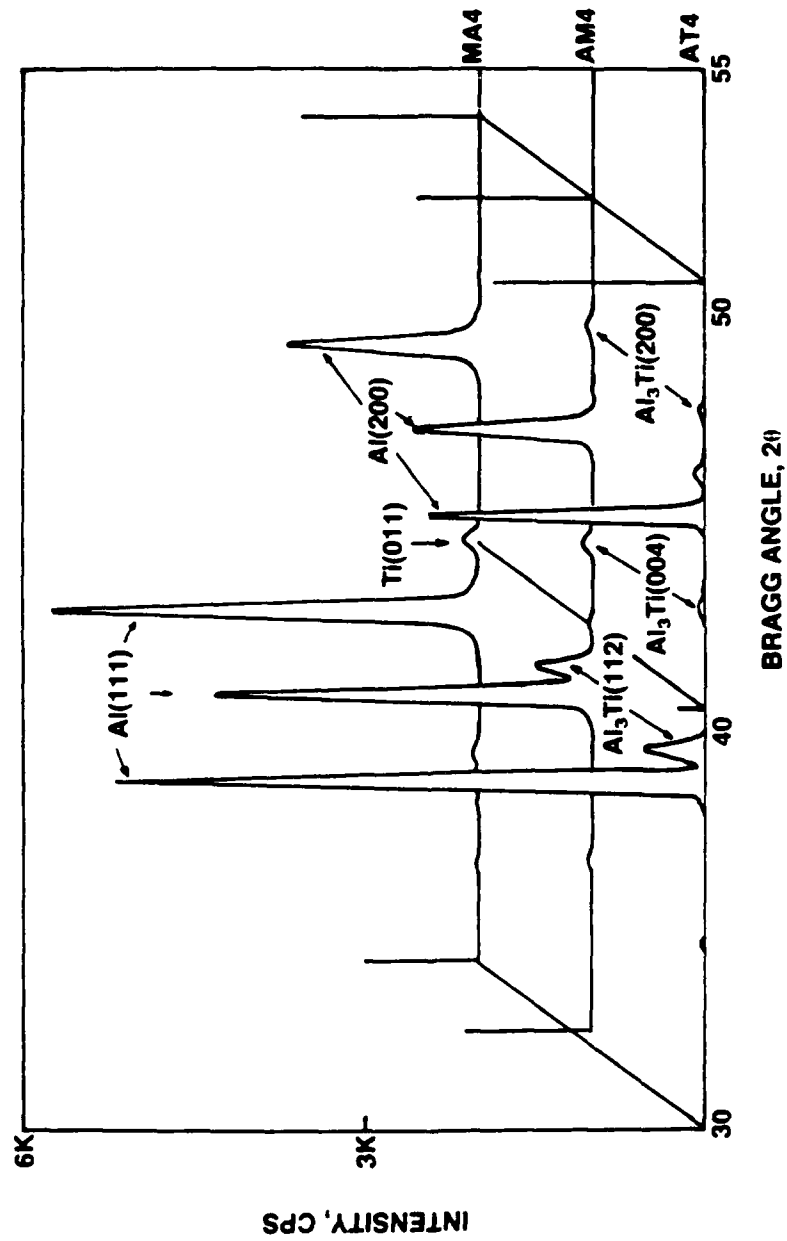


FIGURE 3.1 X-RAY DIFFRACTION PROFILES OF THE AT4, AM4, AND MA4 ALLOY POWDERS

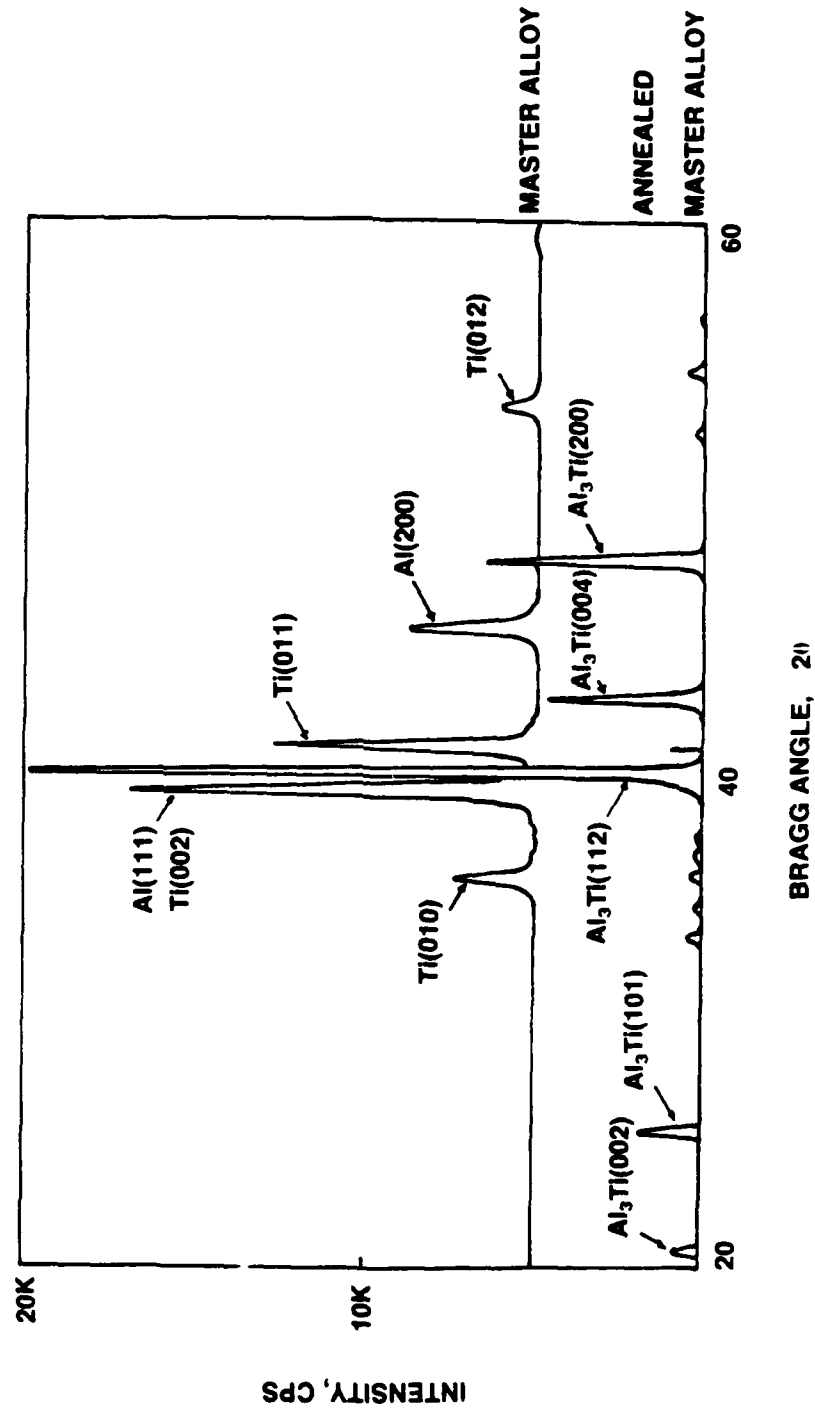
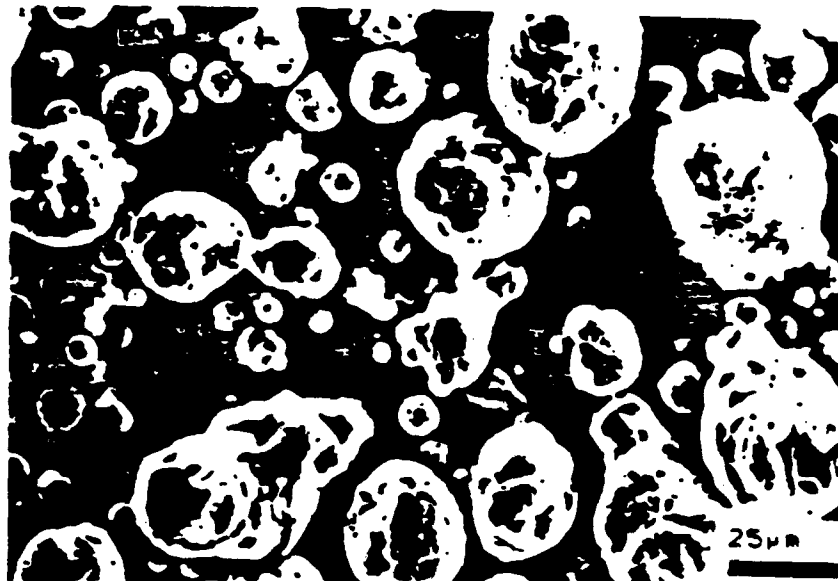


FIGURE 3.2 X-RAY DIFFRACTION PROFILES OF THE AS-RECEIVED AND ANNEALED MASTER ALLOY POWDER



**FIGURE 3.3 MORPHOLOGY OF THE HELIUM GAS
ATOMIZED POWDERS: a) AT4 AND b) AT6**

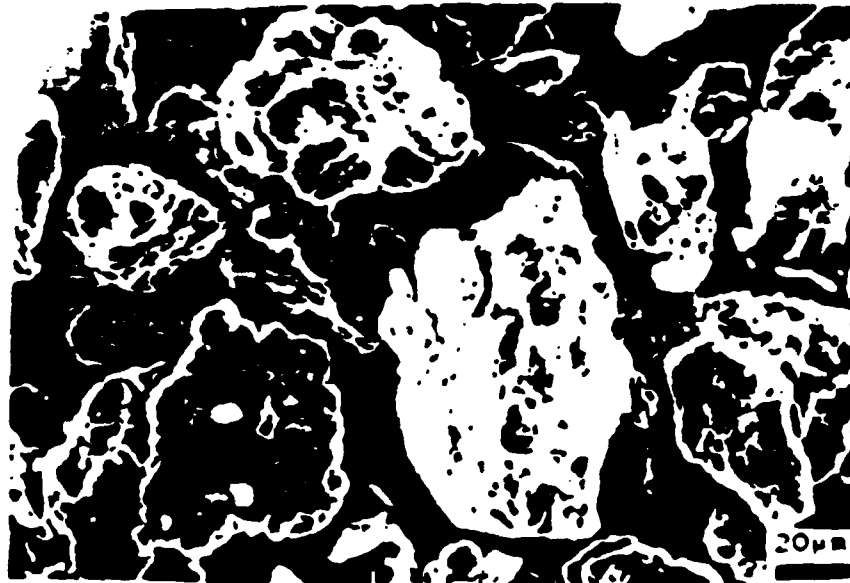
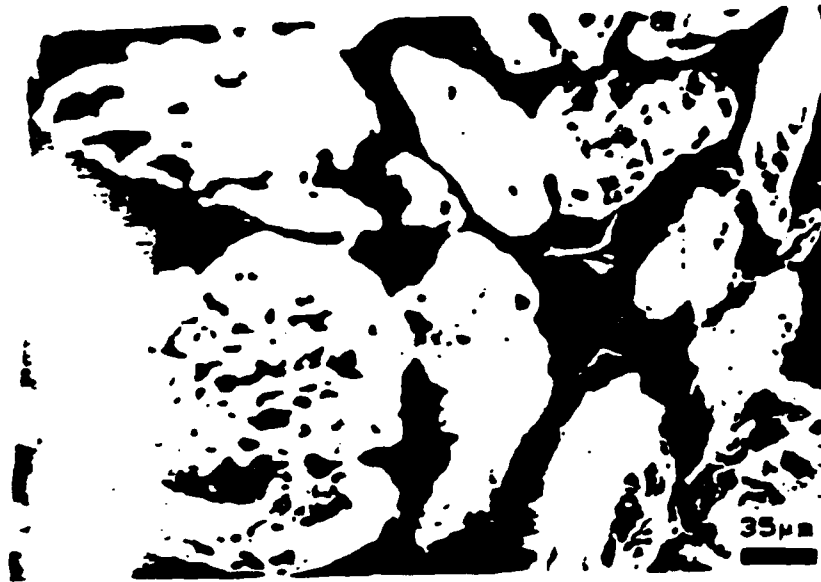


FIGURE 3.4 MORPHOLOGY OF THE ATOMIZED AND MECHANICALLY ALLOYED POWDERS: a) AM4 AND b) AM6

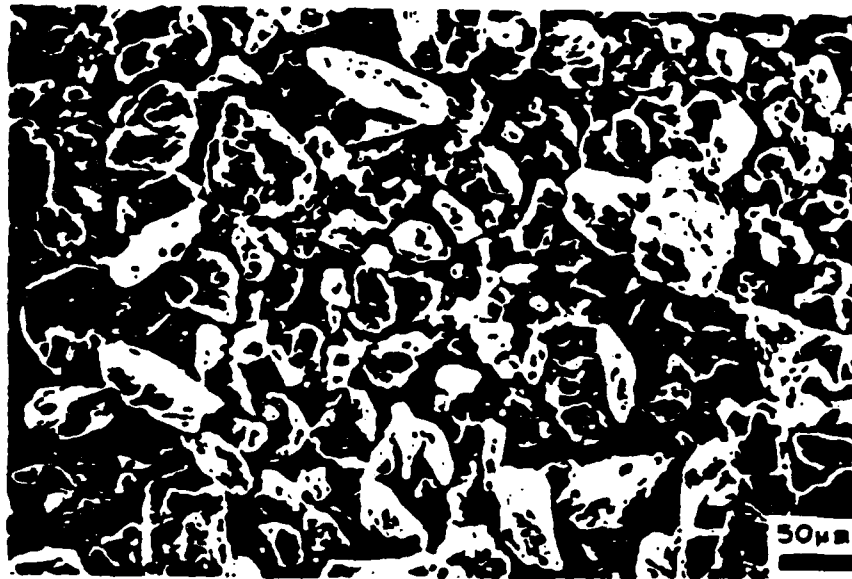
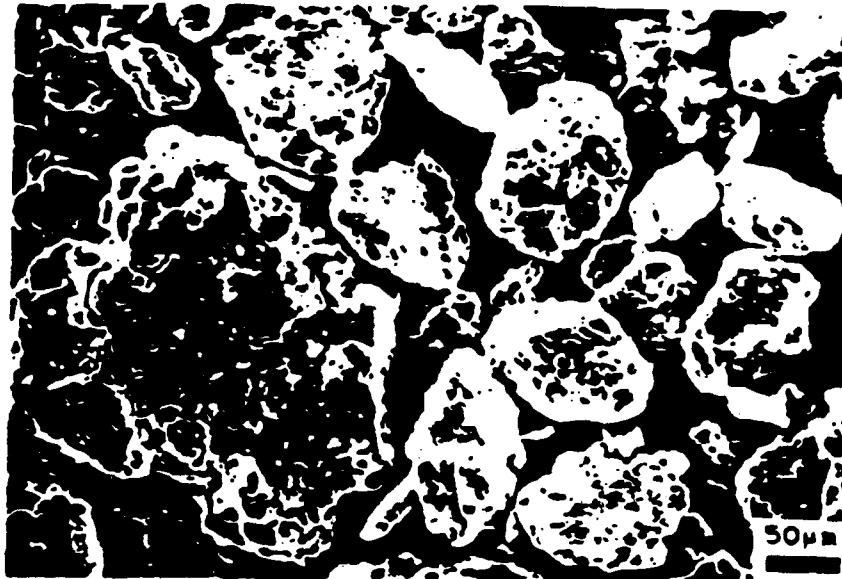
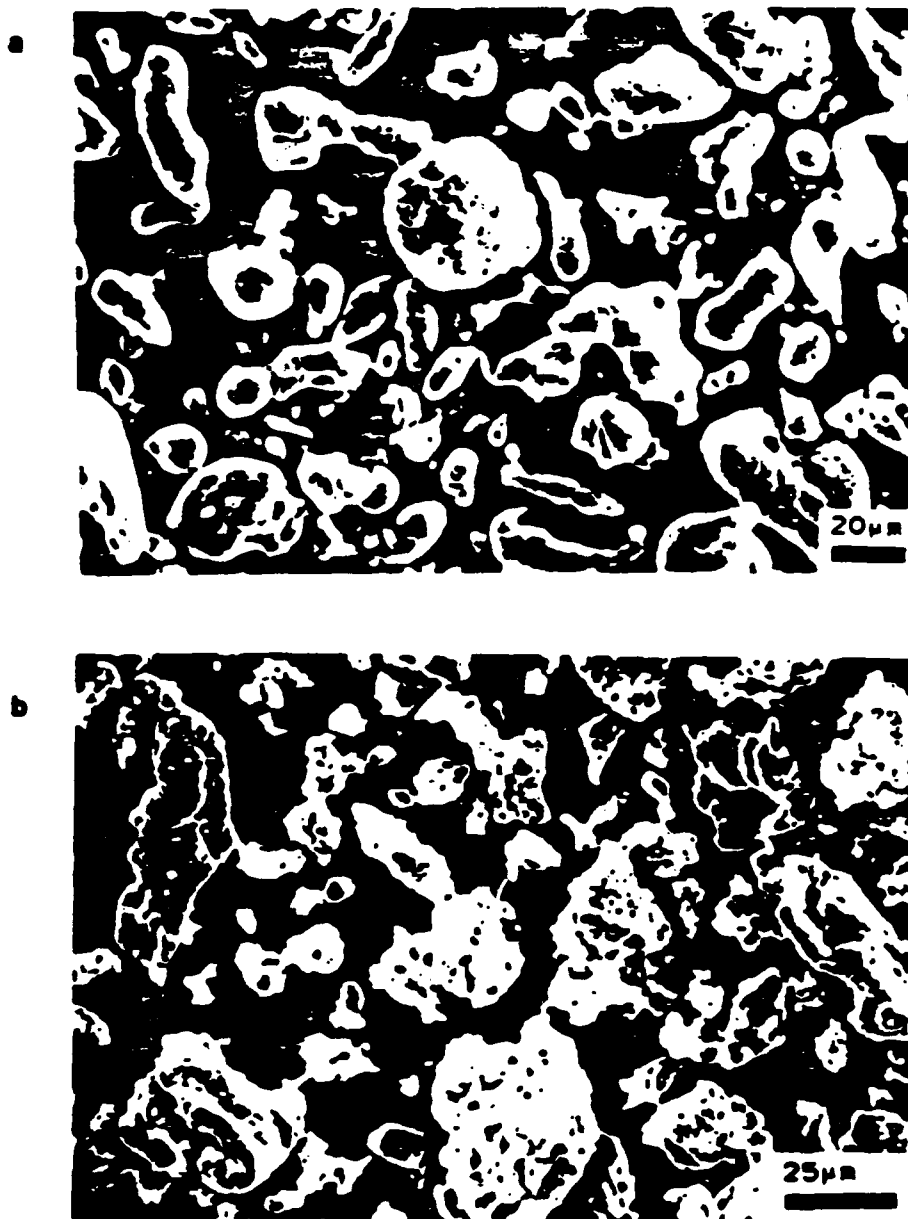
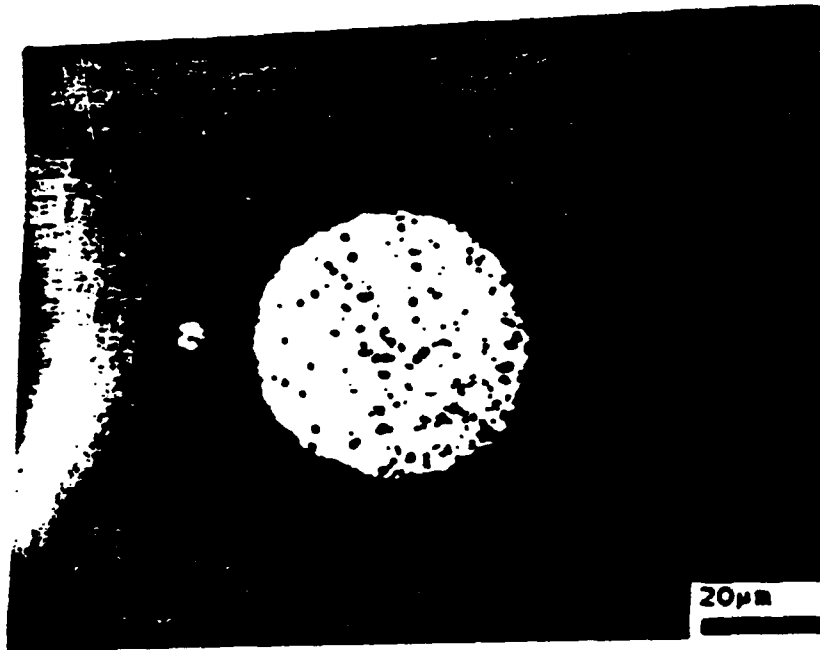


FIGURE 3.5 MORPHOLOGY OF THE MECHANICALLY ALLOYED POWDERS: a) MA4 AND b) MA6



**FIGURE 3.6 MORPHOLOGY OF a) ALCAN ALUMINUM AND
b) THE MASTER ALLOY USED TO PRODUCE MA4 AND MA6**



**FIGURE 3.7 OPTICAL MICROGRAPHS OF THE HELIUM
GAS ATOMIZED POWDERS: a) AT4 AND b) AT6**

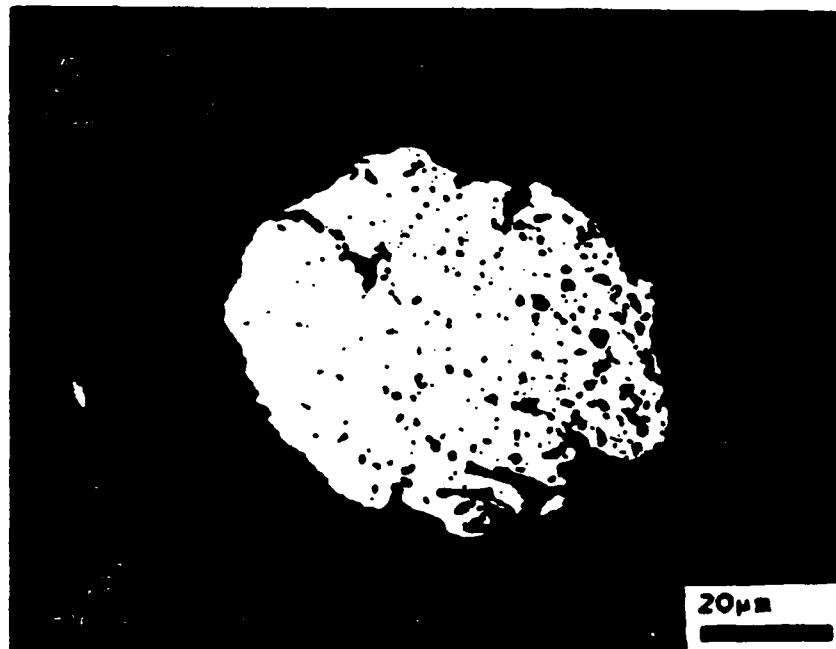
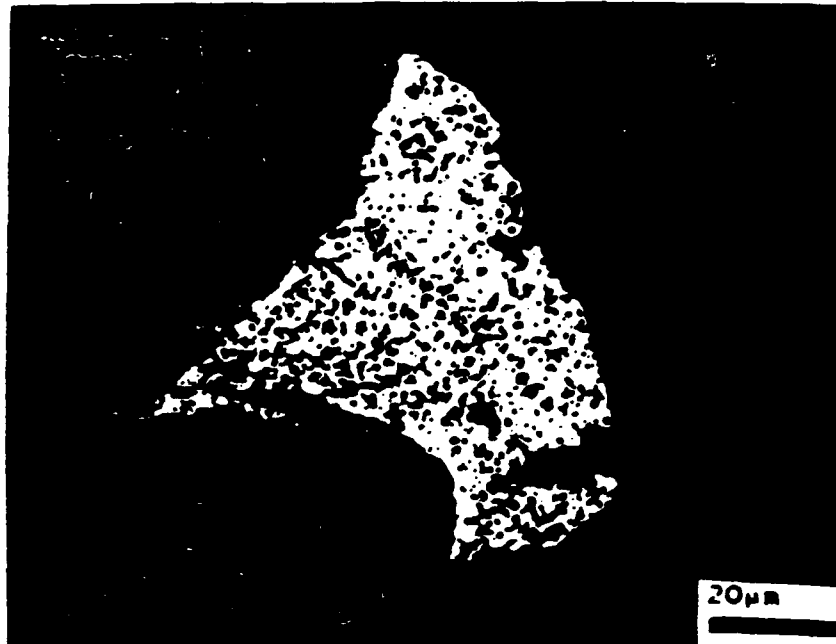


**FIGURE 3.8 OPTICAL MICROGRAPHS OF THE
ATOMIZED AND MECHANICALLY ALLOYED POWDERS:
a) AM4 AND b) AM6**

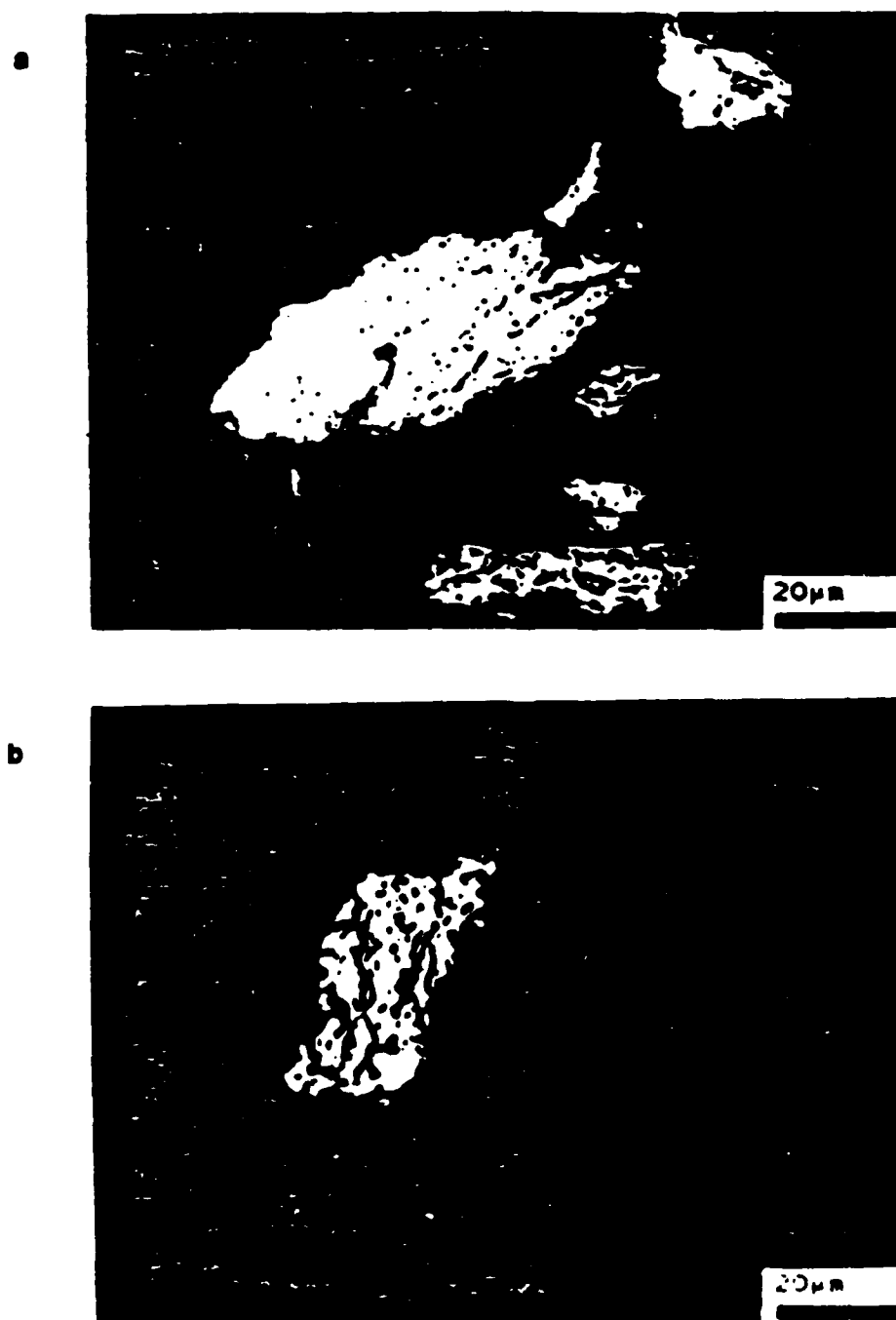


**FIGURE 3.9 OPTICAL MICROGRAPHS OF THE
ALUMINUM-TITANIUM MASTER ALLOY: a) AS-RECEIVED
AND b) ANNEALED FOR 24 HRS AT 1000 C IN A VACUUM**

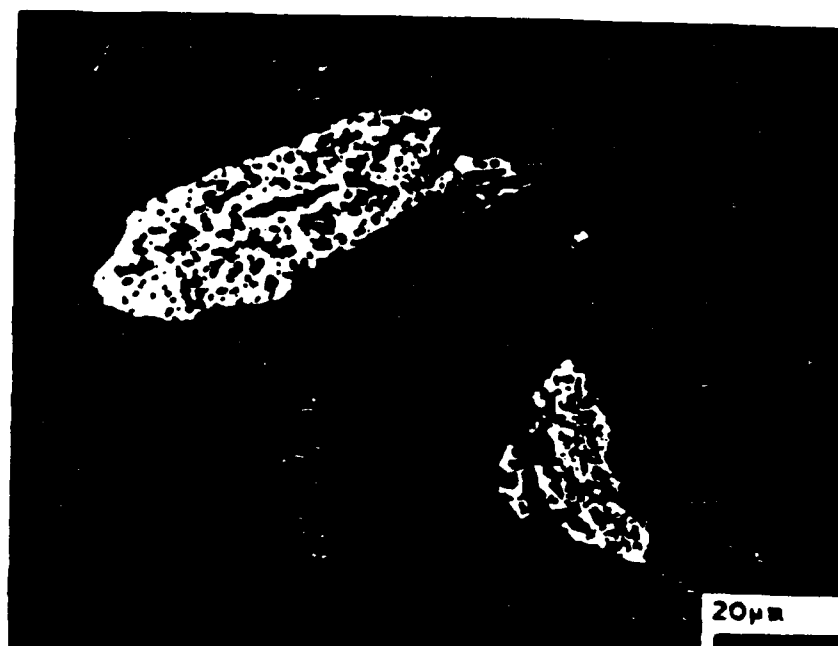


FIGURE 3.10 OPTICAL MICROGRAPHS OF MECHANICALLY ALLOYED POWDERS: a) MA4 AND b) MA6

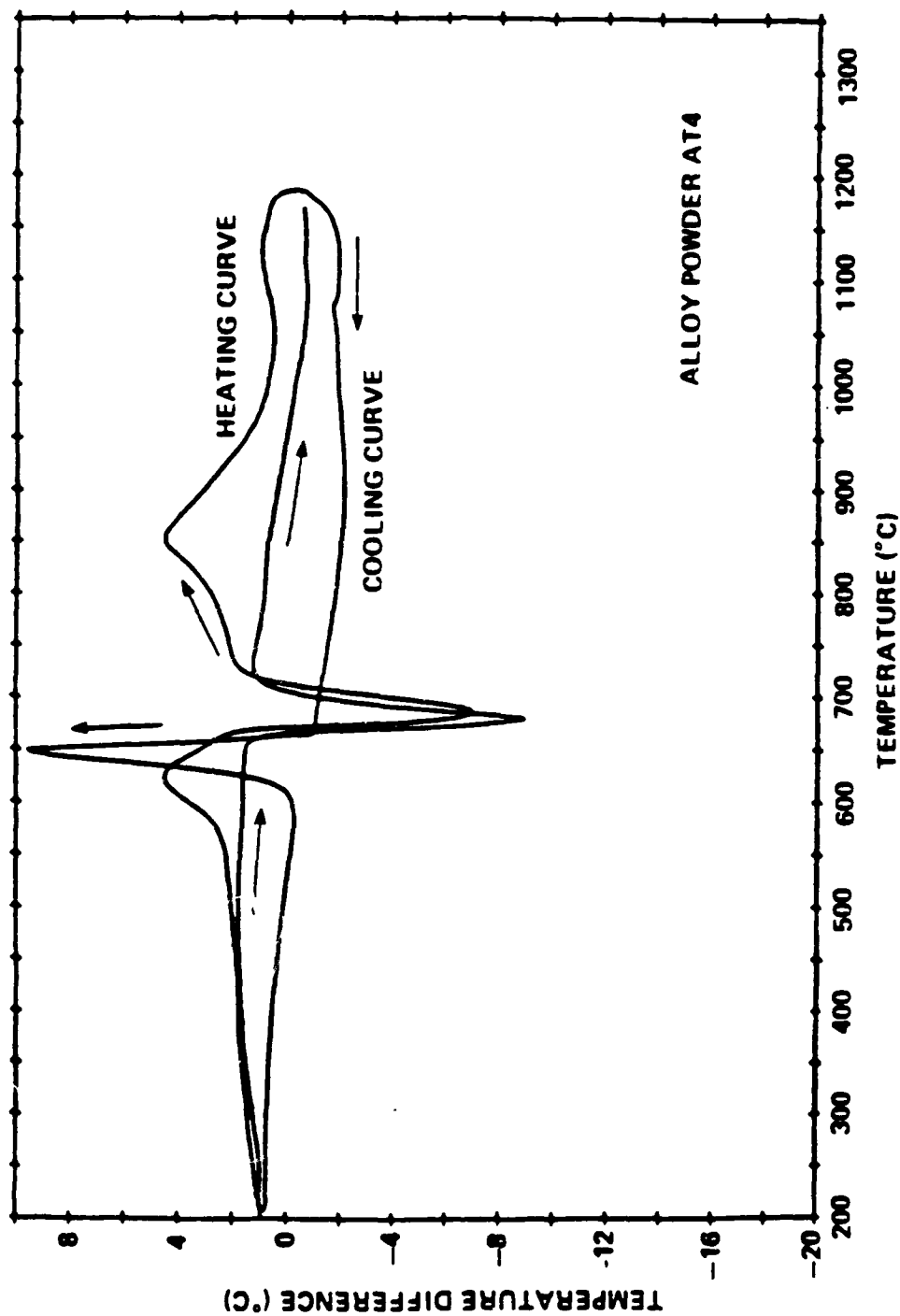


FIGURE 3.11 DIFFERENTIAL THERMAL ANALYSIS PROFILE OF ALLOY POWDER AT4

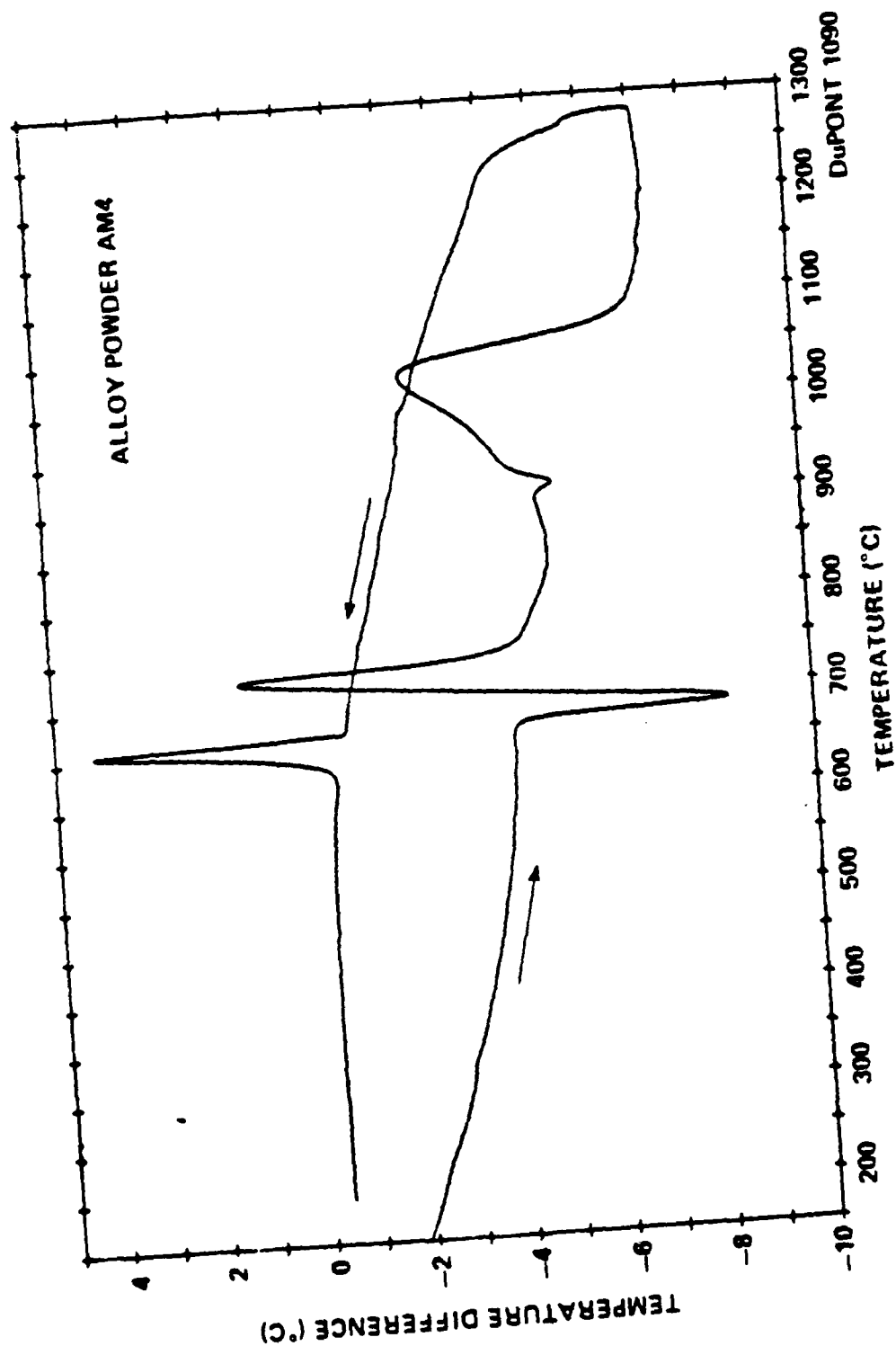


FIGURE 3.12 DIFFERENTIAL THERMAL ANALYSIS PROFILE OF ALLOY POWDER AM4

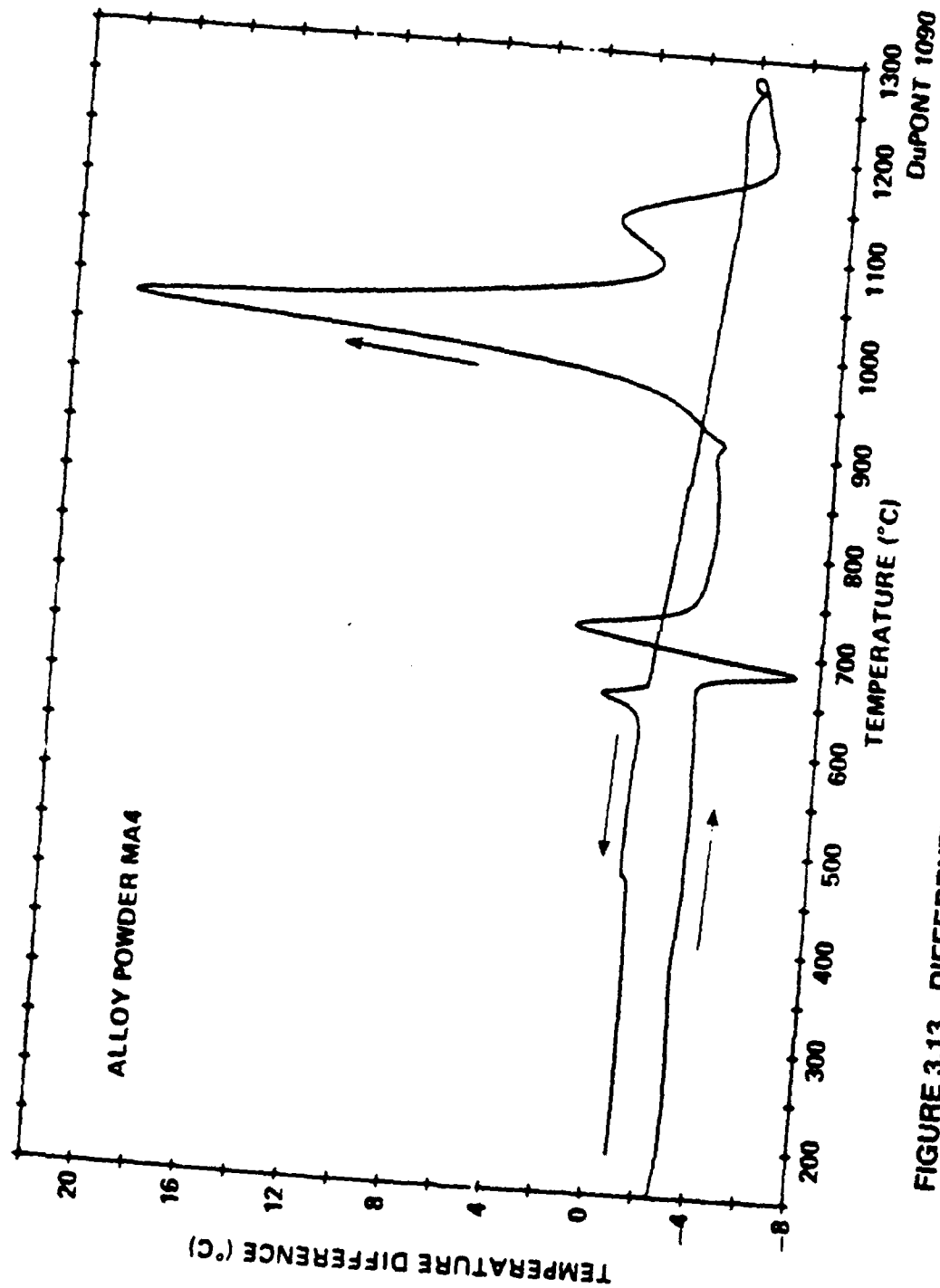


FIGURE 3.13 DIFFERENTIAL THERMAL ANALYSIS PROFILE OF ALLOY POWDER MA4

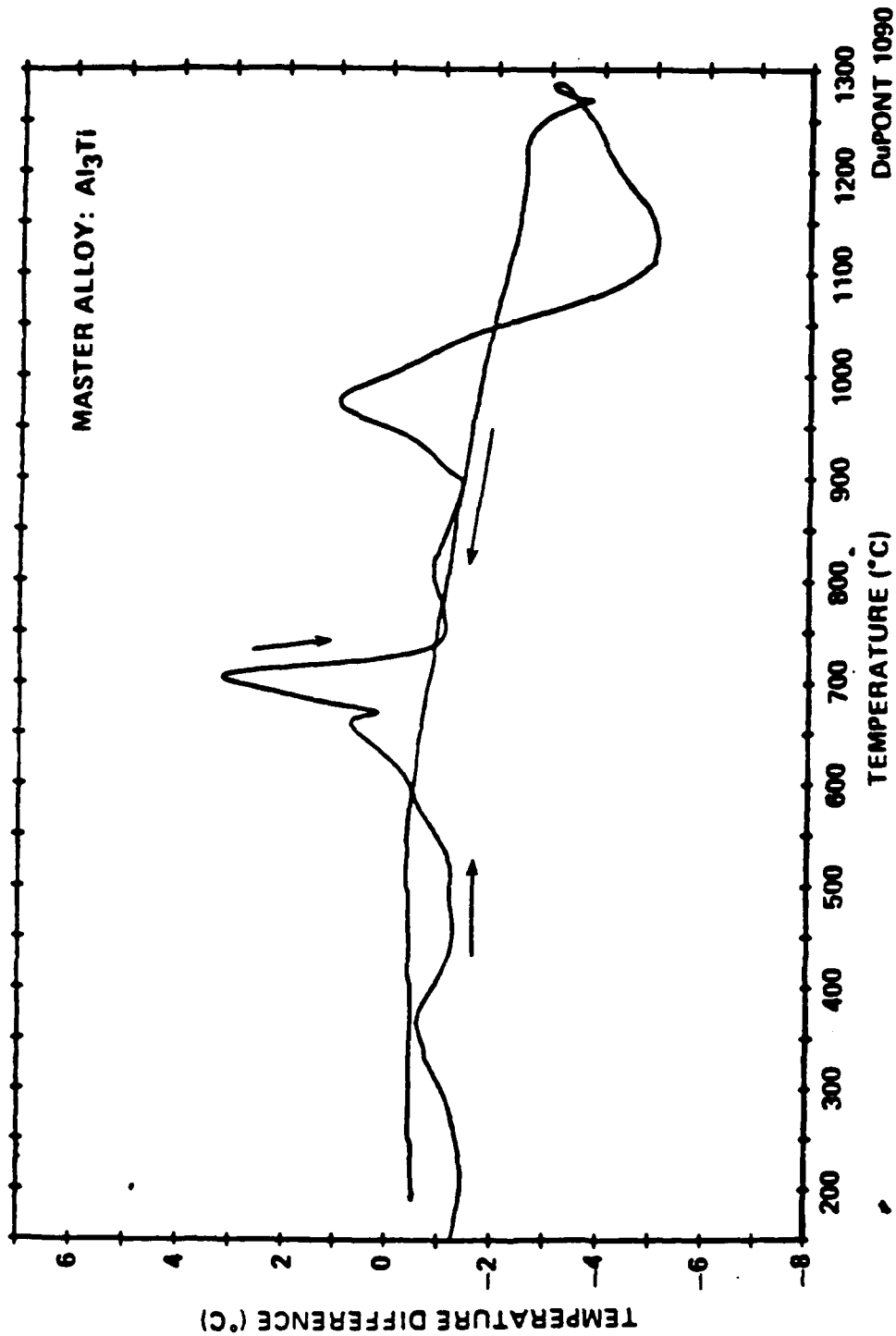


FIGURE 3.14 DIFFERENTIAL THERMAL ANALYSIS PROFILE OF THE Al_3Ti MASTER ALLOY

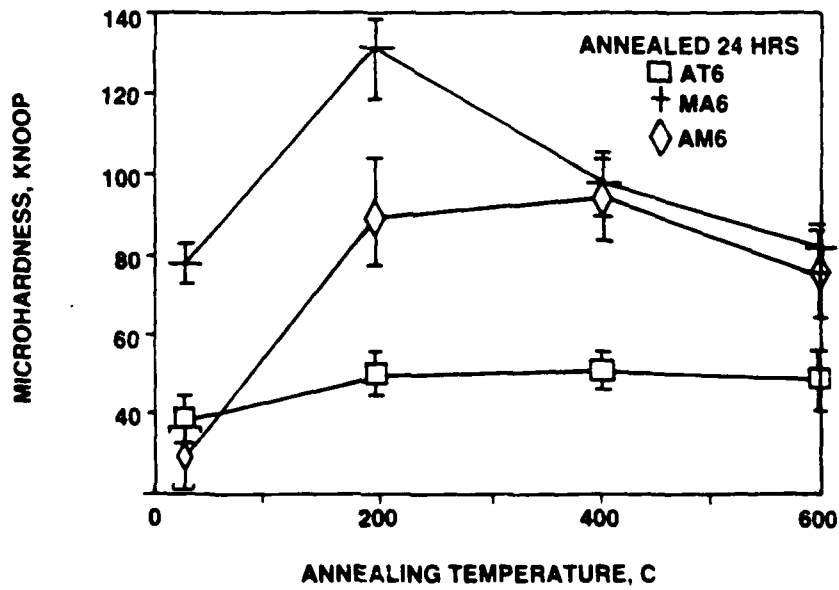
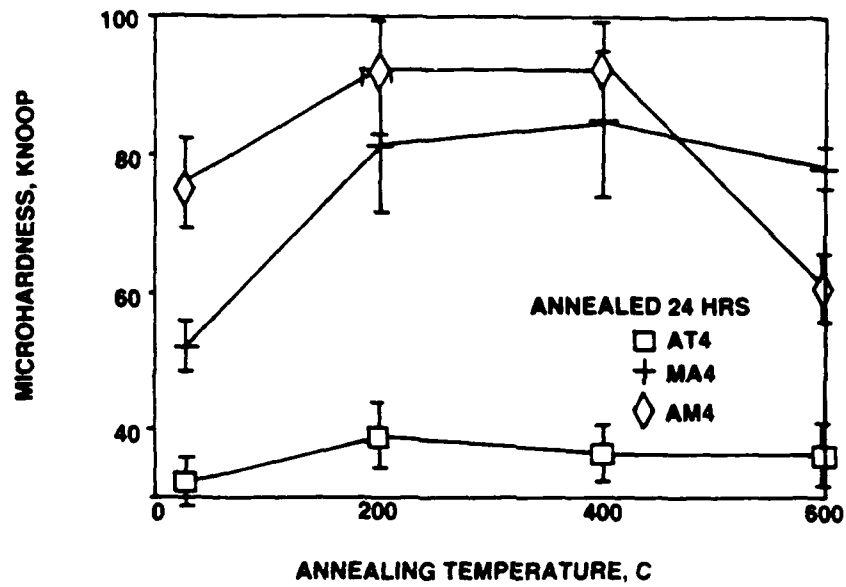


FIGURE 3.15 MICROHARDNESS OF ALLOY POWDERS ANNEALED FOR 24 HRS: a) 4 wt. % Ti AND b) 6 wt. % Ti

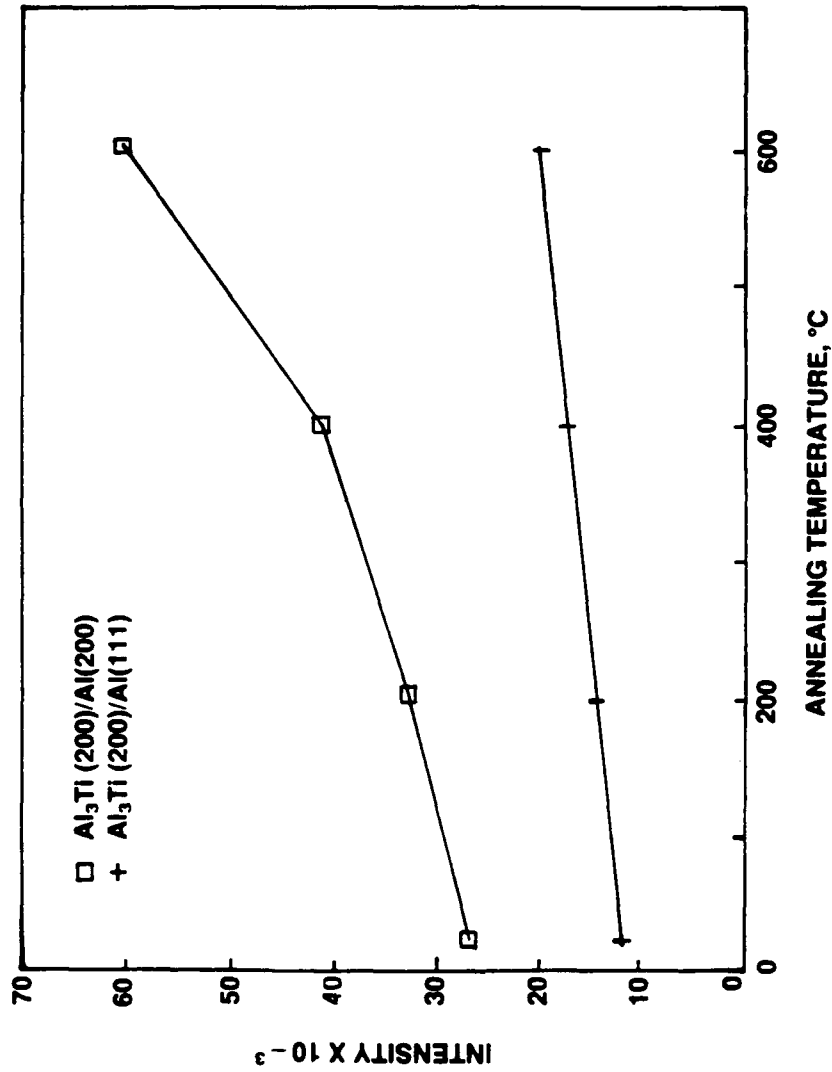


FIGURE 3.16 RELATIVE X-RAY DIFFRACTION PEAK INTENSITY OF Al_3Ti FOR ISOCHRONALLY ANNEALED AT4 POWDER

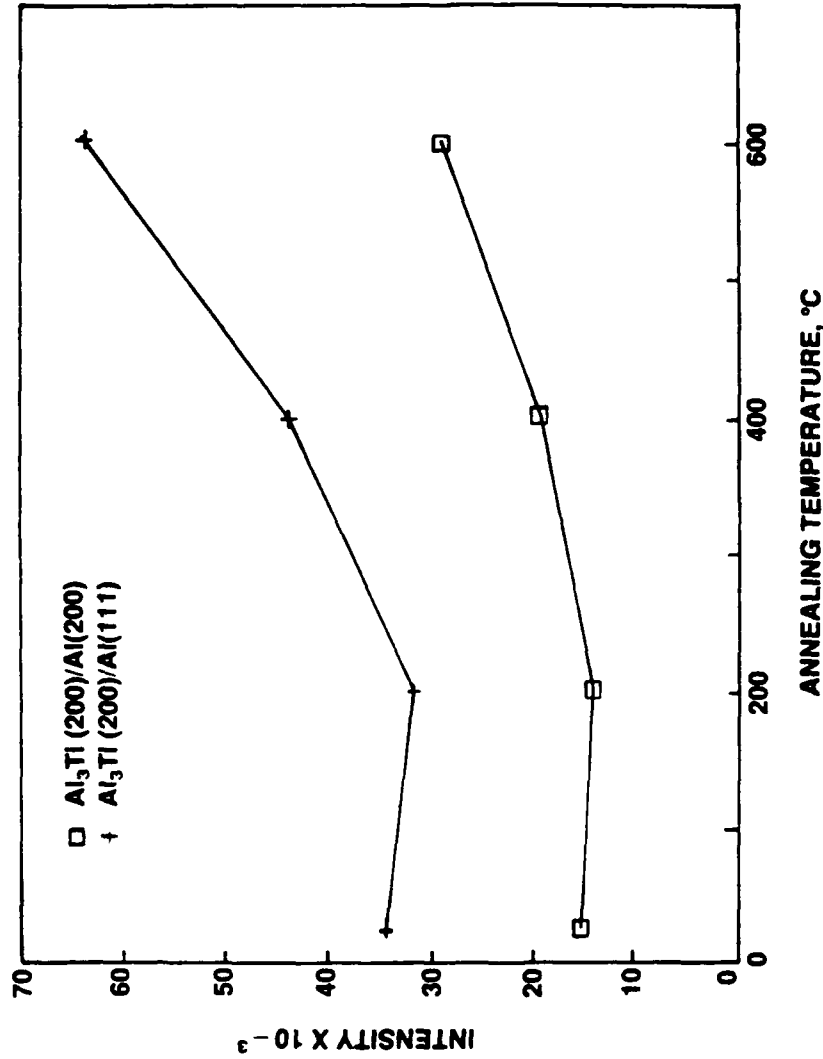


FIGURE 3.17 RELATIVE X-RAY DIFFRACTION PEAK INTENSITY OF Al_3Ti FOR ISOCHRONALLY ANNEALED AM4 POWDER

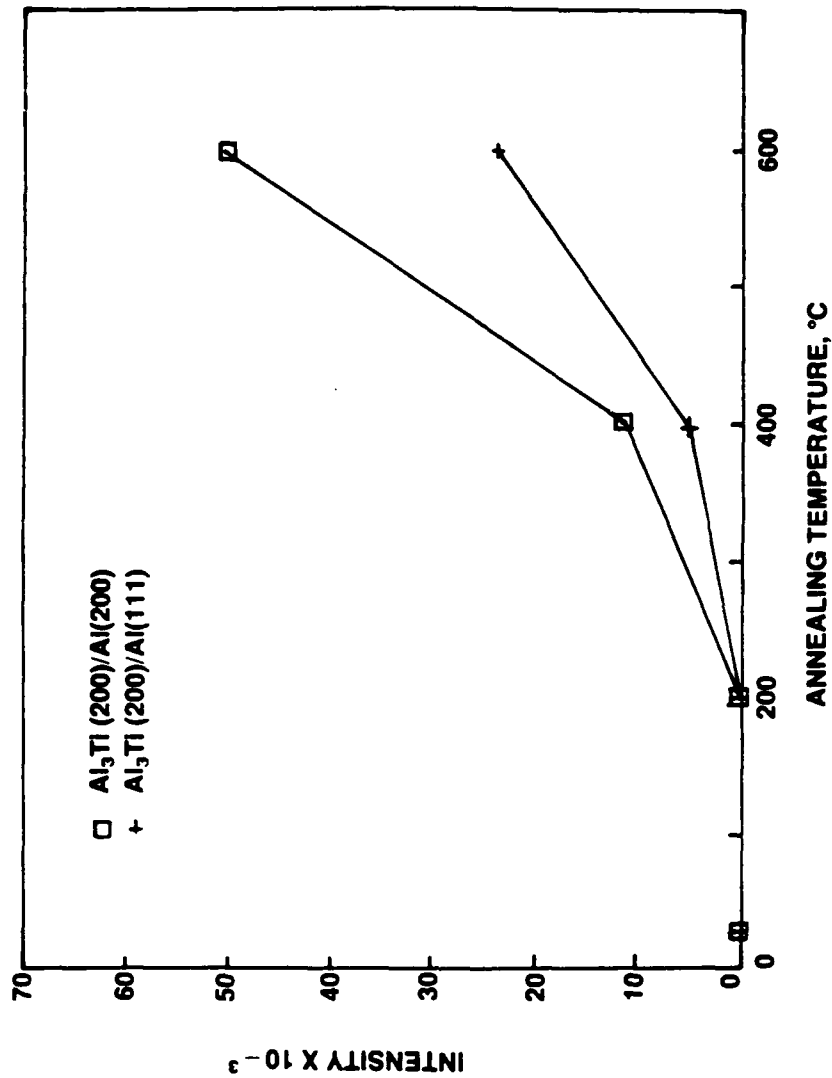
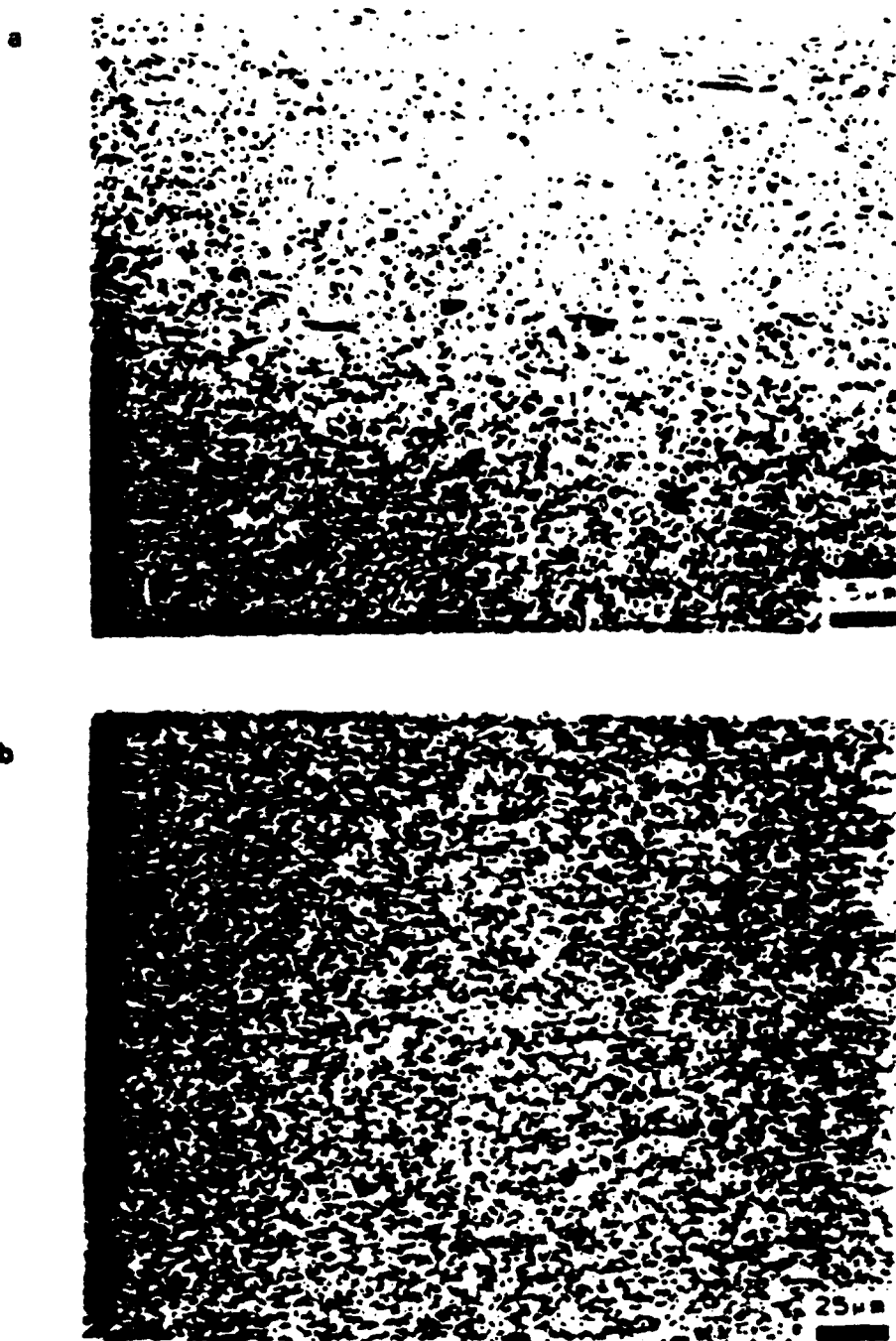
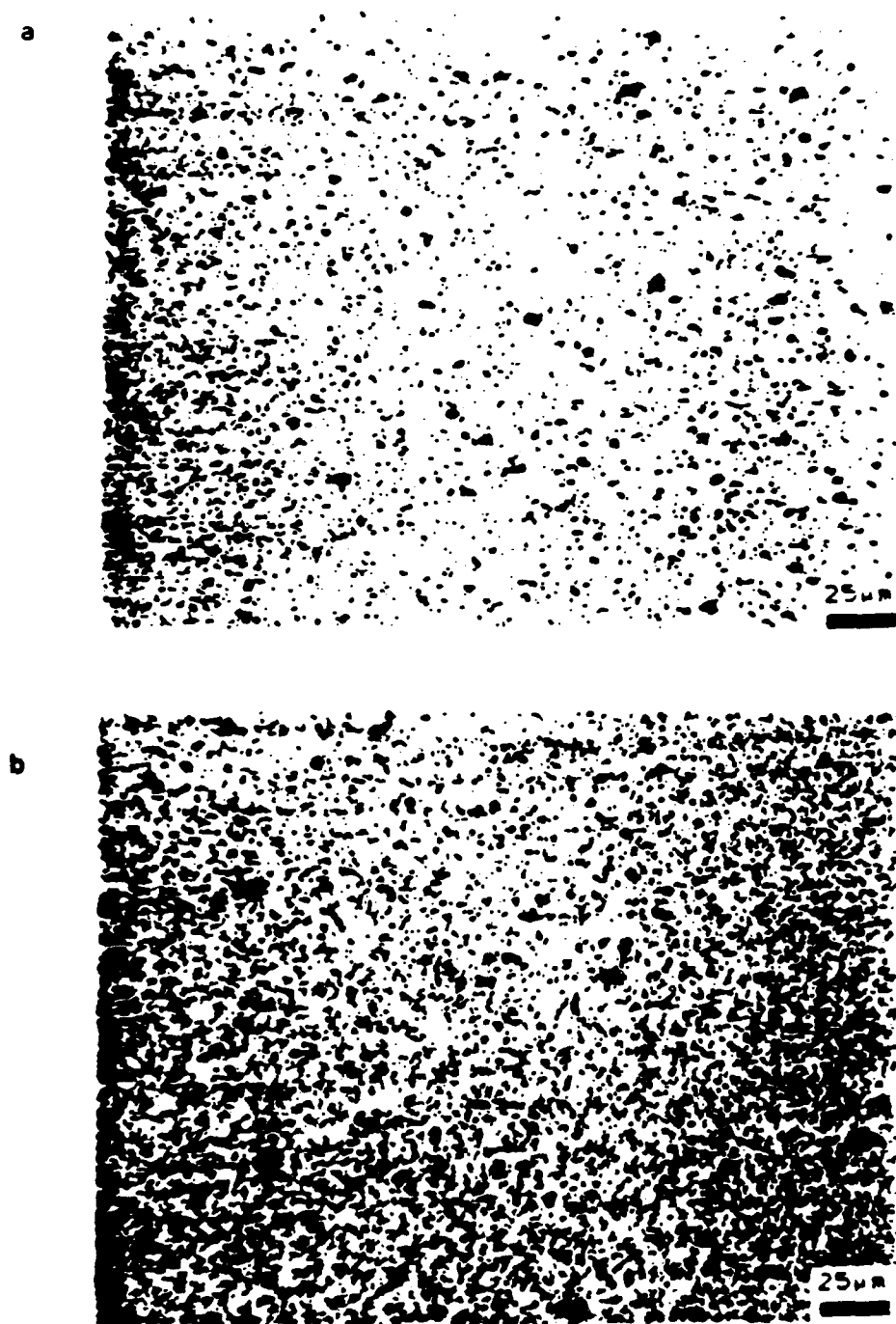


FIGURE 3.18 RELATIVE X-RAY DIFFRACTION PEAK INTENSITY OF Al_3Ti FOR ISOCHRONALLY ANNEALED MA4 POWDER



**FIGURE 3.19 OPTICAL MICROGRAPHS OF THE EXTRUDED
ALLOY ROD: AS-RECEIVED a) AT4 AND b) AT6**



**FIGURE 3.20 OPTICAL MICROGRAPHS OF THE EXTRUDED
ALLOY ROD: AS-RECEIVED a) AM4 AND b) AM6**

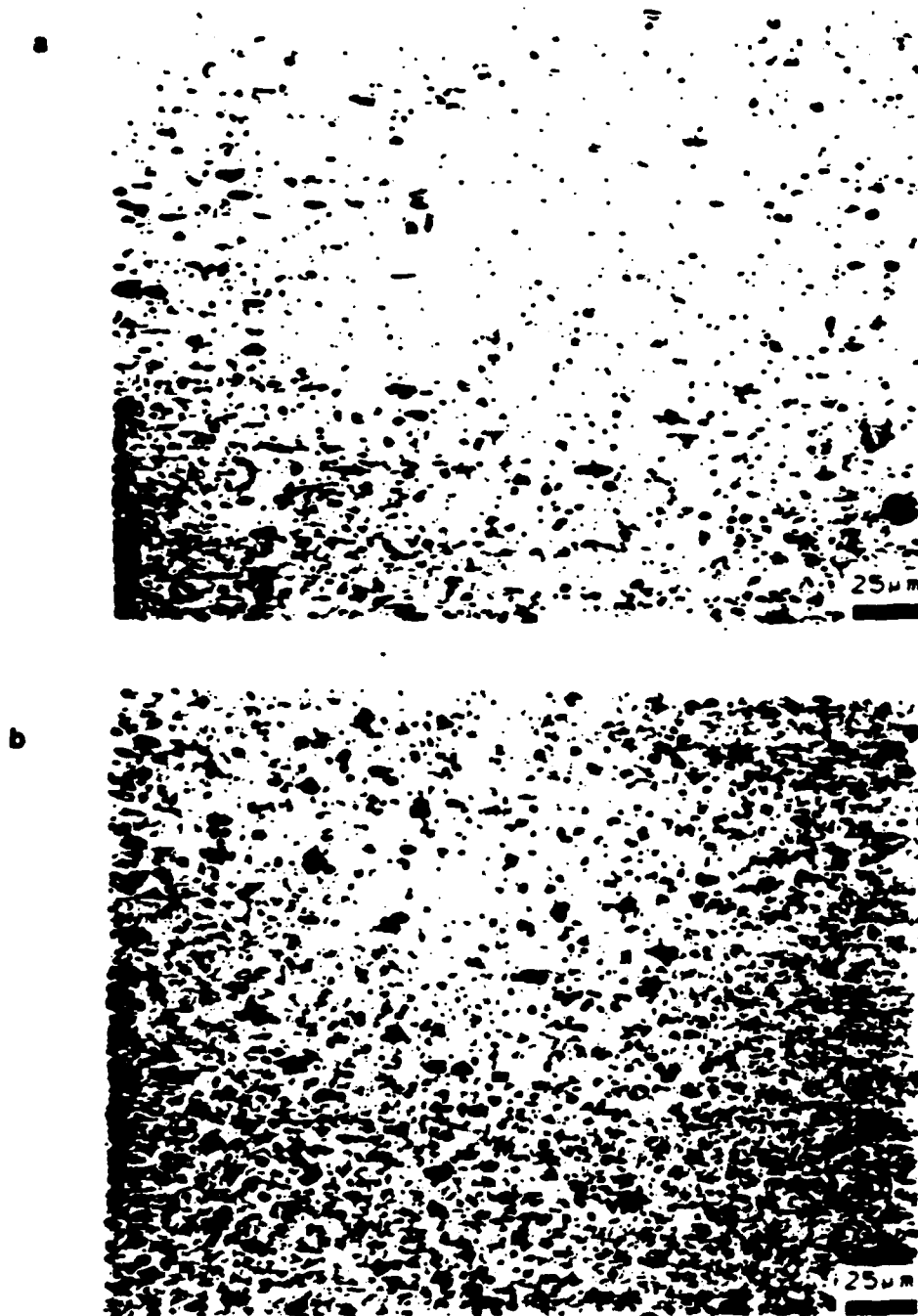


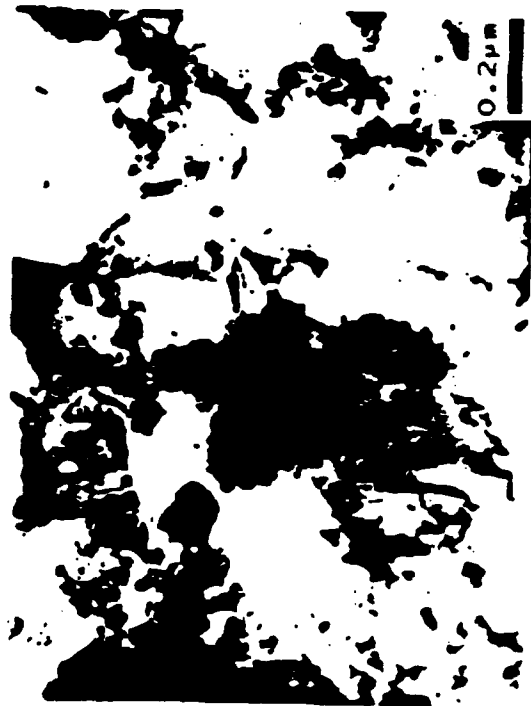
**FIGURE 3.21 OPTICAL MICROGRAPHS OF THE EXTRUDED
ALLOY ROD: AS-RECEIVED a) MA4 AND b) MA6**



b



a



c

**FIGURE 3.22 TRANSMISSION ELECTRON
MICROGRAPHS OF EXTRUDED a) AT4, b) AM4,
AND c) MA4**



b



a



c

FIGURE 3.23 TRANSMISSION ELECTRON
MICROGRAPHS OF EXTRUDED a) AT6, b) AM6,
AND c) MA6



b



a



c

**FIGURE 3.25 TRANSMISSION ELECTRON
MICROGRAPHS OF EXTRUDED AND ANNEALED
(300 C, 100 HRS): a) AT6, b) AM6, AND c) MA6**

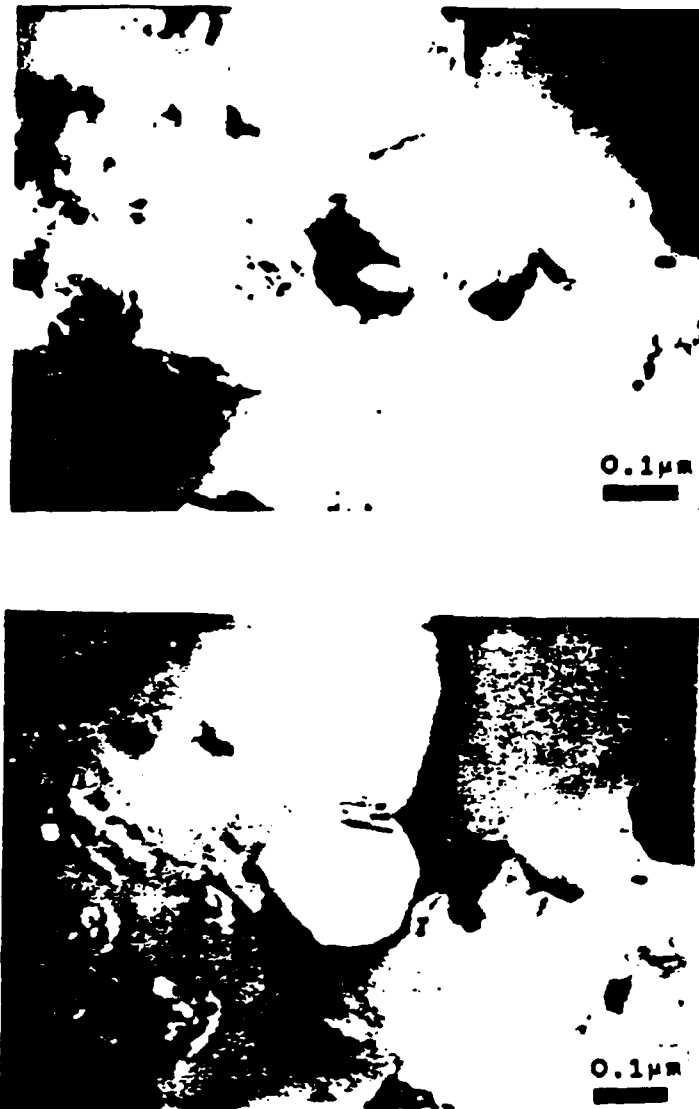


**FIGURE 3.26 BRIGHT FIELD/DARK FIELD TRANSMISSION
ELECTRON MICROGRAPH PAIR OF EXTRUDED AM4**

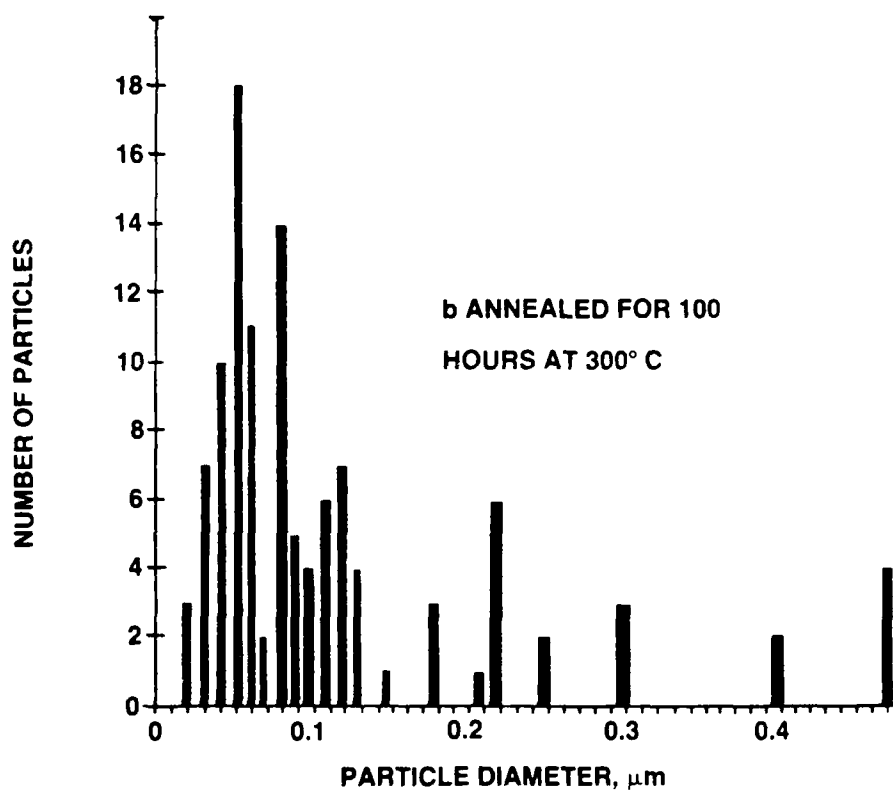
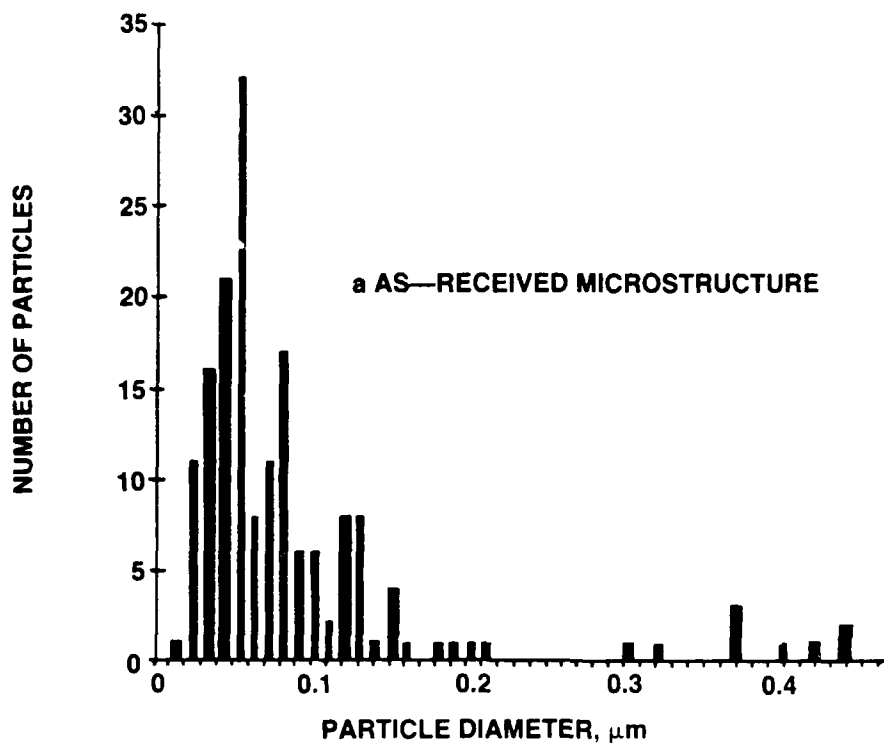


FIGURE 3.27 PARTICLE SIZE DISTRIBUTION OF THE Al_3Ti ALUMINIDE OF THE a) AS-RECEIVED AND b) ANNEALED (300 C FOR 100 hrs.) ALLOYS

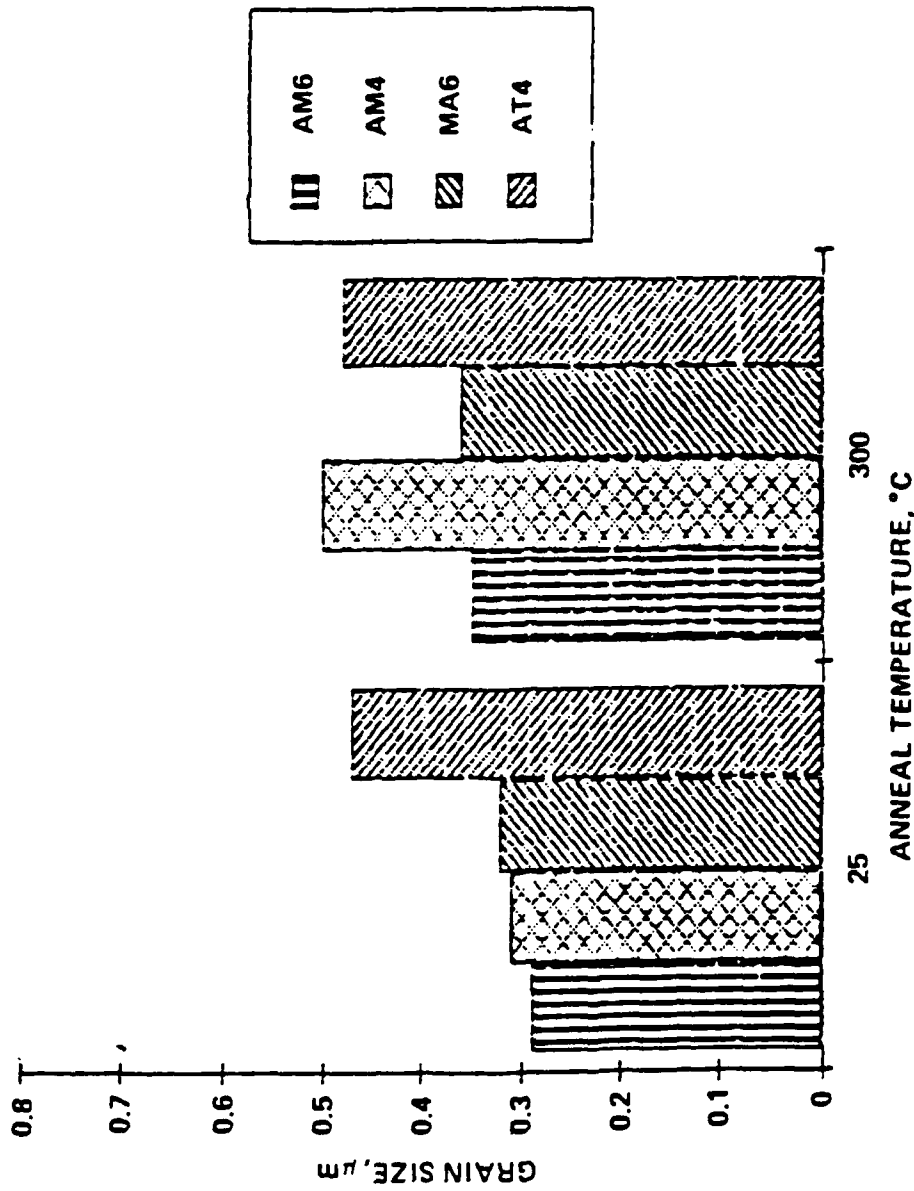
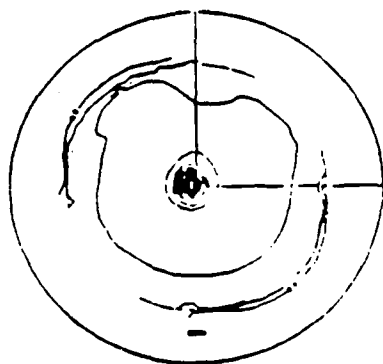
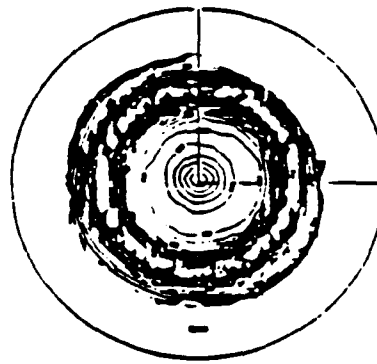


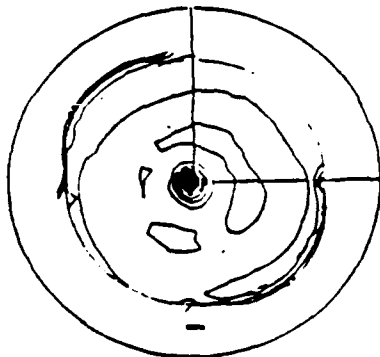
FIGURE 3.28 GRAIN SIZE VARIATION OF THE AS-RECEIVED AND ANNEALED (300 C, FOR 100 HRS) ALLOYS YIELD STRENGTH OF ISOCHRONALLY ANNEALED (100 HRS) ALLOYS



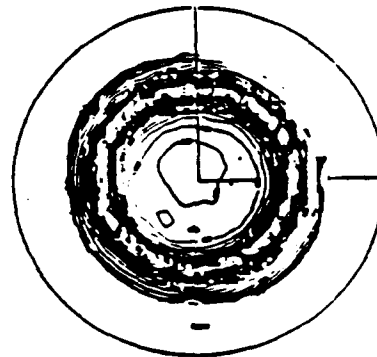
AT4(111)



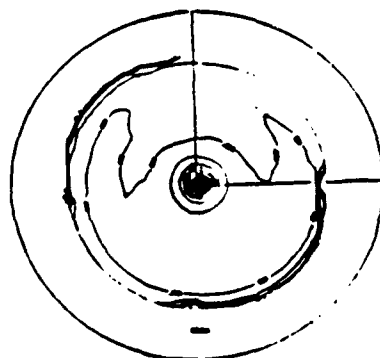
AT4(200)



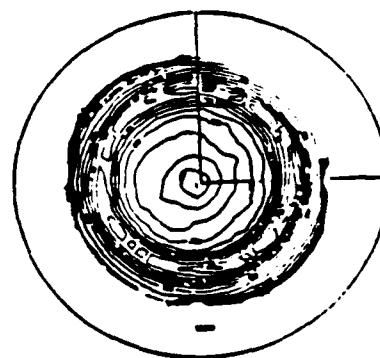
AM4(111)



AM4(200)

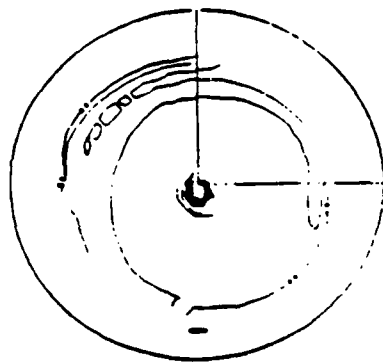


MA4(111)

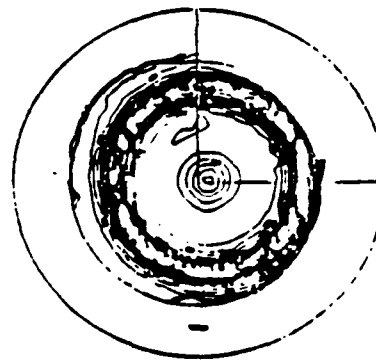


MA4(200)

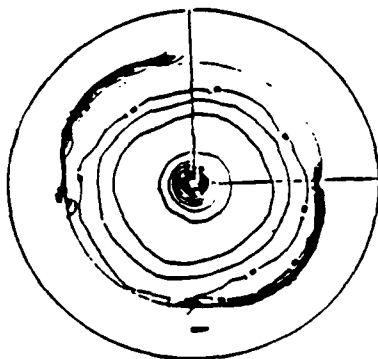
**FIGURE 3.29 (111) AND (200) POLE
FIGURES FOR AS-RECEIVED ALLOYS CONTAINING 4 wt. % TITANIUM**



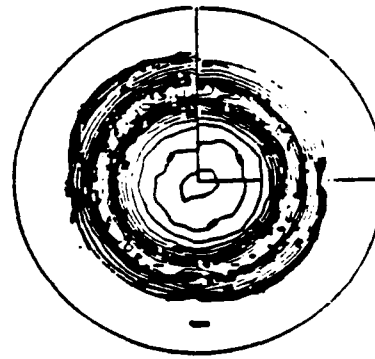
AT6(111)



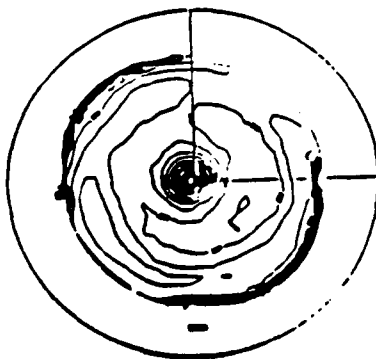
AT6(200)



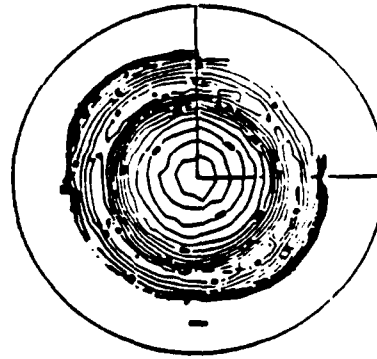
AM6(111)



AM6(200)



MA6(111)



MA6(200)

**FIGURE 3.30 (111) AND (200) POLE
FIGURES FOR AS-RECEIVED ALLOYS CONTAINING 6 wt. % TITANIUM**

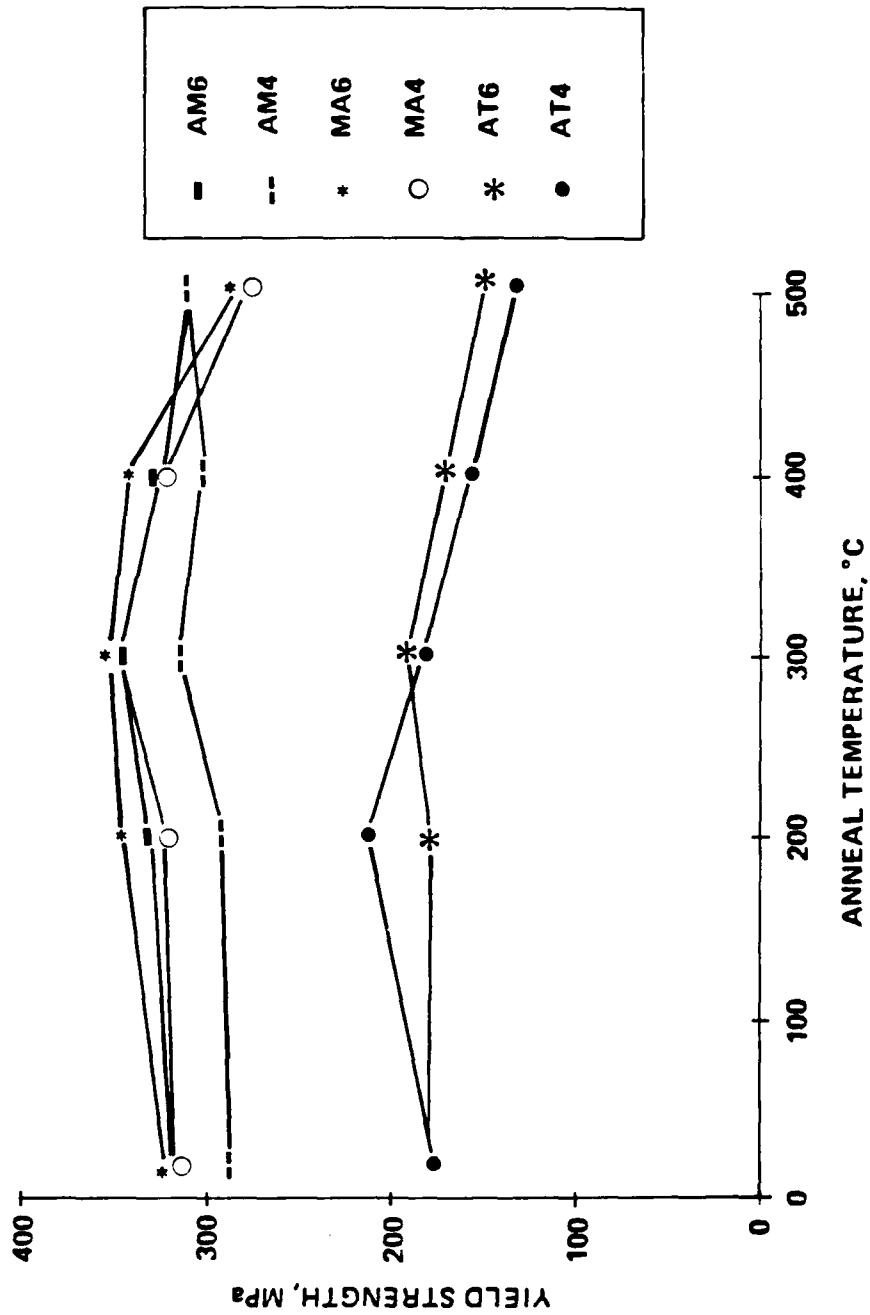


FIGURE 3.31 YIELD STRENGTH OF ISOCHRONALLY ANNEALED (100 hrs.) ALLOYS

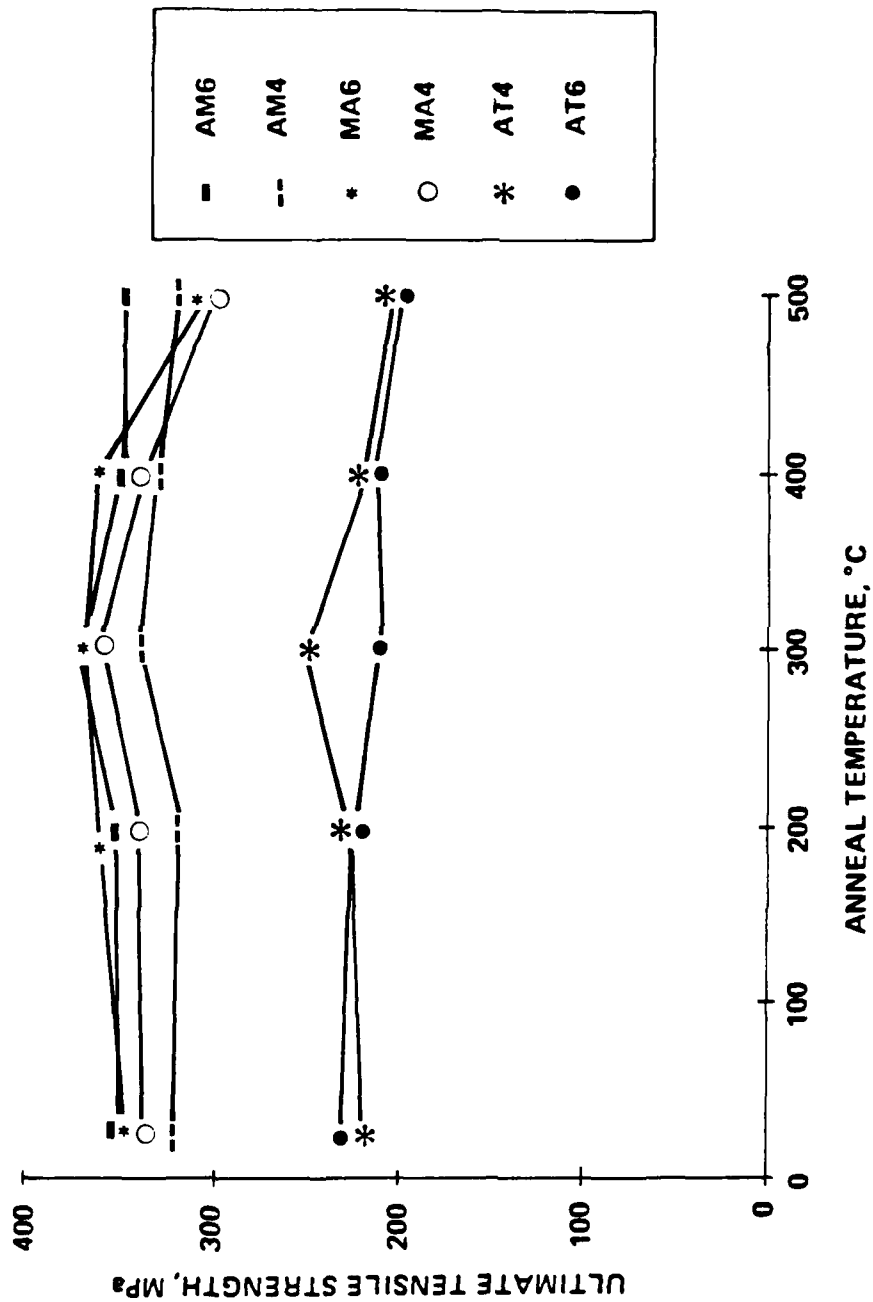


FIGURE 3.32 TENSILE STRENGTH OF ISOCHRONALLY ANNEALED (100 HRS)
ALLOYS

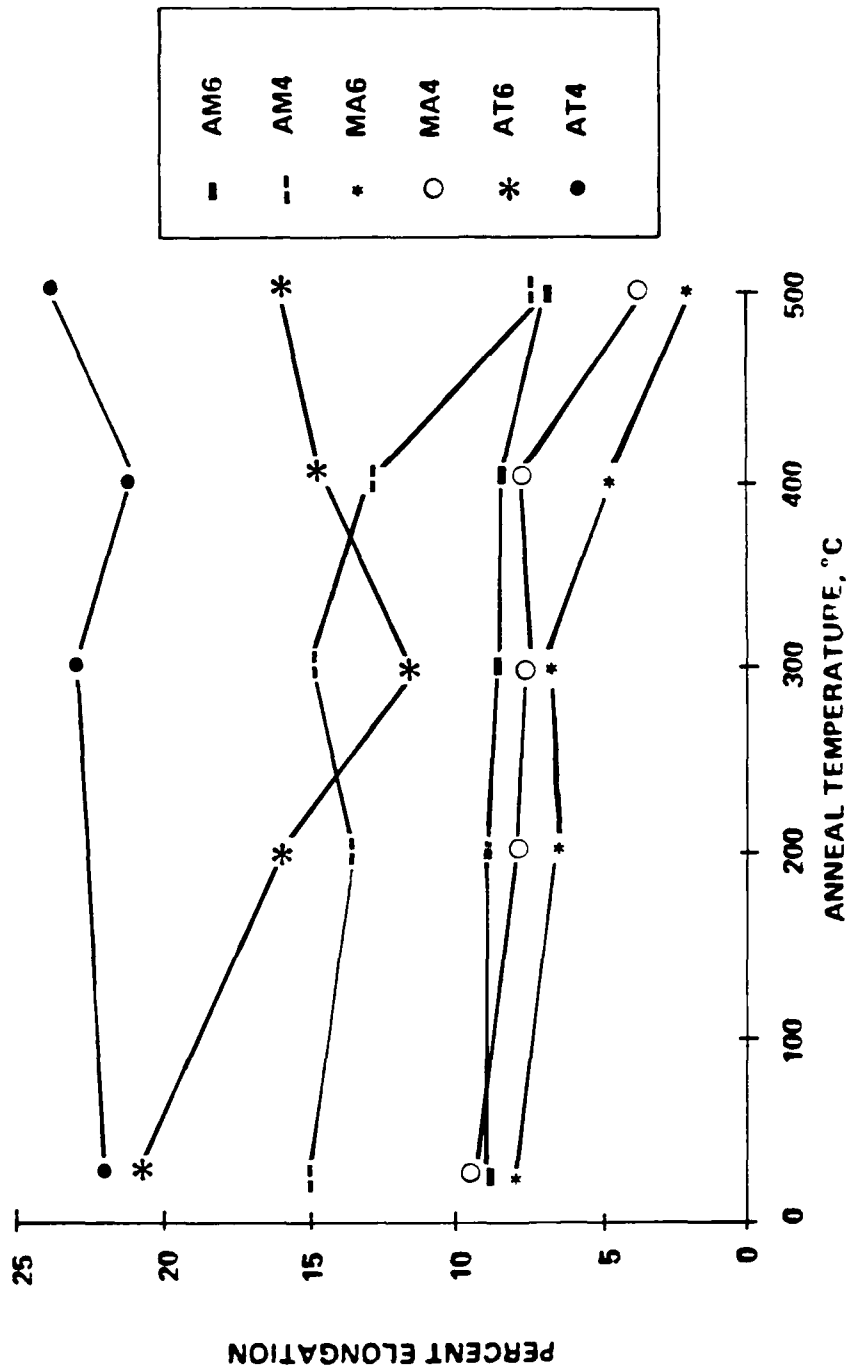


FIGURE 3.33 TENSILE ELONGATION OF ISOTHERMALLY ANNEALED (100 HRS) ALLOYS

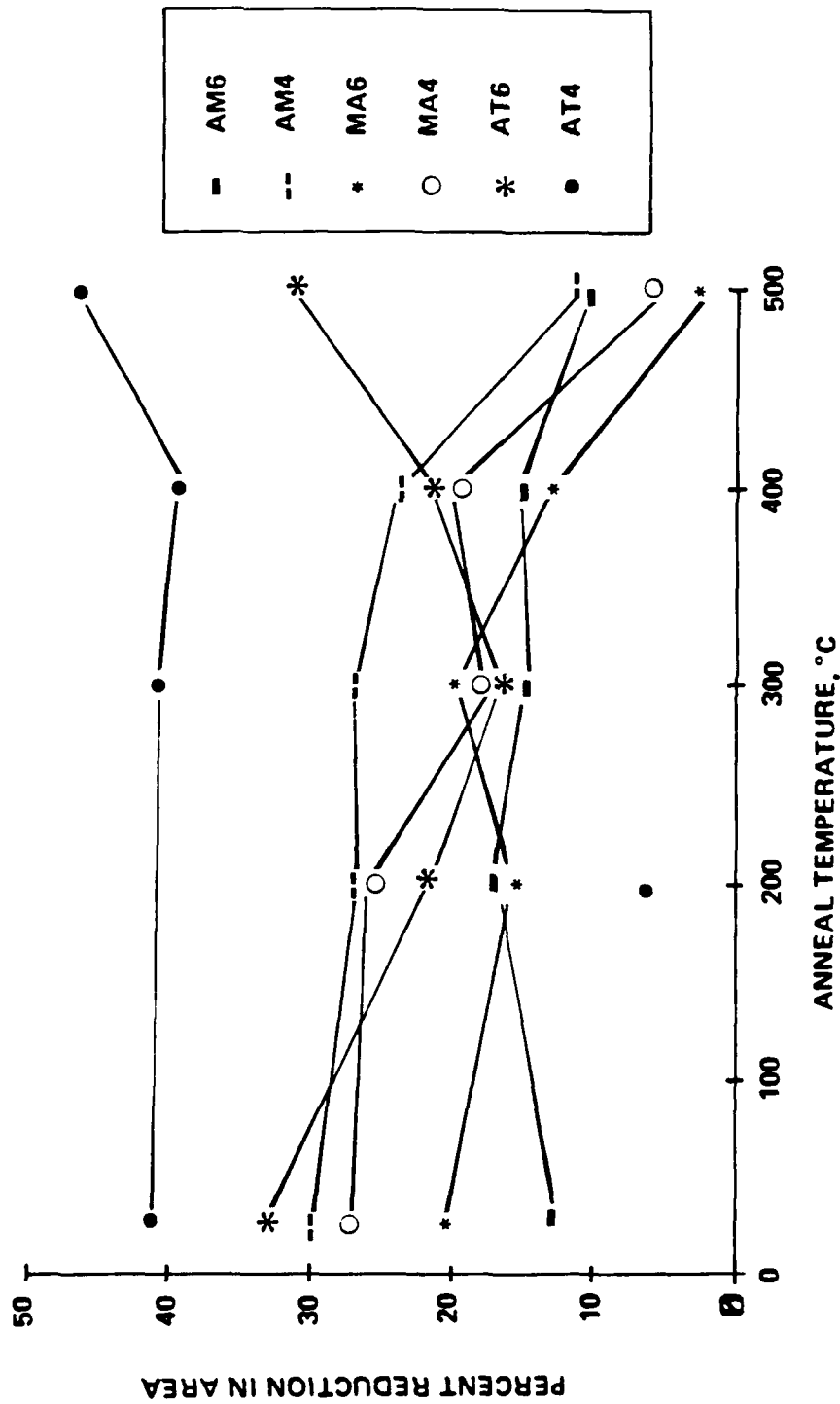


FIGURE 3.34 REDUCTION IN AREA OF ISOCHRONALLY ANNEALED (100 HRS)
ALLOYS

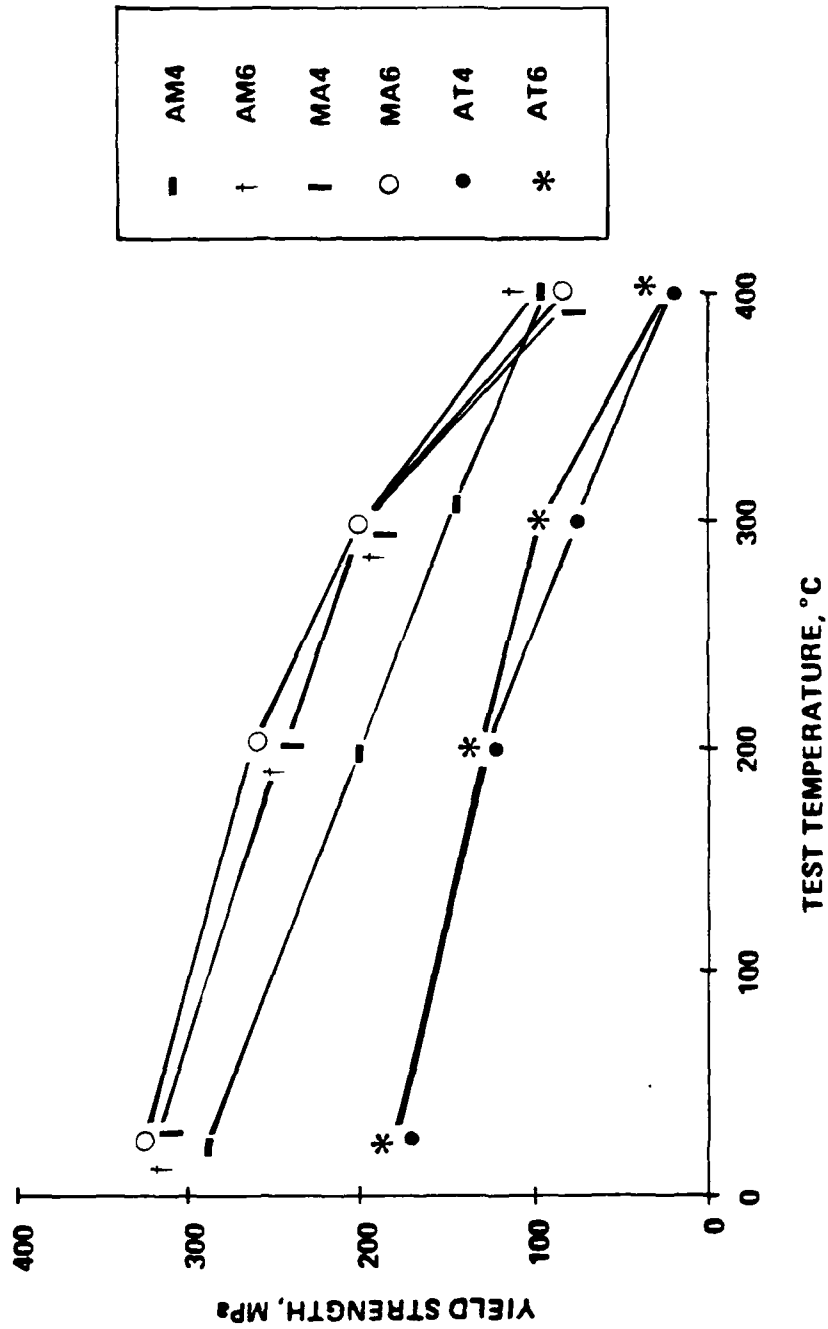


FIGURE 3.35 YIELD STRENGTH OF THE ALUMINUM-TITANIUM ALLOYS
TESTED AT TEMPERATURE

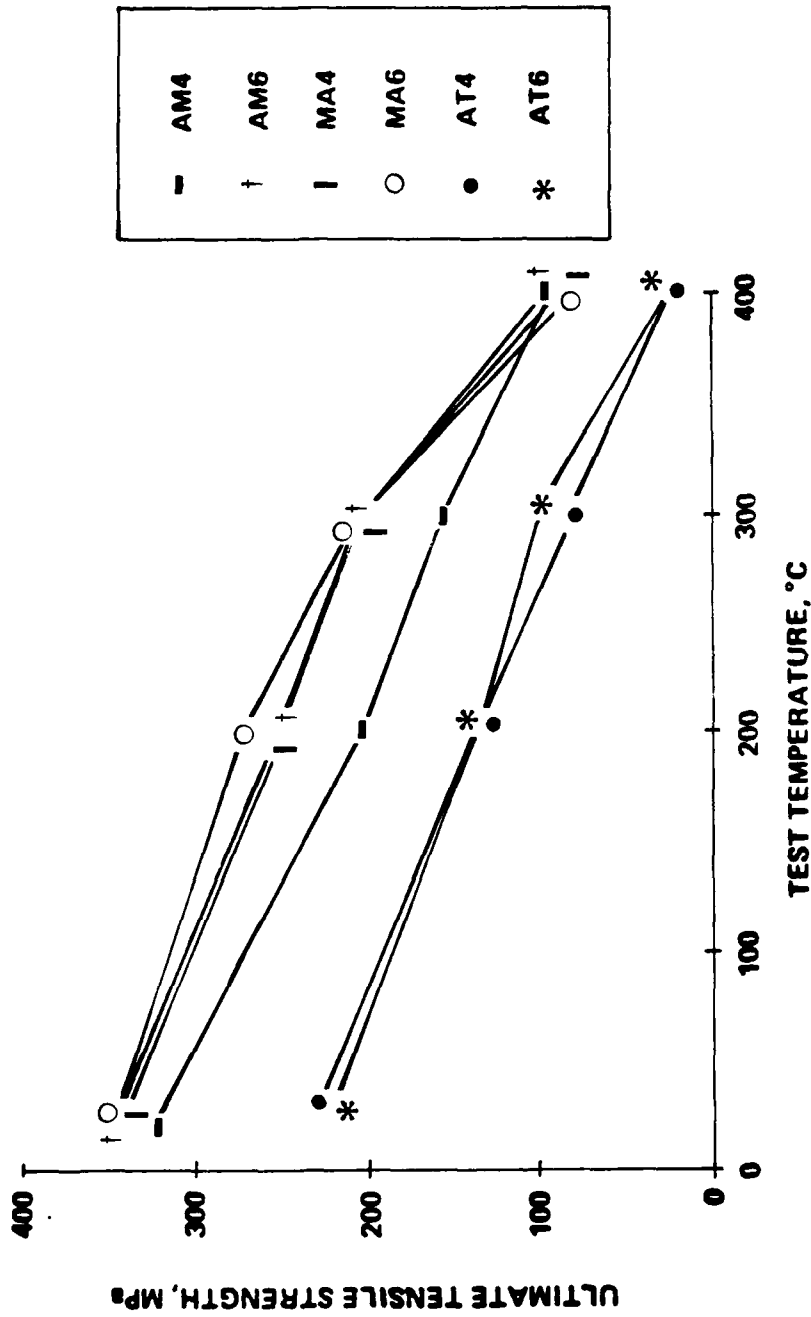


FIGURE 3.36 TENSILE STRENGTH OF THE ALUMINUM-TITANIUM ALLOYS TESTED AT TEMPERATURE

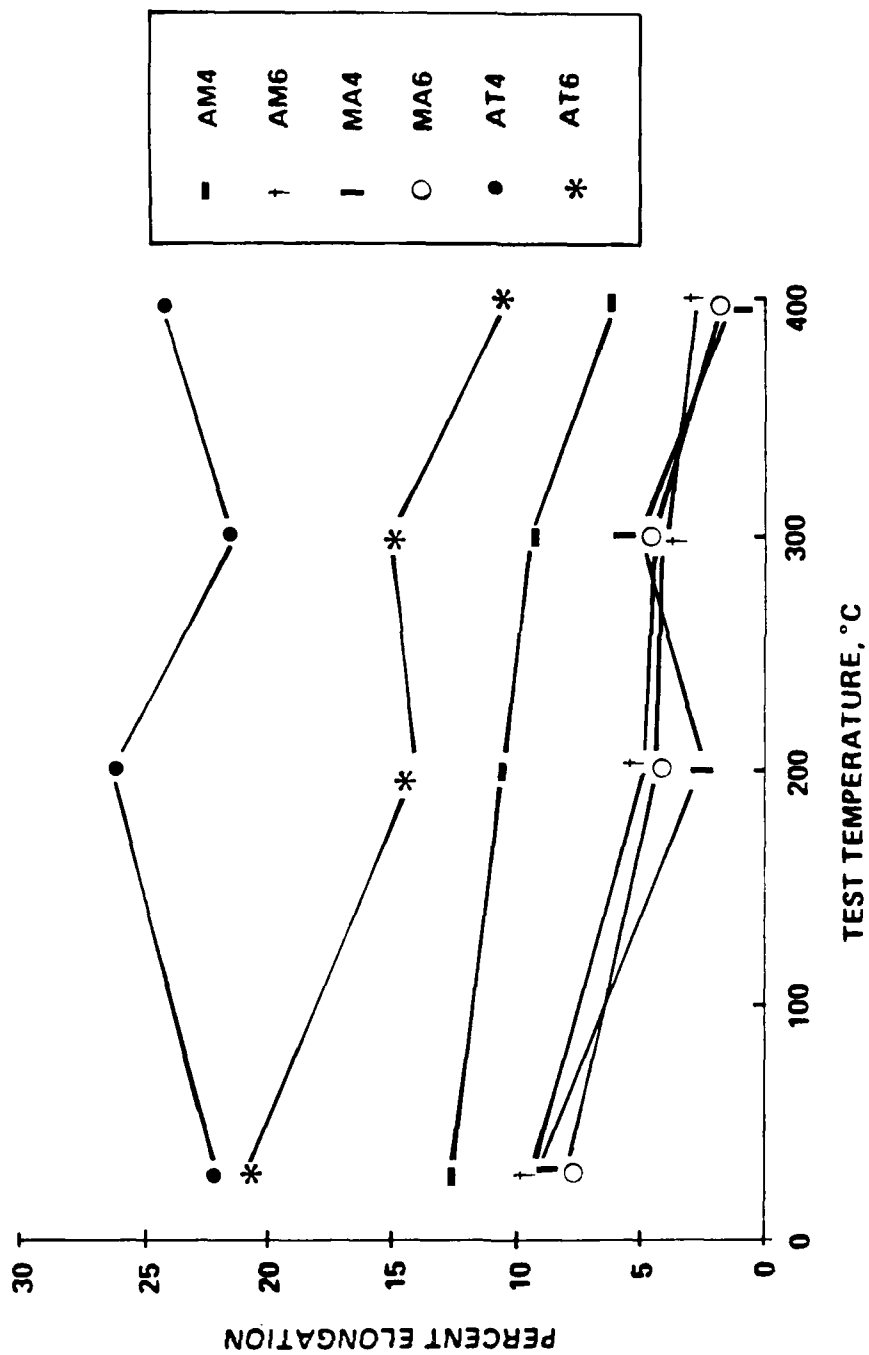


FIGURE 3.37 TENSILE ELONGATION OF THE ALUMINUM-TITANIUM ALLOYS TESTED AT TEMPERATURE

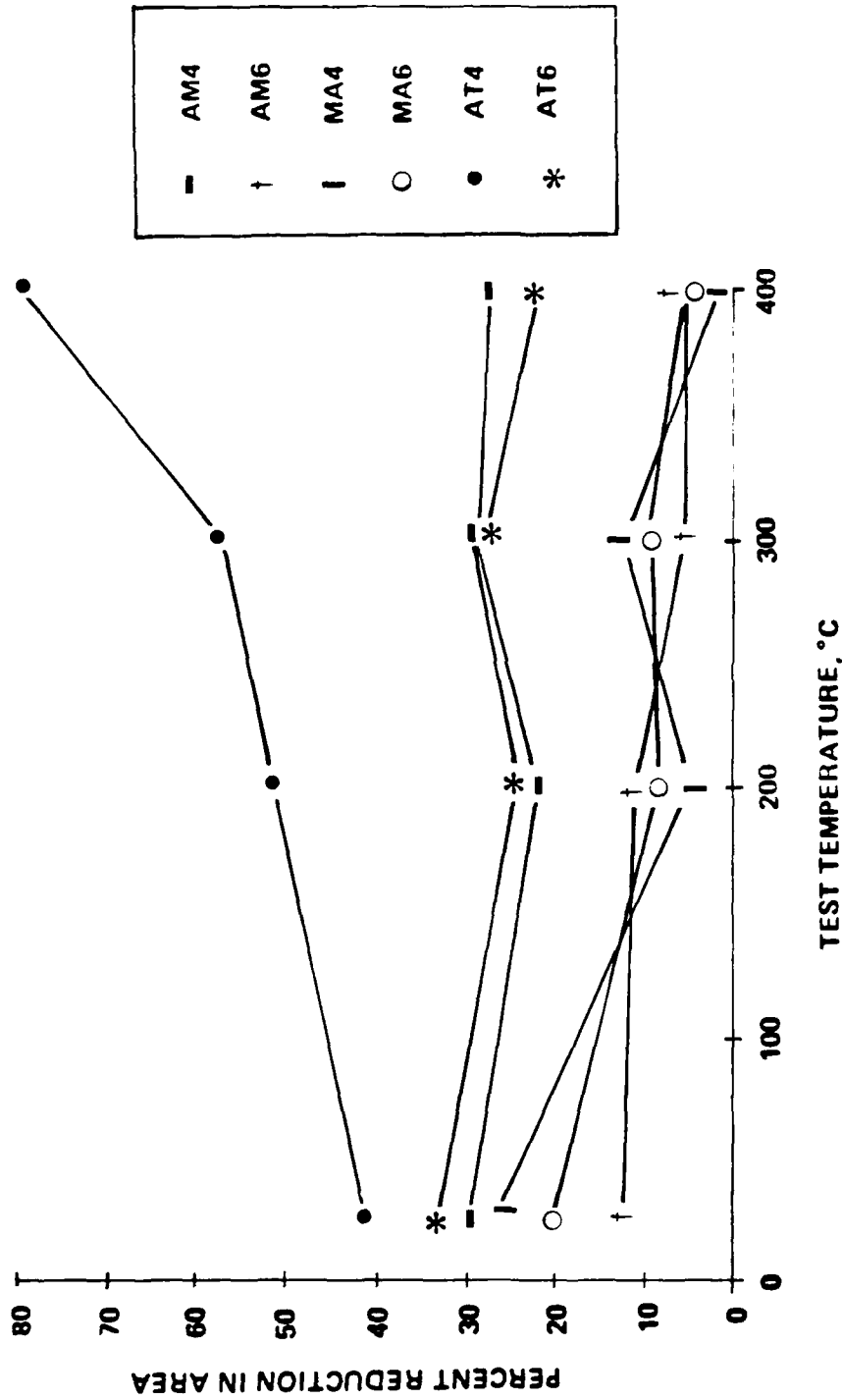
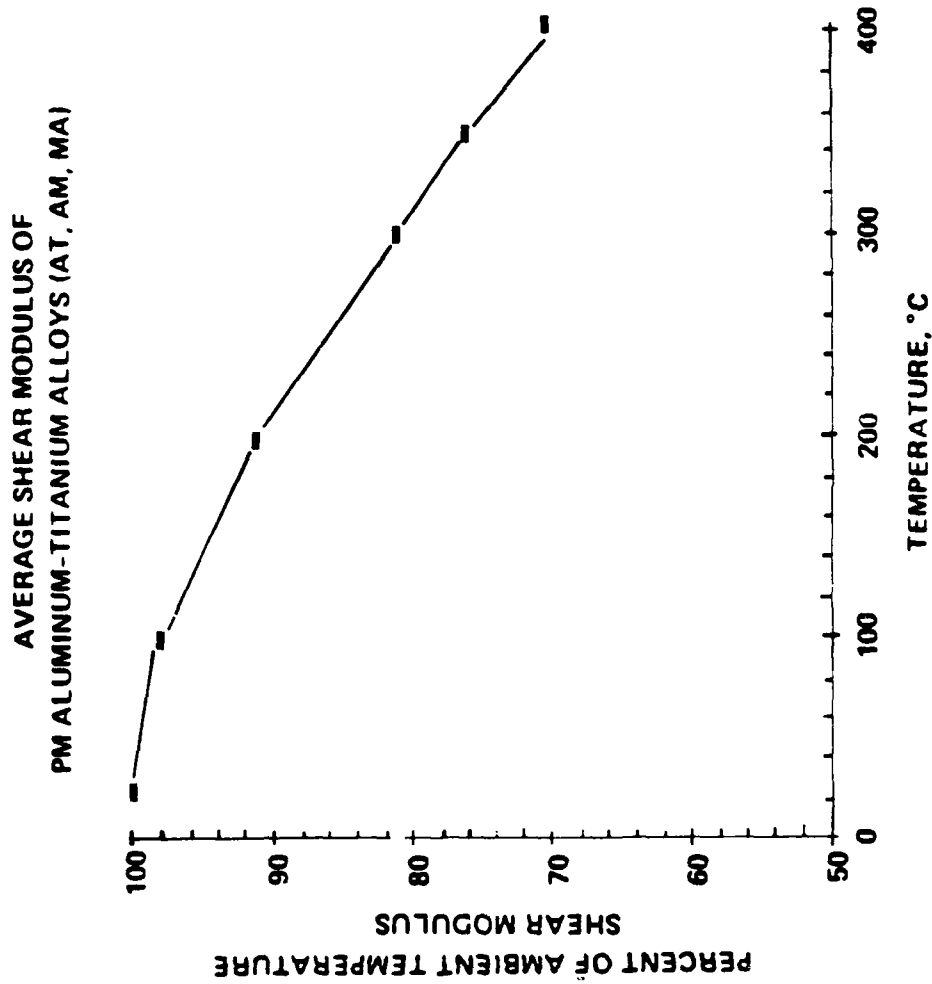


FIGURE 3.38 REDUCTION IN AREA OF THE ALUMINUM-TITANIUM ALLOYS TESTED AT TEMPERATURE



**FIGURE 3.39 SHEAR MODULUS OF THE ALUMINUM-TITANIUM ALLOYS
MEASURED AS A FUNCTION OF TEMPERATURE USING DYNAMICAL
MECHANICAL ANALYSIS**

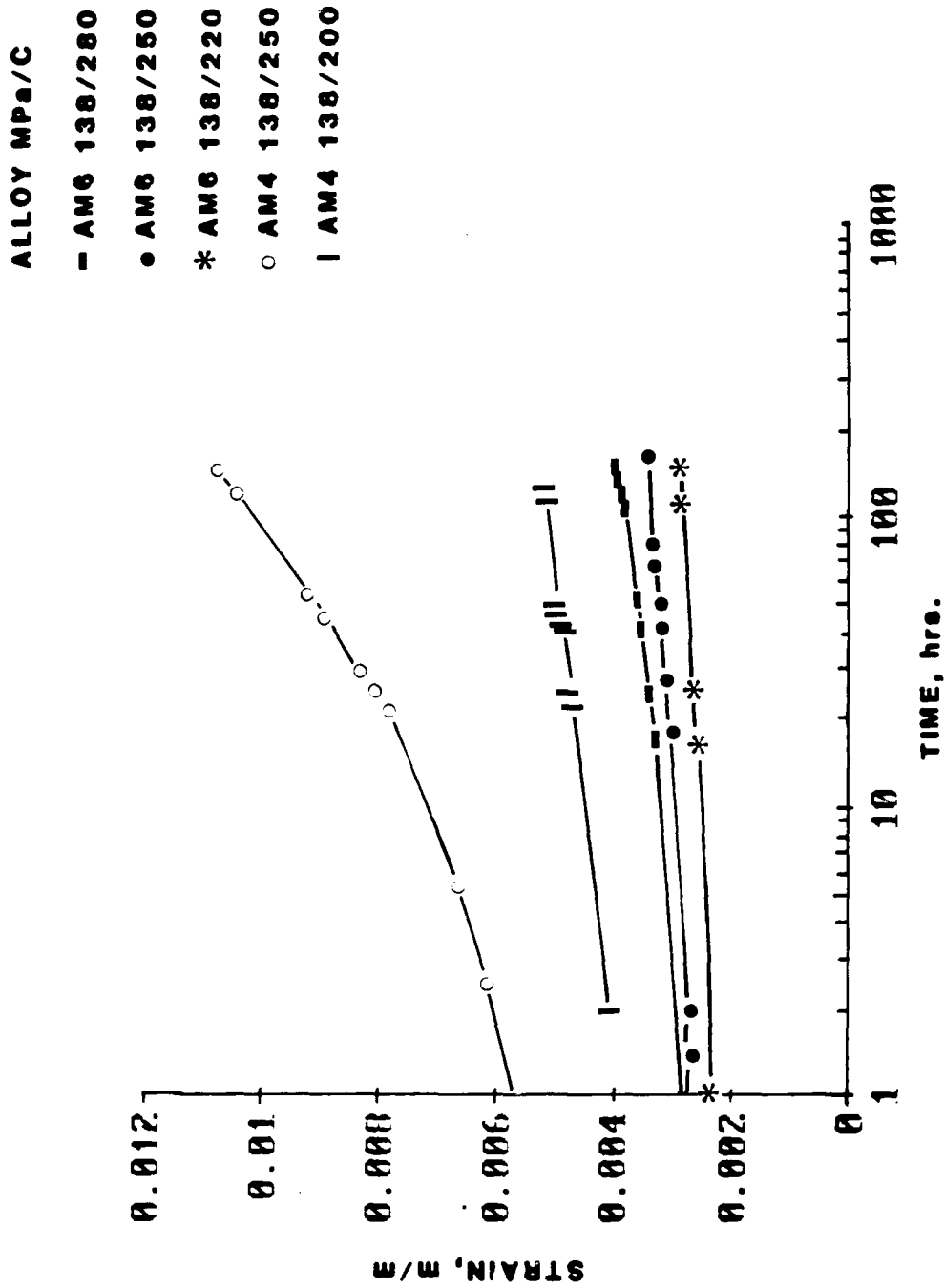


FIGURE 3.40 CREEP RESPONSE OF ALLOYS AM4 AND AM6 AT 138 MPa



FIGURE 3.41 CREEP RESPONSE OF ALLOYS MA4 AND MA6 AT 138 MPa

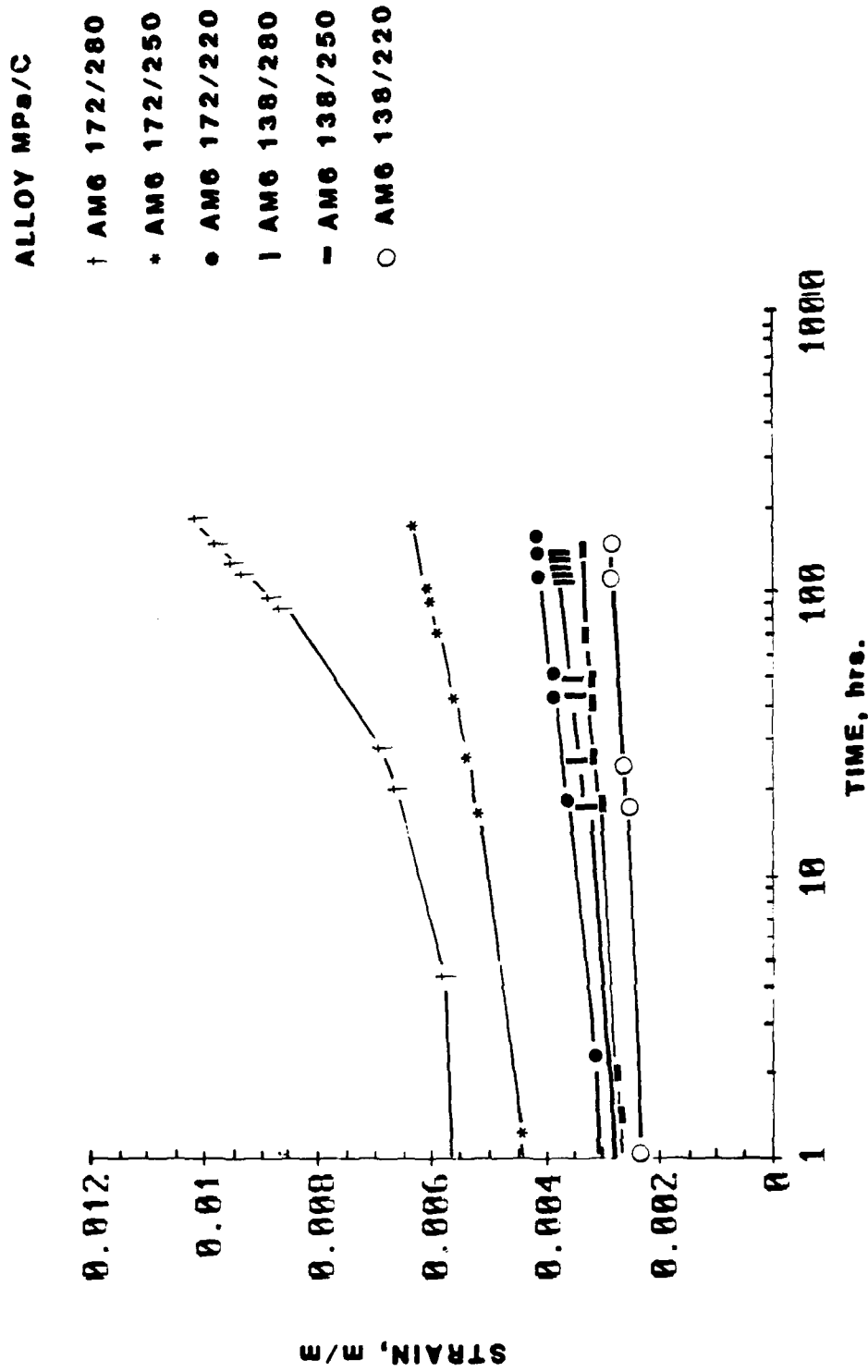


FIGURE 3.42 CREEP RESPONSE OF ALLOY AM6 AT 138 AND 172 MPa

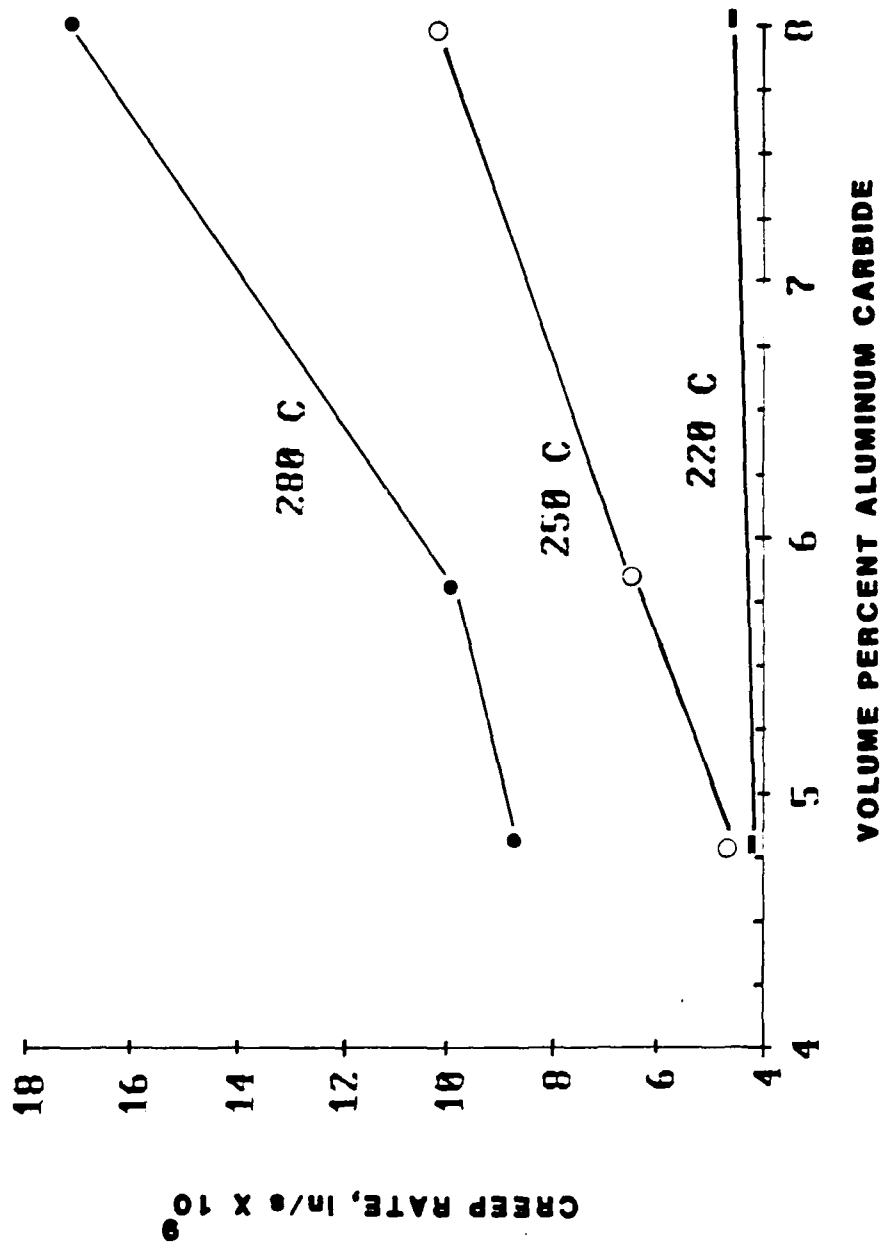


FIGURE 3.43 CREEP RATE VERSUS VOLUME PERCENT Al_4C_3

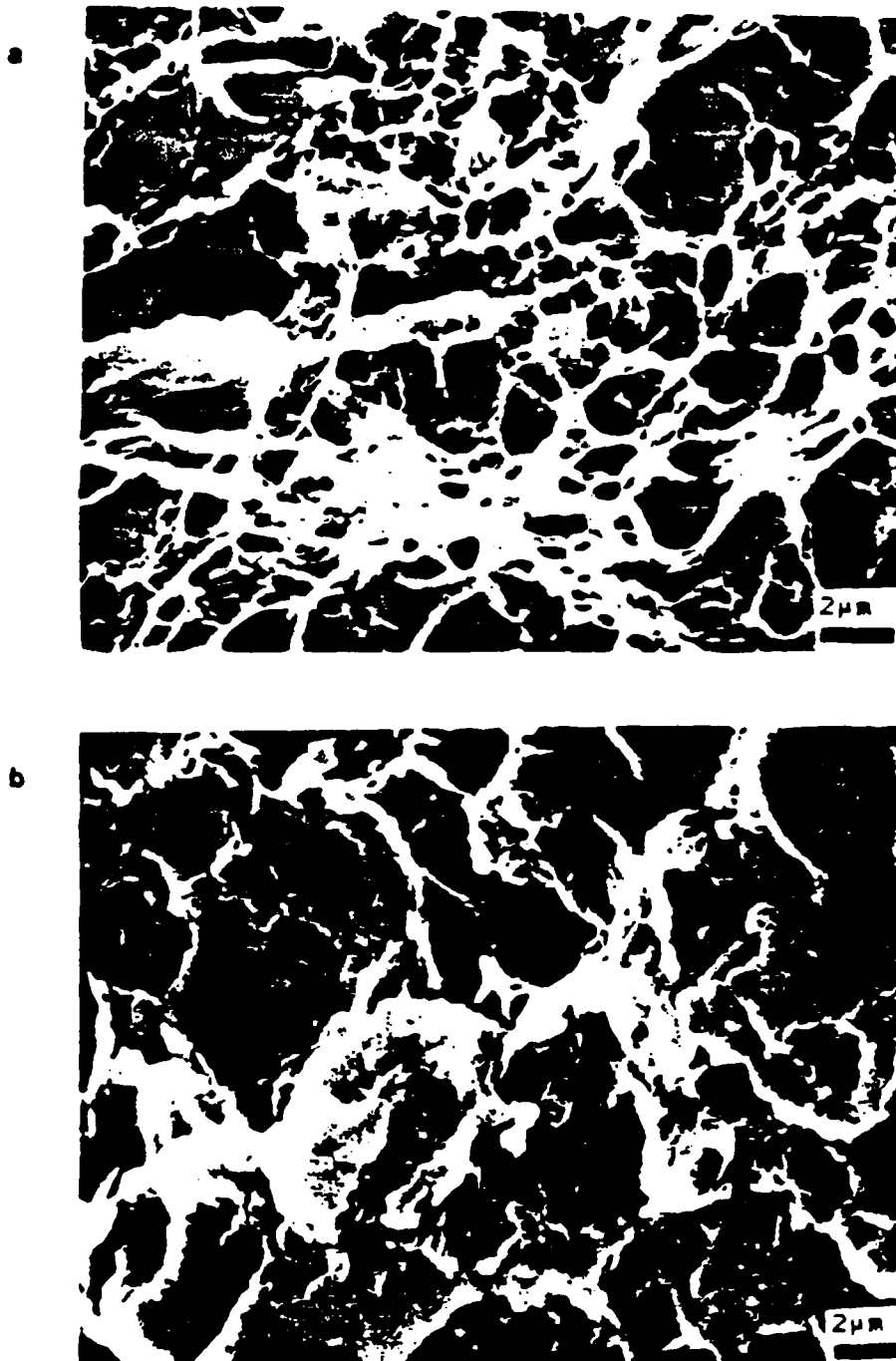


FIGURE 3.44 SCANNING ELECTRON MICROSCOPY
TENSILE FRACTOGRAPHS OF AT4: a) AS-RECEIVED
AND b) TESTED AT 300 C

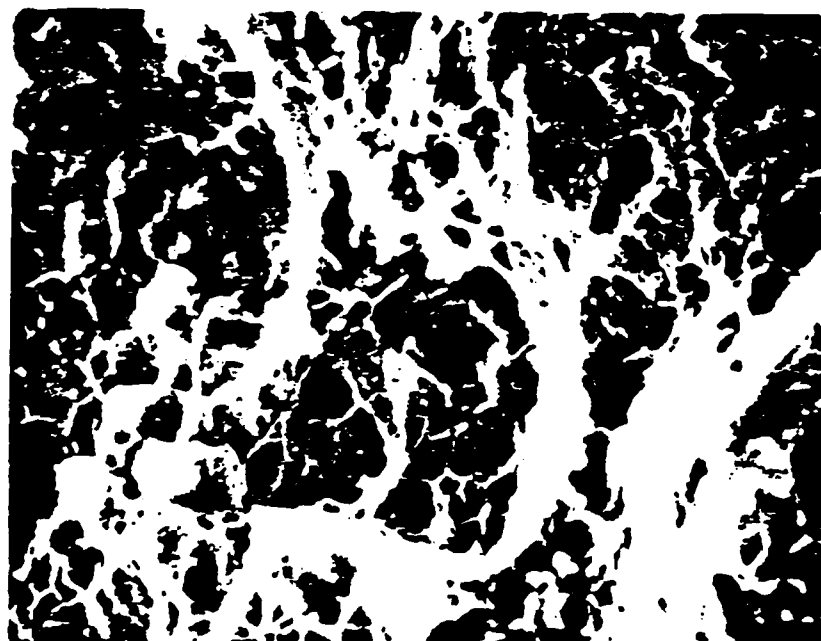
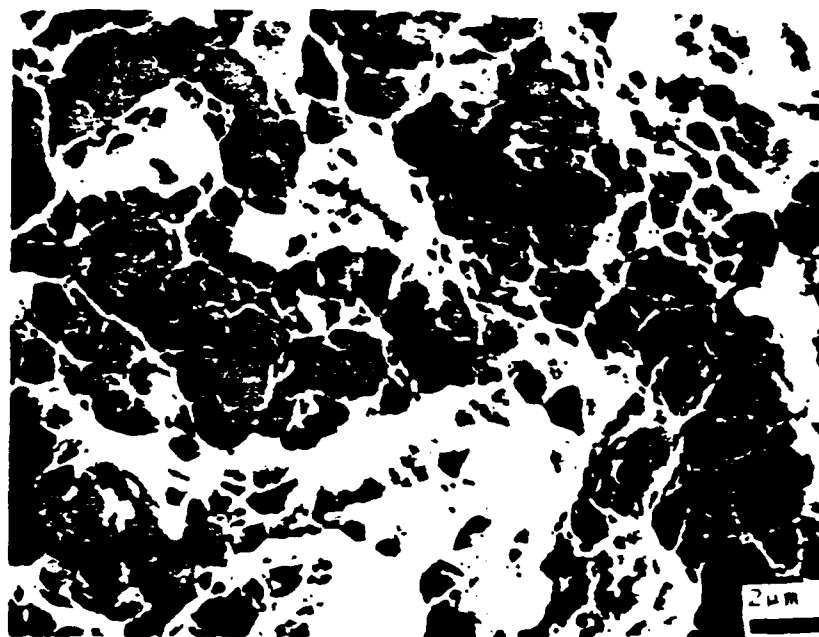
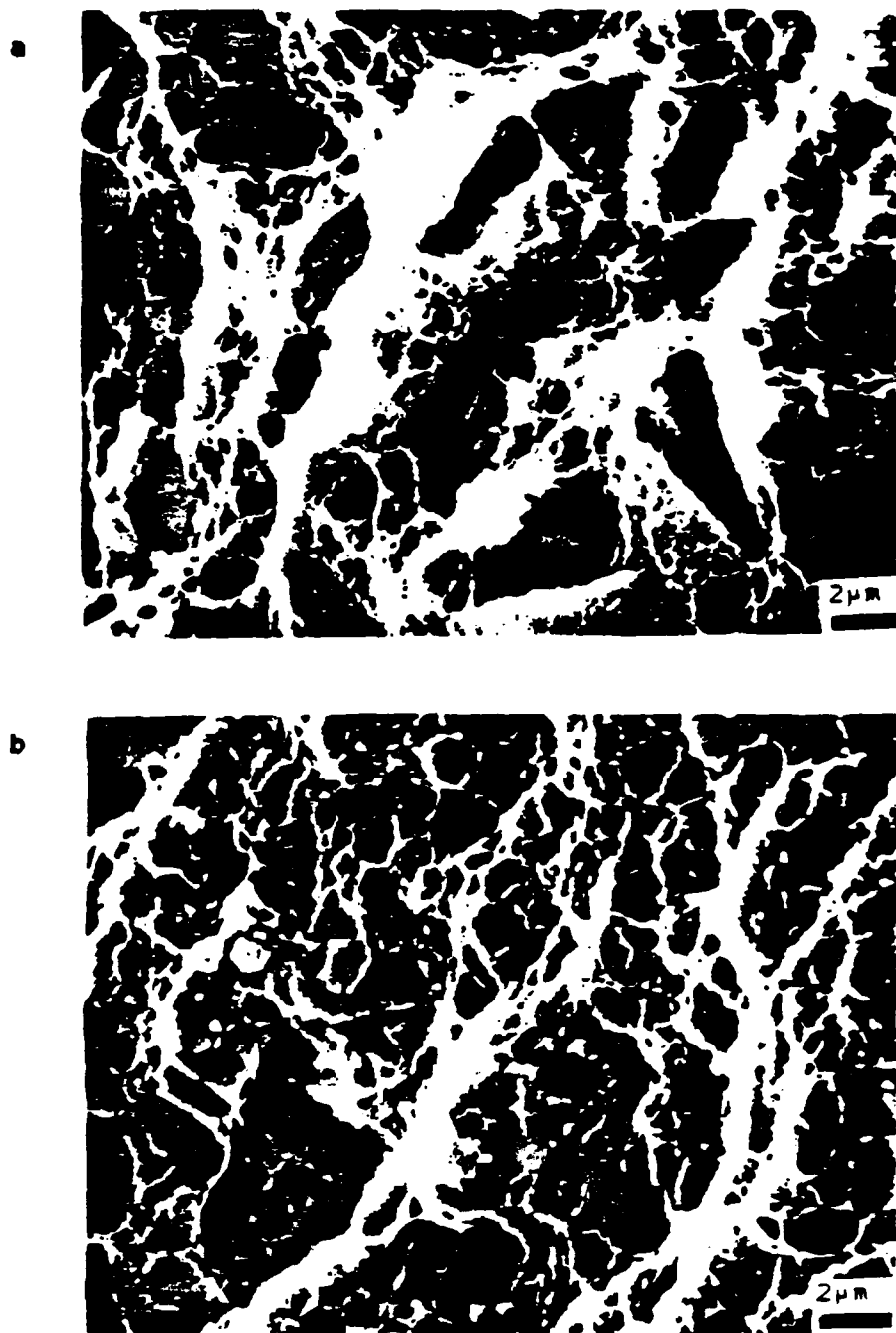


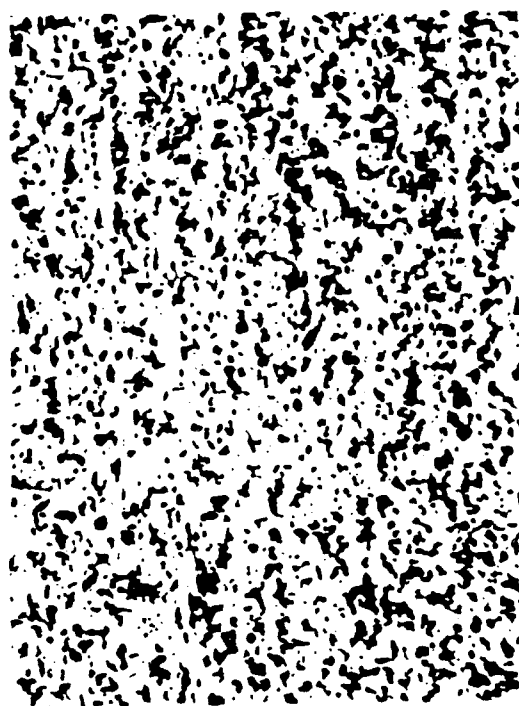
FIGURE 3.45 SCANNING ELECTRON MICROSCOPY
TENSILE FRACTOGRAPHS OF AM4: a) AS-RECEIVED
AND b) TESTED AT 300 °C



**FIGURE 3.46 SCANNING ELECTRON MICROSCOPY
TENSILE FRACTOGRAPHS OF MA4: a) AS-RECEIVED
AND b) TESTED AT 300 C**

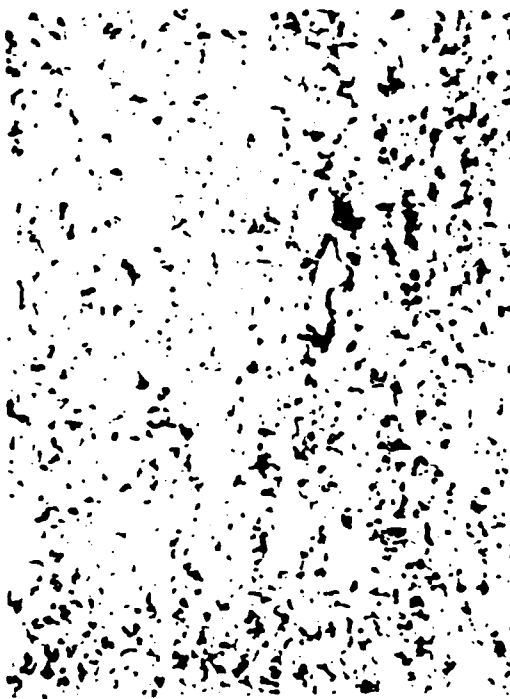


**FIGURE 3.47 OPTICAL MICROGRAPHS
OF TENSILE SPECIMENS TESTED AT 25 C.
a) AT6, b) AM6, and c) MA6**





a



b



c

**FIGURE 3.48 OPTICAL MICROGRAPHS
OF TENSILE SPECIMENS TESTED AT 300 C.
a) AT6, b) AM6, and MA6**

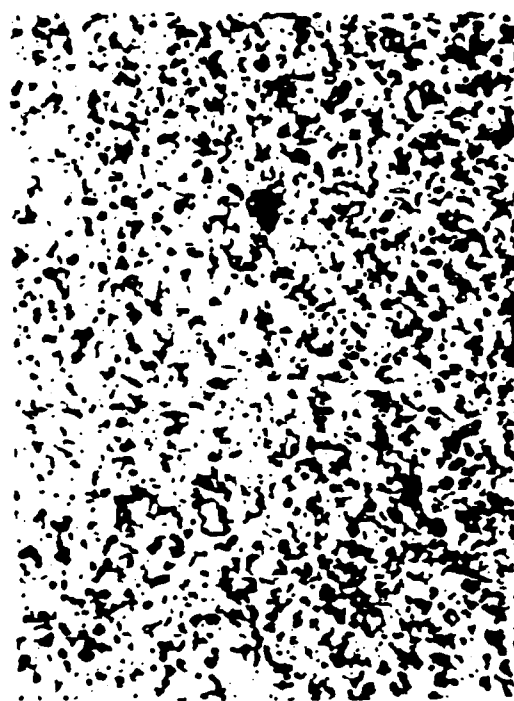


**FIGURE 3.49 OPTICAL MICROGRAPHS
OF CREEP SPECIMENS TESTED AT 250 C.
AND 138 MPa FOR 150 HRS. a) AT4,
b) AM6, and c) MA6**

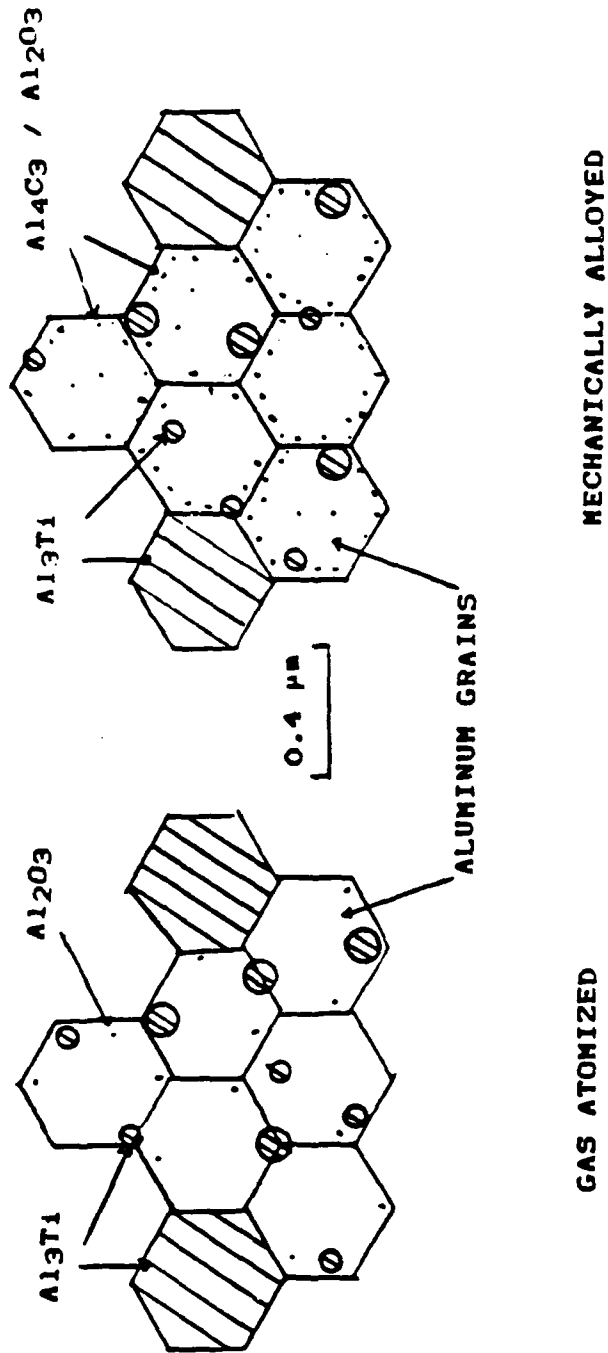


FIGURE 4.1 MICROSTRUCTURAL MODEL ILLUSTRATING THE RELATIVE SIZE AND SPACING OF PARTICLES AND GRAINS

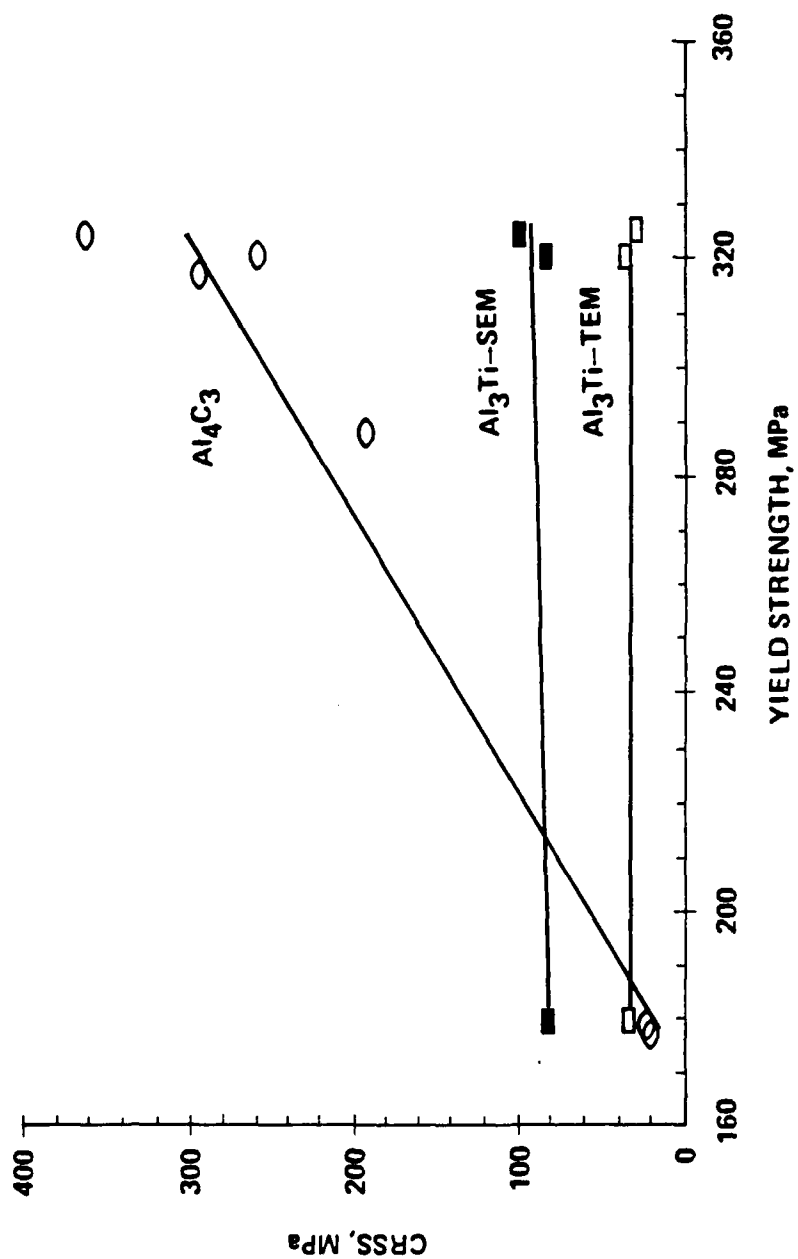


FIGURE 4.2 CALCULATED OROWAN STRENGTHENING OF DISPERSOIDS VERSUS ALLOY STRENGTH

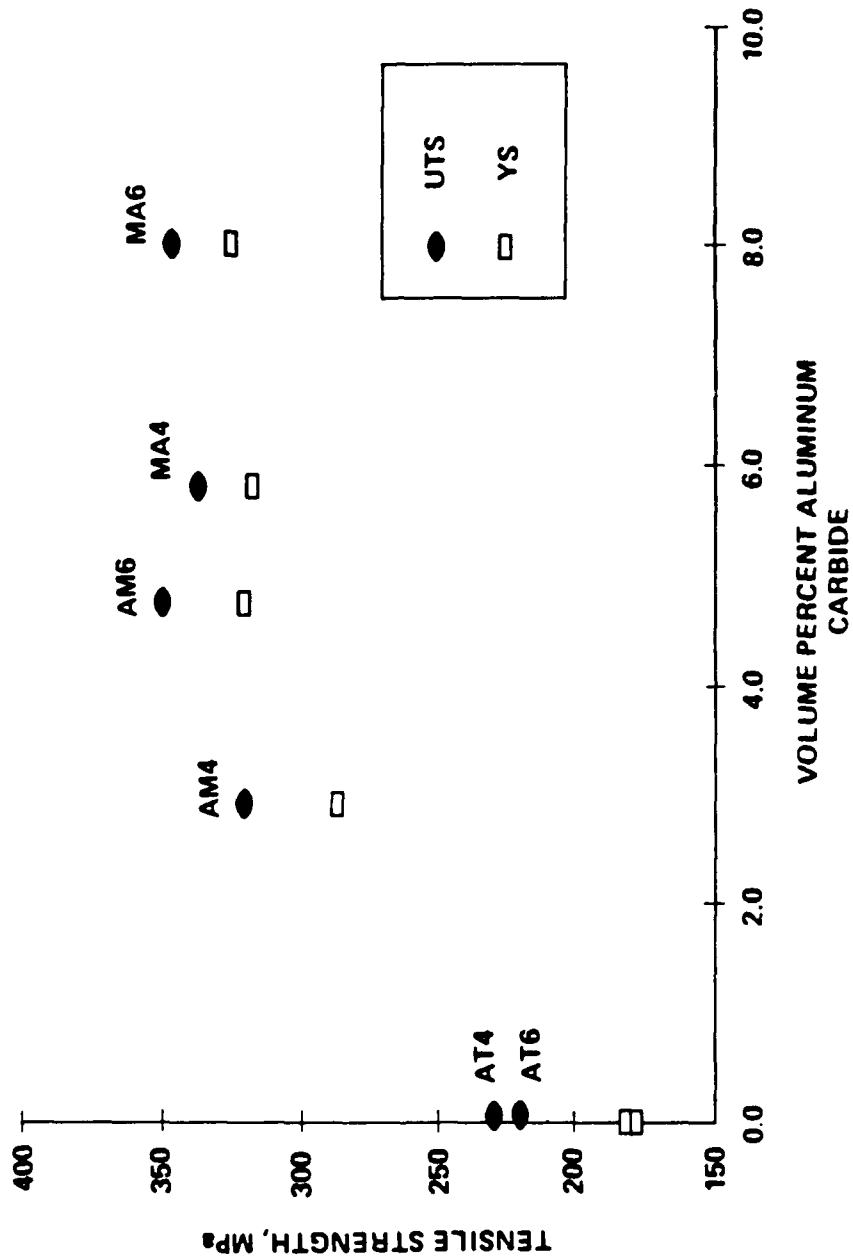


FIGURE 4.3 EFFECT OF ALUMINUM CARBIDES ON TENSILE STRENGTH

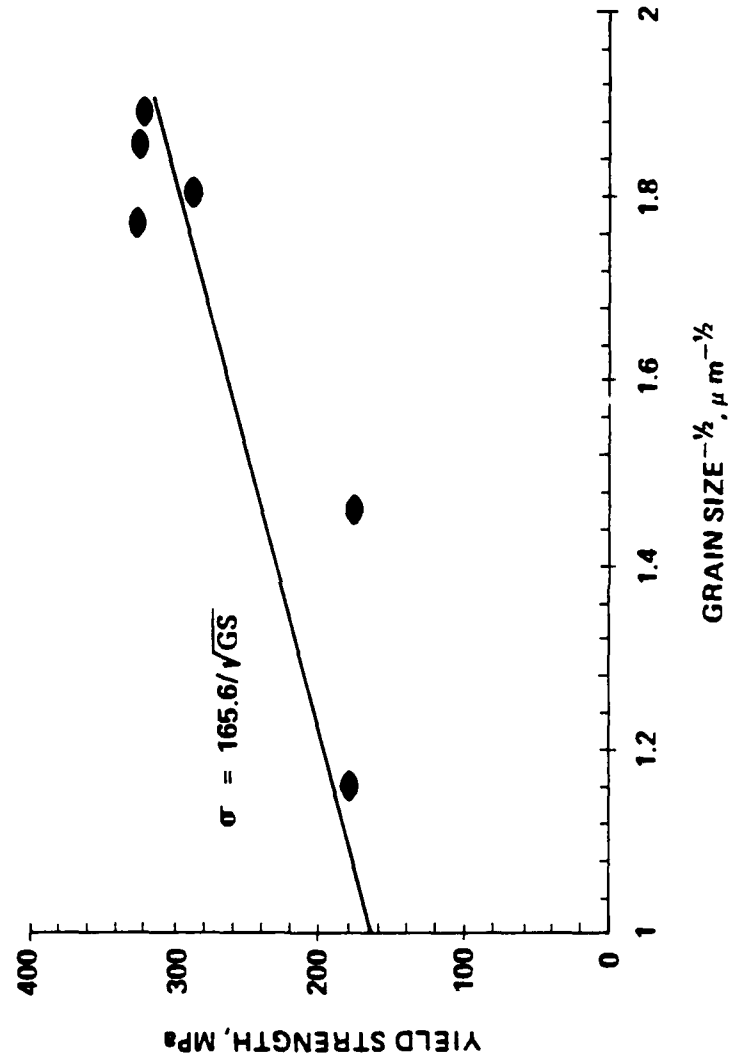


FIGURE 4.4 THE EFFECT OF GRAIN SIZE ON YIELD STRENGTH

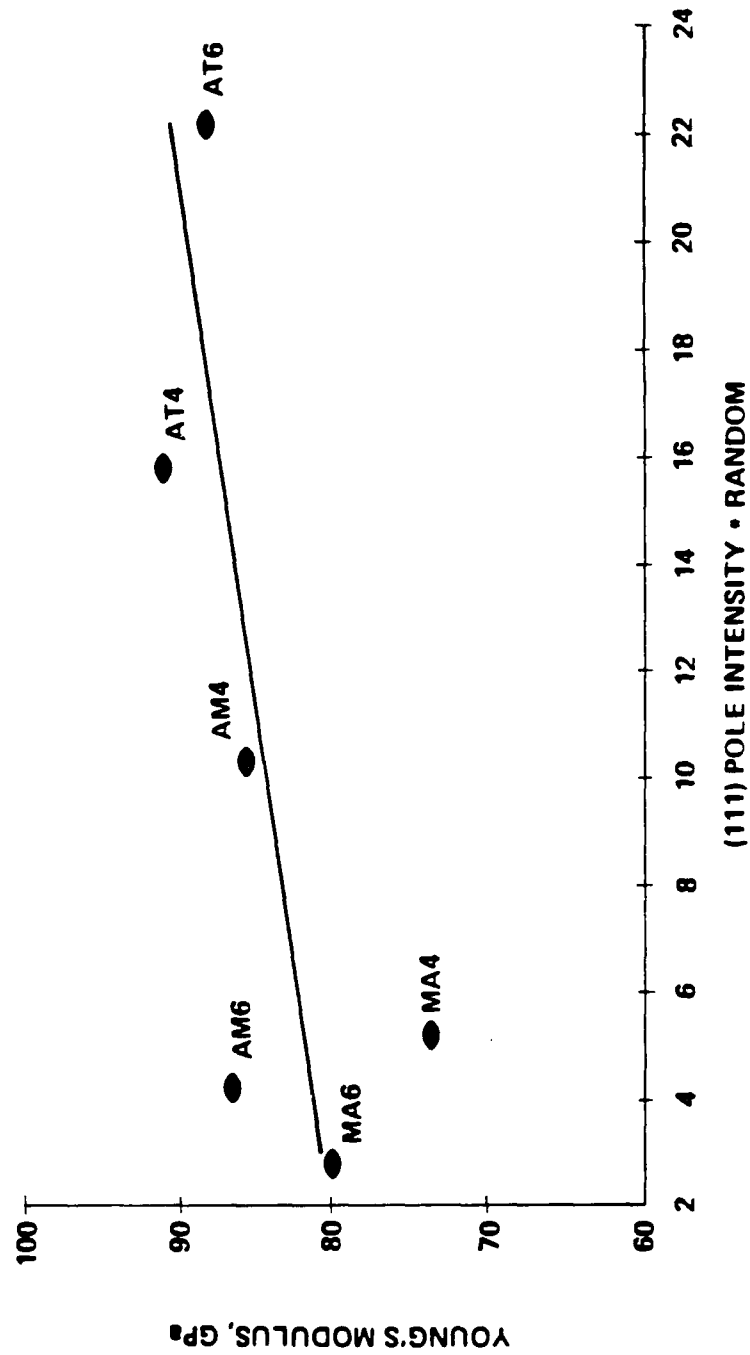


FIGURE 4.5 EFFECT OF TEXTURE ON YOUNG'S MODULUS

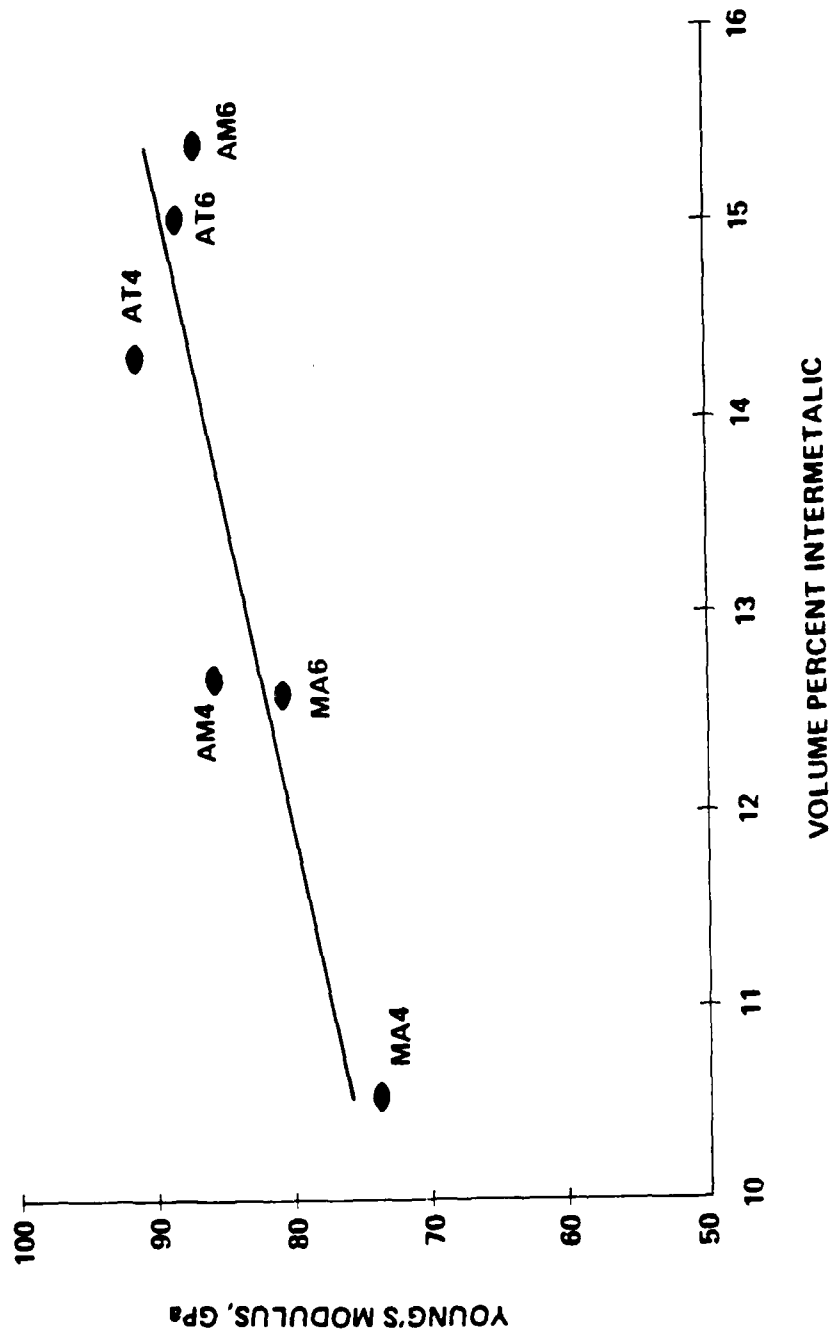


FIGURE 4.6 EFFECT OF Al_3Ti ON YOUNG'S MODULUS

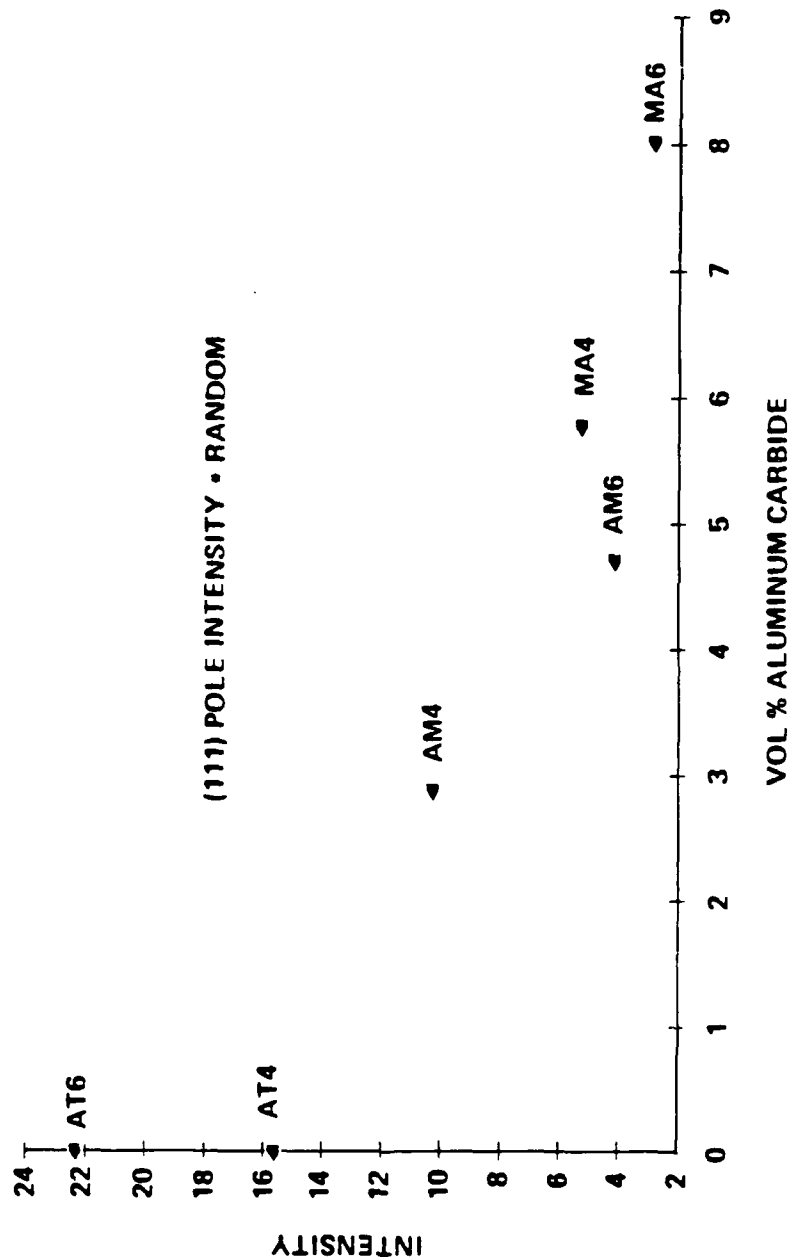


FIGURE 4.7 EFFECT OF DISPERSOIDS ON TEXTURE DEVELOPMENT

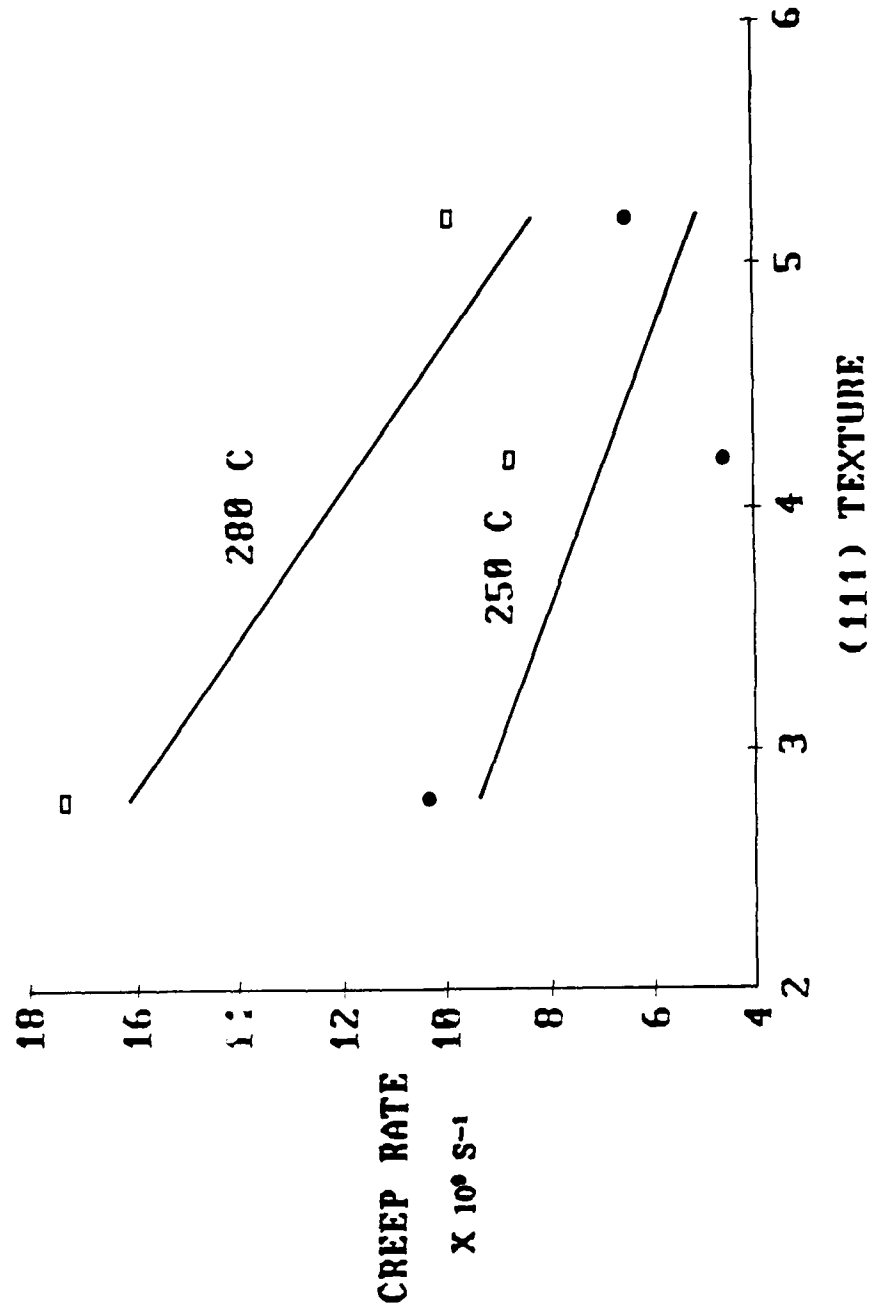


FIGURE 4.8 EFFECT OF TEXTURE ON CREEP RATE

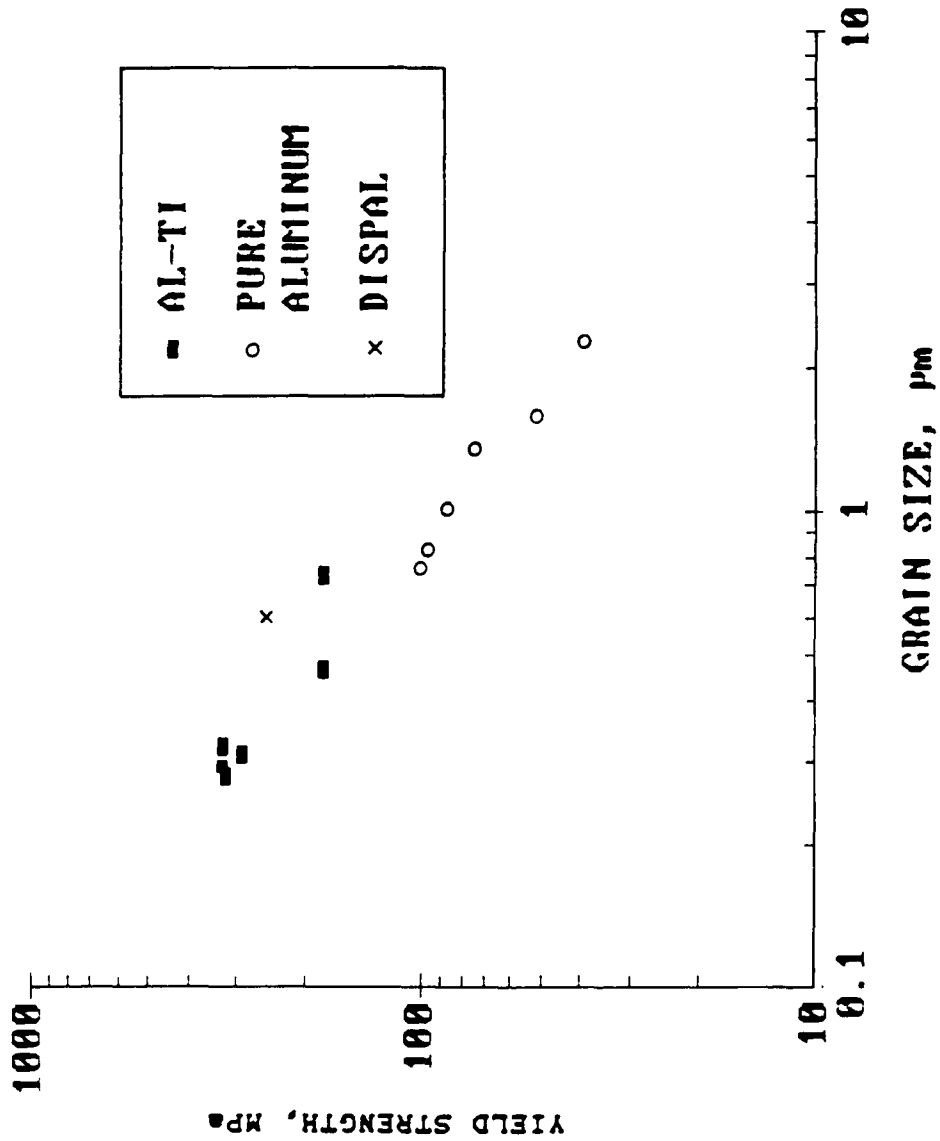


FIGURE 5.1 THE EFFECT OF GRAIN SIZE ON THE STRENGTH OF
PM ALUMINUM-TITANIUM AND PURE ALUMINUM

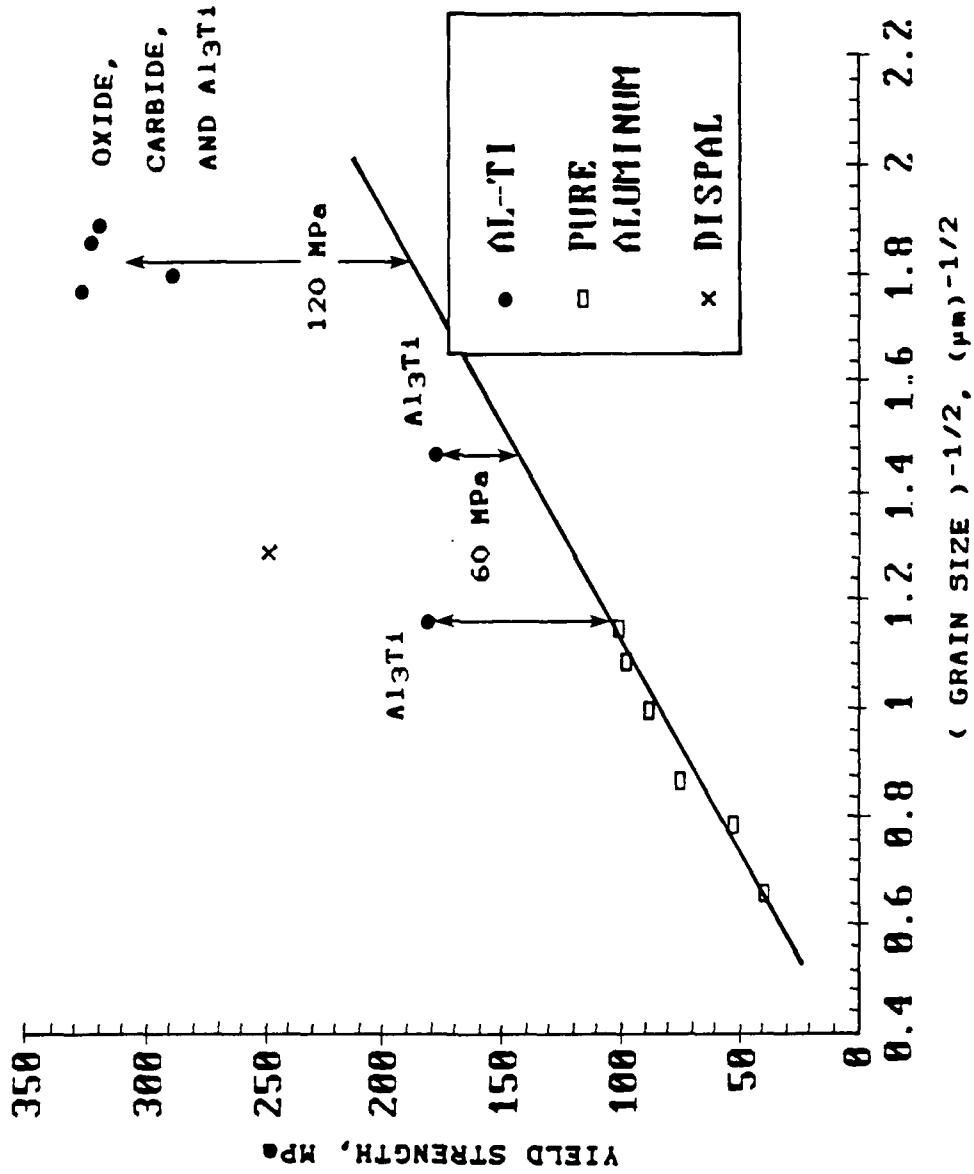


FIGURE 5.2 HALL-PETCH STRENGTHENING OF PM ALUMINUM-TITANIUM AND PURE ALUMINUM

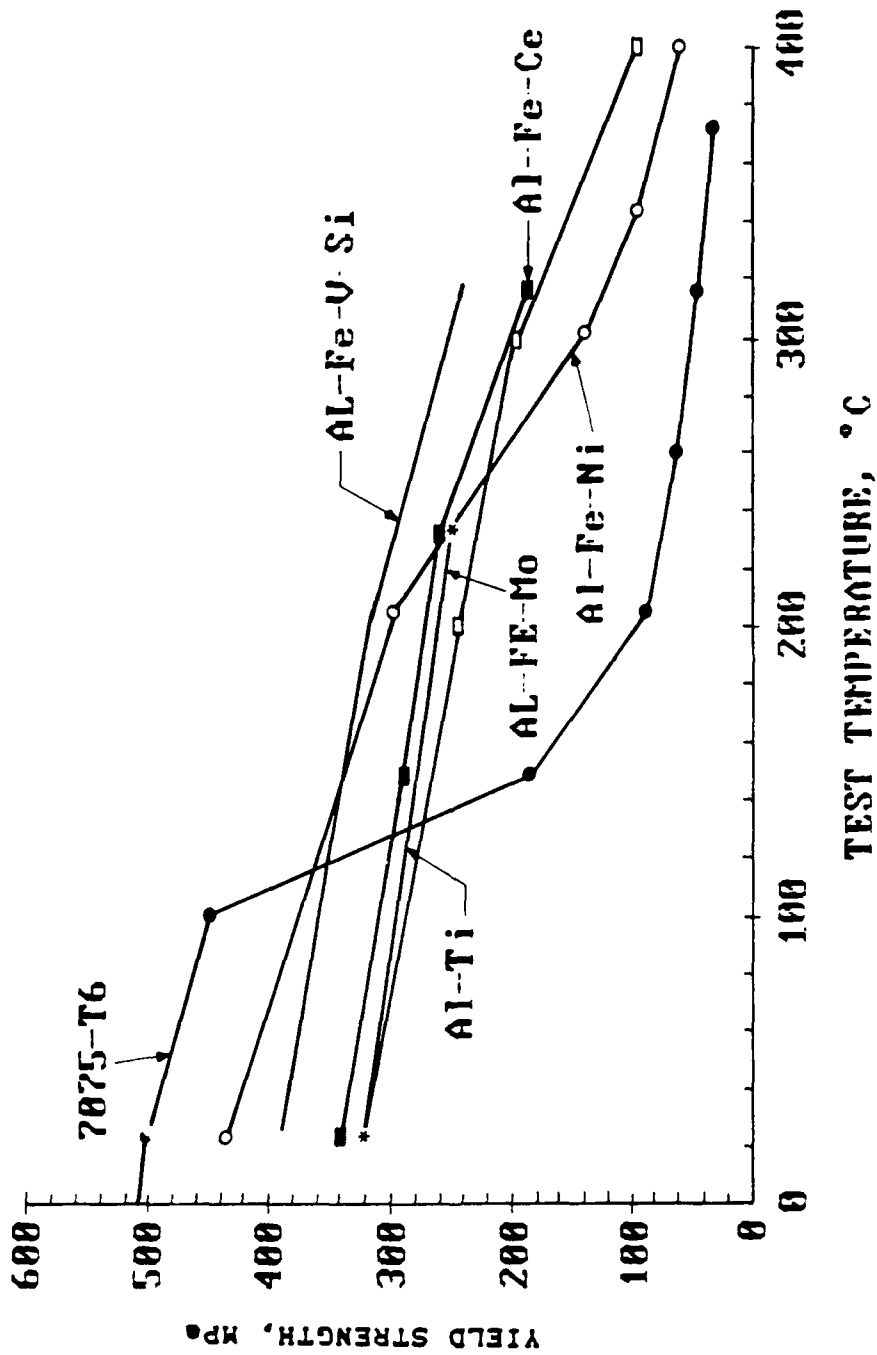


FIGURE 5.3 THE STRENGTH OF SEVERAL ALUMINUM ALLOYS TESTED AT TEMPERATURE

NADC-87159-60

X. REFERENCES

REFERENCES

1. I.F. Sakata and S.L. Langenbeck, "P/M Aluminum Alloy in Place of Titanium," Based on "Elevated Temperature Aluminum Alloys for Aerospace Applications," *Aerospace Engineering*, March/April, 1984.
2. P.P. Millan, Jr., "Application of High-Temperature Powder Metal Aluminum Alloys to Small Gas Turbines," *Journal of Metals*, vol. 35, March, 1983, p.76.
3. C.G. Levi and R. Mehrabian, "Heat Flow During Rapid Solidification of Undercooled Metal Droplets," *Metallurgical Transactions A.*, vol. 13A, 1982, p.221.
4. H. Jones, "Observations on a Structural Transition in Aluminum Alloys Hardened by Rapid Solidification," *Material Science and Engineering*, vol. 5, 1969.
5. J.R. Manning, J.G. Early, W.B. Boettinger, L.A. Bendersky, and F.S. Biancaniello, 1st Quarterly Report, "Consolidation of Rapidly-Solidified High Temperature Aluminum Alloys," National Bureau of Standards, for the Naval Air Development Center, N000198WR41136, June, 1984.
6. J.R. Manning, J.F. Early, W.J. Boettinger, L.A. Bendersky, and F.S. Biancaniello, "Consolidation of Rapidly-Solidified High Temperature Aluminum Alloys," Second Quarterly Report, NBS, Oct. 1984. N62269-84WR-00198.
7. N. Grant, "Rapid Solidification of Metallic Particles," AIME Conf. Proc. *High Strength Powder Metallurgy Aluminum Alloys*. ed. M.J. Koczak and G.J. Hildeman, Feb., 1982. p.3.
8. R. Mehrabian, "Rapid Solidification," *International Metals Reviews*, vol. 27, no. 4, 1982, p.185.
9. J.P. Hirth, *Metallurgical Transactions*, vol. 9A, 1978, p.401.
10. R.E. Sanders, Jr., and G.H. Hildeman, "Elevated Temperature Aluminum Alloy Development," Final Report, AFWAL Contract No. F-3315-77-C-5086, June, 1981.
11. C.M. Adam, R.G. Bourdeau, J.W. Broch, and A.R. Cox, "Application of Rapidly Solidified Alloys," Final Report, AFWAL Contract No. F-33615-76-C-5136, Dec., 1981.
12. W.M. Griffith, R.E. Sanders, Jr., and G.J. Hildeman, "Elevated Temperature Aluminum Alloys for Aerospace Applications," *ibid.* ref. 7, p.209.
13. A.K. Gogia, P.V. Rao, and J.A. Sehhar, *Journal of Material Science*, vol. 20, 3091, 1985.
14. S.C. Jha and T.H. Sanders, Jr., "Microstructure of Melt-Spun Al-Fe and Al-Fe-Ce Alloys," AIME Conf. Proc. *High Strength Powder Metallurgy Aluminum Alloys II*. ed. G.J. Hildeman and M.J. Koczak, Oct., 1985. p.243.
15. S.D. Kirchoff, R.H. Young, W.M. Griffith, and Y.W. Kim, "Microstructure/Strength/Fatigue Crack Growth Relations in High Temperature P/M Aluminum Alloys," *ibid.* ref. 7, p.237.
16. D.J. Skinner, R.L. Rye, D. Raybould, and A.M. Brown, "Dispersion Strengthened Al-Fe-V-Si Alloys," *Scripta Metallurgica*, vol. 20, 1986, p.867.

17. F.H. Froes and J.R. Pickens, "Powder Metallurgy of Light Metal Alloys for Demanding Applications," *Journal of Metals*, Jan., 1984.
18. D.L. Eric, "Development of a Mechanically Alloyed Aluminum Alloy for 450-650°F. Service," AFML, AFML-TR-79-4210, August, 1979.
19. R.D. Schelleng and S.J. Donachie, "Mechanically Alloyed Aluminum," *Metal Powder Report*, vol. 38, No. 10, Oct., 1983.
20. J.P. Lyle, Jr., "Excellent Products of Aluminum Powder Metallurgy," *Journal of Metals*, Jan. 1957, p.109.
21. R.J. Towner, "Atomized Powder Alloys of Aluminum," *Metals Progress*, May 1985, p.70.
22. E.A. Block, "Dispersion Strengthened Aluminum Alloys," *Metallurgical Reviews*, vol. 6, no. 22, 1961, p.193.
23. F.V. Lenel, A.B. Backensto, Jr., and M.V. Rose, "Properties of Aluminum Powder and of Extrusions Produced From Them," *Journal of Metals*, Jan. 1957, p.124.
24. R.F. Singer, W.C. Oliver, and W.D. Nix, "Identification of Dispersoid Phases Created in Aluminum During Mechanical Alloying," *Met. Trans. A.*, vol. 11A, 1980, p.1895.
25. J.S. Benjamin, *Metallurgical Transactions*, vol.1, p.2943, 1970.
26. ASM, *Powder Metallurgy*, vol. 7, 9th edition, ASM 1984, p.56.
27. P.S. Gilman and W.D. Nix, "The Structure and Properties of Aluminum Alloys Produced by Mechanical Alloying: Powder Processing and Resultant Powder Structures," *Met. Trans. A.*, vol. 12A, May, 1981, p.813.
28. J.S. Benjamin and M.J. Bomford, "Dispersion Strengthened Aluminum Made by Mechanical Alloying," *Met. Trans. A.*, vol. 8A, Aug., 1977, p.1301.
29. F.G. Lovshenko and G. Jangg, "Production of Dispersion-Hardened Aluminum Carbon Alloys. Part I," *Soviet Powder Metallurgy and Metal Ceramics*, vol. 17, no.9, Sept., 1978.
30. V. Arnhold and J. Baungarten, "Dispersion Strengthened Aluminum Extrusion," *Powder Metallurgy International*, vol.17, no.4, 1985, p.168.
31. J.S. Benjamin and R.D. Schelleng, "Dispersion Strengthened Aluminum-4 Pct. Magnesium Alloy Made by Mechanical Alloying," *Met. Trans. A.*, vol. 12A, Oct., 1981, p.1827.
32. S.K. Kang, D.L. Erich, and H.F. Merrick, "The Mechanical Behavior of Mechanically Alloyed Al Alloys," *ibid.* ref. 7, p.317.
33. E.A. Starke, Jr., "Aluminum Alloys of the 70's: Scientific Solutions to Engineering Problems. An Invited Review," *Material Science and Engineering*, vol. 29, 1977.
34. R.J. Bucci, "Selecting Aluminum Alloys to Resist Failure by Fracture Mechanisms," *Engineering Fracture Mechanics*, vol. 12, p.407-441, Pergamon Press, 1979.

35. P. Haasen, "Mechanical Properties of Solid Solutions and Intermetallic Compounds-Chapter 21," *Physical Metallurgy*. Editors: R.W. Cahn and P. Haasen. North Holland, New York, 1983.
36. G.E. Dieter, *Mechanical Metallurgy*. McGraw-Hill, New York, 1976, p.210.
37. J.H. Frye and Hune-Rothery, *Proceedings of the Royal Society, London*, vol. 181, p.1-14, 1942.
38. E.A. Starke, Jr., and J.A. Wert, "The Strengthening Mechanisms of Aluminum Powder Alloys," *ibid.* ref. 14, p.3.
39. W.R. Hibbard, *Transactions of the Metallurgical Society, AIME*, vol. 212, p.3, 1958.
40. R.W. Hertzberg, *Deformation and Fracture Mechanics of Engineering Materials*. John Wiley, New York, 1976, p.14.
41. E. Schmid. *Z. Electrochem*, vol. 37, p.447, 1931.
42. G.J. Taylor, *Journal Institute of Metallurgy*, vol. 62, p.307, 1938.
43. J.F.W. Bishop and R. Hill, *Philos. Mag.*, vol. 42, p.414-427, 1298-1307, 1951.
44. I.G. Palmer, R.E. Lewis, and D.D. Crooks, "The Design and Mechanical Properties of Rapidly Solidified Al-Li-Y Alloys," *Conf. Proc. AIME Aluminum Lithium Alloys*. ed., T.H. Sanders, Jr. and E.A. Starke, Jr., May, 1980.
45. E.O. Hall, *Proceedings of the Physics Society of London*, vol. 643, p.747, 1951.
46. N.J. Petch, *London Journal of Iron and Steel Industry*, vol. 173, p.25, 1953.
47. R.F. Decker, "Alloy Design Using Second Phases," *Metallurgical Transactions*, vol. 4, Nov. 1973, p.2495.
48. N. Hansen, "Effect of Grain Size on the Mechanical Properties of Dispersion-Strengthened Aluminum-Oxide Products," *Transactions of the Metallurgical Society of the AIME*, vol. 245. p.1305. June, 1969.
49. J.A. Wert, *Strength of Metal Alloys*. ed. R.C. Gifkins, Pergamon Press, p.339, 1980.
50. Y.W. Kim and W.M. Griffith *PM Aerospace Materials*, vol. 1, MPR, Shrewsburg, UK, 1984.
51. J.C.M. Li and Y.T. Chou, *Metallurgical Transactions*, vol. 1, p.1145-1159, 1970.
52. J.P. Hirth, *Metallurgical Transactions*, vol. 3, p.3047-3067, 1972.
53. J.W. Martin, *Micromechanisms in Particle Hardened Alloys*. Cambridge University Press, Cambridge. 1980.
54. P.B. Hirsh and A. Kelly. *Philosophic Magazine*. vol. 12, p.881, 1965.
55. E. Orowan. in *Symposium on Internal Stress in Metals and Alloys*. London: Institute of Metals. 1948. p.451.

56. D. Hull and D.J. Bacon, *Introduction to Dislocations*, vol. 37, Pergamon Press, Oxford, 1984.
57. R.S.W. Shewfelt, and L.M. Brown, "Philosophic Magazine, vol. 35, p. 945, 1977.
58. G.S. Ansell and J. Weertman, AIME Transactions, vol. 215, p.838, 1959.
59. R.W. Lund and W.D. Nix, Acta Metallurgica, vol. 24, p.469, 1976.
60. R.W. Lund and W.D. Nix, Metallurgical Transactions, vol. 6A, p.1329, 1975.
61. J.M. Lifshitz and V.M. Slyzov, "The Kinetics of Precipitation from Supersaturated Solid Solutions," Journal of Physics and Chemistry of Solids. vol. 19, Nos. 1/2, 1961, p.35.
62. Huttlgren et. al.: Selected Values of the Thermodynamic Properties of Binary Alloys. ASM, Ohio, 1973.
63. D.H. St. John and L.M. Hogan, "Thermal Stability in the Al-Al₃Ti System," Journal of Material Science. vol. 15, 1980, p.2369.
64. L.F. Mondolfo, *Aluminum alloys: Structure and Properties*. Butterworths, London-Boston., 1979.
65. M. Hansen, *Constitution of Binary Alloys*. McGraw-hill, New York, 1958.
66. D.H. St. John, and L.M. Hogan, "Metallography and Growth Crystallography of Al₃Ti in Al-Ti Alloys up to 5 wt.%Ti," Journal of Crystal Growth, vol. 46, 1979, p.387-398.
67. D.H. St. John, and L.M. Hogan, "Segregation Patterns in Unidirectionally Solidified Al-Ti Solid Solution Alloys," Journal of Crystal Growth, vol. 46, 1979, p.585-587.
68. H. El-Halfawy et. al., "Al₃Ti Precipitates in a Chill-Cast Al-14 wt.% Ti Alloy," Metallography, vol. 12, no.9, Sept., 1979.
69. J. Cisse, H.W. Kerr, and G.F. Bolling, "The Nucleation and Solidification of Al-Ti Alloys," Metallurgical Transactions, vol. 5, March, 1974, p. 633.
70. J.H. Westbrook, Ed., *Intermetallic Compounds*. John Wiley and Sons, New York, 1967.
71. S. Tsunekawa and M.E. Fine, "Lattice Parameters of Al₃(Zr_xTi_{1-x}) Vs. x in Al-2AT.% (Ti + Zr) Alloys," Scripta Metallurgica, vol. 16, 1982, p.391.
72. S. Hashimoto, K F Kobayaski, and S. Miura, "Roles of Lattice Coherency to the Heterogeneous Nucleation in the Al-Ti System," Zeitschrift fuer Metallkunde, Dec., 1983.
73. J.W. Martin and R.D. Doherty, *Stability of Microstructure in Metallic Systems*. Cambridge Univ. Press, Cambridge, 1980.
74. H.W. Kerr, J. Cisse, and G.F. Bolling, "On Equilibrium and Non-Equilibrium Peritectic Transformations," Acta Metallurgica, vol. 22, June, 1974, p.677.
75. D.H. St. John and L.M. Hogan, "The Peritectic Transformation," Acta Metallurgica, vol. 25, 1977, p.77.

76. Y.R. Mahajan, S.D. Kirchoff, and F.H. Froes, "Thermal Stability of Rapidly Solidified Al-Ti-Gd Alloy," *Scripta Metallurgica*, vol. 20, 1986.
77. A.G. Jackson, Y.R. Mahajan, and S.D. Kirchoff, "Identification of $Al_{20}Ti_2Gd$ Precipitates in an Aged RST Al-4Ti-4Gd Alloy," *Scripta Metallurgica*, vol. 20, no. 9, Sept., 1986.
78. Y.R. Mahajan, Y.W. Kim, and F.H. Froes, "Microstructural Characterization and Thermal Stability of Rapidly Solidified Al-5Fe-3Ti and Al-5Fe 3Ti-2Er Alloys," *ibid.* ref. 14, p.333.
79. American Society for Testing and Materials, *1981 Annual Book of ASTM Standards*. Part 10, Phila., PA, 1981.
80. Y.W. Kim, W.M. Griffith, and F.H. Froes, "The Breakup and Distribution of Surface Oxides Through Processing of P/M Aluminum Alloy 7091," *Metals/Materials Technology Series*. 1983 ASM metals Congress.
81. M.L. Ovecoglu and W.D. Nix, "Characterization Studies of Mechanical Alloying of Rapidly Solidified Al-8.4%Fe-3.4%Ce Powders," *ibid.* ref. 14, p.225.
82. M.J. Koczak, M.K. Premkumar, and W.E. Frazier, "In-situ Metal Matrix Composites," Presented at the Annual meeting of the American Ceramics Society/National Aeronautic and Space Administrations, Cocoa Beach Fl. Jan. 1986.
83. A. Banerji and W. Reif, "Development of Al-Ti-C Grain Refiner Containing TiC," *Metallurgical Transactions*. vol. 17A. December, 1986.
84. L.S. Darken and R.W. Gurry, *Physical Chemistry of Metals*, McGraw-Hill, New York, 1953.
85. U.V. Deshmukh, "Mechanical Properties and Microstructures of Manganese Modified Al-Zn-Mg-Cu P/M Alumiun Alloys," Ph.D. Thesis, Drexel University, 1987.
86. M.E. O'Dowd, "The Influence of Precipitate Type on the Elastic Properties of Aluminum-Copper-Lithium Alloys," University of Virginia, Master's Thesis, 1987.
87. W. Voight, *Lehrbuch der Kristallphysik*. B.G. Teubner Verlag, Stuttgart, 1966.
88. A. Ruess, "Berechnung der Fließgrenze von Mischkristallen auf Grund der Plastizitätsbedingung für Einkristalle," *Z. Angew. Math. Mech.*, vol.9, 1929, p.49.
89. R. Hill, "The Elastic Behavior of a Crystalline Aggregate," *Proc. Phys. Soc.*, vol. A65, 1952, p.349.
90. M.E. Fine, "Elastic Moduli of Two Phase Aluminum Alloys," *Scripta Metallurgica* vol. 15, 1981, pp. 523-524.
91. J.P. Lyle, Jr., *Aluminum*. ed. by K.R. Horn, ASM Metals Park, Ohio, vol. 1 1967, pp.337-358.
92. J. Holowach and T.K. Redder, "Ti/Al Design/Cost Trade-off Analysis," General Electric Co. for the Air Force Aero Propulsion Laboratory, Report No. AFAPL-TR-78-74, Feb. 1979.
93. C.S. Barrett, *Structure of Metals*. McGraw-Hill, New York, 1952.

94. E. Arzt, M.F. Ashby, and R.A. Verrall, "Interface Controlled Diffusional Creep," Acta Met. vol. 31, No. 12, pp.1977-1989, 1983.
95. J. Weertman and J.R. Weertman, "Mechanical Properties II," *ibid* ref. 35, p.1310.
96. M. Sahoo and J.A. Lund, "Substructure and Dispersion Hardening in Aged, Cold Worked and Annealed Al-4Wt Pct Cu Alloy," Met. Trans. vol. 4, p.39, January 1973.
97. Alcoa, Preliminary Data-Wrought P/M Alloy CU78 Extrusions and Forgings, Alcoa, 1984.
98. Allied Signal, "Aluminum Alloy FVS1212 for High Temperature/High Stiffness Applications." Product Literature, Allied Signal, 1984.
99. Allied Signal, "Aluminum Alloy FVS0812 for High Temperature/High Stiffness Applications." Product Literature, Allied Signal, 1984.

ACKNOWLEDGEMENT

The author wishes to acknowledge the financial support of the Navy's RST program manager, Dr. Gilbert London; and the managerial and technical support of Drs. John J. DeLuccia and Jeffrey Waldman. The author owes a special debt of gratitude to Prof. Michael J. Koczak, Drexel University, Phila., PA. Without Prof. Koczak's technical guidance and support, this report and Ph.D. thesis would have been impossible.